Title
Investigating the Metabolic Landscape of T Cell Development from Hematopoietic Stem Cells In Vivo and In Vitro

Author
Sun, Victoria

Publication Date
2021

UNIVERSITY OF CALIFORNIA

Los Angeles

Investigating the Metabolic Landscape of T Cell Development from Hematopoietic Stem Cells *In Vivo* and *In Vitro*

A dissertation submitted in partial satisfaction of the requirements for the degree Doctor of Philosophy in Molecular Biology

by

Victoria Sun

2021

ABSTRACT OF THE DISSERTATION

Investigating the Metabolic Landscape of T Cell Development

from Hematopoietic Stem Cells *In Vivo* and *In Vitro*

by

Victoria Sun

Doctor of Philosophy in Molecular Biology

University of California, Los Angeles, 2021

Professor Gay M. Crooks, Chair

Normal T cell production from hematopoietic stem and progenitor cells (HSPCs) declines with age, causing the immune system to become less efficient at fighting illnesses ranging from infections to cancer. T cell development begins when HSPCs from the bone marrow circulate in the blood and home to an organ called the thymus. After populating the thymus, HSPCs are first directed to a T cell fate. In later stages, committed thymocytes advance through pivotal checkpoints to mature into different types of T cells with specialized functions that then egress from the thymus. Although the metabolism of peripheral and activated T cells has been extensively studied, metabolic changes during stem cell development into T cells are not well understood, especially in human thymus.

In vitro models of T cell differentiation are promising tools to study T cell development, but how well they reflect *in vivo* metabolism remains unclear. Studying metabolic changes *in vitro* also faces several challenges due to limitations in current standard culture systems. Previously, our lab developed an *in vitro* 3D "Artificial Thymic Organoid" (ATO) model that generates functional human T cells from various stem cell sources. Our goal is to improve T cell production and ultimately advance T cell therapies that regenerate the immune system. Here, we adapt the ATO system to recapitulate thymic differentiation of murine HSPCs into mature T cells and overcome several limitations of previous *in vitro* systems.

Next, we integrate transcriptomics and metabolic extracellular flux data from human and murine *in vivo* and *in vitro* thymocytes to define the metabolic signatures that distinguish T lineage commitment and T cell maturation stages in the thymus. We reveal that patterns of metabolic activity are remarkably well-conserved in human and murine species, and during *in vitro* T cell development. Glycolysis and oxidative phosphorylation are drastically reduced at the developmental stage during which thymocytes are completing T cell receptor (TCR) rearrangement. Using an *in vitro* mouse knockout model of the recombinase activating gene *Rag-1*, we demonstrate that metabolic activity persistently decreases at the same stage even in the absence of TCR rearrangement. Thus, our results identify critical metabolic transitions that are highly conserved between species as well as *in vivo* and *in vitro* T cell development. Future studies in the lab would study the impact of perturbing metabolic pathways on T cell development, particularly in the context of aging.

The dissertation of Victoria Sun is approved.

Hilary Ann Coller

Kenneth A. Dorshkind

Leanne Dana Jones

Caius Gabriel Radu

Gay M. Crooks, Committee Chair

University of California, Los Angeles

2021

Dedication

To my friends, lab family, mentors, and collaborators.

To my family Liqing Lee Sun, Jiao Wang, Angela Sun, Christopher Sun, Tiffany Sun, and Winter Sun.

To my significant other Norman Khoo.

Table of contents

List of Figures

Acknowledgements

I would like to thank my advisor, Dr. Gay M. Crooks, for her constant encouragement and guidance, as well as my lab mentor, Dr. Amelie Montel-Hagen, for teaching me everything possible—from making organoids to writing a paper. I thank my collaborator Dr. Mark Sharpley, whose expertise and ideas paved the way for my project. I thank my thesis committee and additional collaborators from the Banerjee lab for their thoughtful advice. I am incredibly lucky to have joined the Crooks lab family, who assisted me throughout and shared delicious food with me. My research would not have been possible without Dr. Linsey Stiles and the BSCRC Flow Core. I am grateful for my significant other, my best friends, and my family who supported me and my aspirations. I would like to acknowledge my previous mentors who inspired me to pursue a physician-scientist training: Dr. Sally Horne-Badovinac, Dr. Lindsay Lewellyn, Dr. Maria I. Morasso, and Dr. Olivier Duverger.

Chapter 2 is adapted from Montel-Hagen A, Sun V, Casero D, Tsai S, Zampieri A, Jackson N, Li S, Lopez S, Zhu Y, Chick B, He C, de Barros SC, Seet CS, Crooks GM* (2020). "*In vitro* recapitulation of murine thymopoiesis from single hematopoietic stem cells." *Cell Reports*. Volume 33, Issue 4, 2020, 108320. DOI: https://doi.org/10.1016/j.celrep.2020.108320. We gratefully acknowledge the expert technical assistance of Felicia Codrea, Jessica Scholes and Jeffrey Calimlim from the UCLA Broad Stem Cell Research Center (BSCRC) Flow Cytometry Core; as well as the Technology Center for Genomics and Bioinformatics (TCGB) at UCLA and the Translational Pathology Core Laboratory (TPCL) at UCLA. We thank L. Coulombel for generously providing us with MS-5 cells many years ago. This work was supported by the National Institute of Health (NIH Bethesda, MD) grants RO1AG049753 (GMC), R21AI119927 (GMC), 5P30AG028748/UL1TR000124 (NCATS/UCLA CTSI) (D.C), P30CA016042 (NCI)

(TCGB and TPCL cores), KL2TR001882 (NIH/NCATS/UCLA CTSI) (CSS), K08CA235525 (NIH/NCI) (CSS), NIH T32GM008042 (V.S) and the Connie Frank and Evan Thompson Program for Collaborative Restorative Transplantation Research. VS acknowledges the support of the Eli and Edythe Broad Center of Regenerative Medicine and Stem Cell Research at UCLA Training Program.

Author contributions were: Conceptualization, A.M.-H., V.S., C.S.S., and G.M.C.; Methodology, A.M.-H., and V.S.; Formal analysis, D.C.; Investigation, A.M.-H., V.S., S.T., A. Z., N.J., S. L., S.L., Y. Z., B.C. C. H.; Data Curation, D.C.; Writing – Original Draft, A.M.-H., V.S., and G.M.C.; Writing – Review and Editing, A.M.-H., V.S., C.S.S., S.C.D., and G.M.C.; Supervision, G.M.C.; Funding acquisition, G.M.C.

Chapter 3 is adapted from a manuscript in revision (2021). We gratefully acknowledge the expert technical assistance of Jeffrey Calimlim, Felicia Codrea, and Jessica Scholes from the UCLA Broad Stem Cell Research Center (BSCRC) Flow Cytometry Core; the expert technical assistance of Dr. Linsey Stiles from the UCLA Mitochondrial and Metabolism Core; the Technology Center for Genomics and Bioinformatics (TCGB) at UCLA and the Translational Pathology Core Laboratory (TPCL) at UCLA; as well as the Next Generation Sequencing Core at the Salk Institute for Biological Studies. We thank Dr. Christopher S. Seet from UCLA for reviewing the manuscript. We thank Dr. Felix J. Hartmann and Dr. Sean C. Bendall from Stanford University and Katherine Sheu from the Hoffmann Lab at UCLA for assistance with developing R code for analysis, and Dr. Kai Yang and Dr. Hongbo Chi for sharing their thymocyte Seahorse assay protocol. This work was supported by the National Institute of Health (NIH Bethesda, MD) grants RO1AG049753 (to GMC), 5P30AG028748/UL1TR000124 (NCATS/UCLA CTSI) (to DC), P30CA016042 (NCI) (TCGB and TPCL cores), NIH T32GM008042 (to VS), a BSCRC

Innovation Award (to GMC, UB, MS), and the Connie Frank and Evan Thompson Program for Collaborative Restorative Transplantation Research (to GMC). This research was made possible by a grant to GMC from the California Institute of Regenerative (GC1R-06673-B [CRP]). The contents of this publication are solely the responsibility of the authors and do not necessarily represent the official views of CIRM or any other agency of the state of California. K.E.K-U acknowledges the support of the JCCC and Institute for Quantitative & Computational Biosciences at UCLA. VS acknowledges the support of the Eli and Edythe Broad Center of Regenerative Medicine and Stem Cell Research at UCLA Training Program.

Author contributions were: Conceptualization, V.S., M.S., G.M.C, U.B.; Methodology, V.S. and M.S.; Formal analysis, V.S. and M.S.; Investigation, V.S., M.S., A.M.-H., P.C., A.Z., S.L., S.C.D., Y.Z.; Data Curation, V.S., K.E.K-U., D.C.; Human Thymus Sample Contribution, C.P.; Writing – Original Draft, V.S., and G.M.C.; Writing – Review and Editing, V.S., M.S., D.C., S.C.D., and G.M.C.; Supervision, G.M.C.; Funding acquisition, G.M.C., U.B.

BIOGRAPHICAL SKETCH

EDUCATION

UNIVERSITY OF CALIFORNIA, LOS ANGELES (UCLA) Los Angeles, CA
MD, Ph.D. Candidate August 2015 – Current
GPA: 4.00

UNIVERSITY OF CHICAGO Chicago, IL
Bachelor of Arts in Biological Sciences September 2010 – June 2014
GPA: 3.92

RESEARCH EXPERIENCE

UNIVERSITY OF CALIFORNIA, LOS ANGELES (UCLA) Los Angeles, CA
Graduate Student (Dr. Gay Crooks) July 2017 – Ongoing

- Studying how lymphocyte T-cell development in Artificial Thymic Organoids (ATOs) is similar to that in mouse and human thymus.

NATIONAL INSTITUTE OF ARTHRITIS AND MUSCULOSKELETAL AND SKIN DISEASES (NIH) Bethesda, MD
Post-baccalaureate IRTA Trainee (Dr. Maria Morasso) July 2014 – June 2015

- Studied the function of transcription factor Dlx3 as a regulator of tooth development in a mouse model

UNIVERSITY OF CHICAGO (MOLECULAR GENETICS AND CELL BIOLOGY) Chicago, IL
Undergraduate Fellow (Dr. Sally Horne-Badovinac) February 2011 – March 2014

- Investigated the role of oriented follicle cell divisions in *Drosophila* egg chamber elongation

KAISER PERMANENTE (SLEEP DISORDERS CENTER) Fontana, CA
Volunteer Research Coordinator (Dr. Dennis Hwang) September 2013

- Analyzed impact of educative videos and follow-up calls on patient compliance to obstructive sleep apnea treatment

LEADERSHIP, TEACHING, AND VOLUNTEER ACTIVITIES

1/11—8/11: Tutor, **Neighborhoods Schools Program**, Chicago, IL

- Ray Elementary School
- St. Martin's Women Shelter

4/12: Volunteer, **Global Medical Brigades**, Accra, Ghana
9/13—12/13: Hospitalist Research Volunteer, **University of Chicago Medicine Hospitalist Project**, Chicago, IL
9/13—12/13: Health Advocate, **Health Leads at Chicago Family Health Center**, Chicago, IL
9/13—3/14: Undergraduate Teaching Assistant, **University of Chicago**, Chicago, IL

- Fundamentals of Cell and Molecular Biology
- Fundamentals of Genetics

1/16—3/17: Co-Coordinator, **Student Interest Group for Pathology**, David Geffen School of Medicine, Los Angeles, CA
3/18—6/19: Environmental Coordinator, **Weyburn Hilgard Residents' Association**, Los Angeles, CA
3/18—ongoing: Staff Writer, **Signal to Noise Magazine**, Los Angeles, CA
10/19—ongoing: Mentor; **UCLA Program for Excellence in Education and Research in the Sciences (PEERS)**, Los Angeles, CA

HONORS AND AWARDS

2019-2021 Broad Stem Cell Research Center (BSCRC) Training Program Predoctoral Fellowship

2017 Leon D. & Leah E. Rivenburg MSTP Fellowship, UCLA
2013 Katen Scholars Program, University of Chicago
2013 Phi Beta Kappa Honor Society
2012 Biological Sciences Collegiate Division Symposium Presentation Prize Winner, University of Chicago
2012, 2011 Biological Sciences Collegiate Division Summer Fellowship, University of Chicago
2012 Lillian Gertrude Selz Prize, University of Chicago

POSTERS AND PRESENTATIONS

- **Sun V**[*], Montel-Hagen A[*], Casero D, Tsai S, Zampieri A, Jackson N, Li S, Lopez S, Zhu Y, Chick B, He C, de Barros SC, Seet CS, Crooks GM. In vitro recapitulation of murine T cell development from single hematopoietic stem cells. Featured oral and poster presentation at: International Society of Experimental Hematology Scientific Meeting; 2020 Aug 19-21; Virtual
- **Sun V***, Montel-Hagen A*, Tsai S, Jackson N, Zampieri A, Lopez S, Zhu Y, Seet CS, Crooks GM, Artificial Thymic Organoids Recapitulate Murine T Cell Differentiation from Hematopoietic Stem and Progenitor cells. Poster presentation at: UCLA BSCRC Annual Stem Cell Symposium; 2020 Feb 7; Los Angeles, CA
- **Sun V***, Montel-Hagen A*, Tsai S, Jackson N, Zampieri A, Lopez S, Zhu Y, Seet CS, Crooks GM, Artificial Thymic Organoids Recapitulate Murine T Cell Differentiation from Hematopoietic Stem and Progenitor cells. Poster presentation at: La Jolla Immunology Conference**;** 2019 Oct 15-17; San Diego, CA
- **Sun V**, Montel-Hagen A, Seet CS, Crooks GM. Notch signaling in Artificial Thymic Organoids recapitulates murine T cell development *in vitro*. Poster presentation at: Gordon Conference "Stem Cells and Cancer: Developmental, Metabolic and (Epi)Genomic Mechanisms Driving Organogenesis and Tumorigenesis"; 2019 March 24-29; Ventura, CA
- **Sun V**, Montel-Hagen A, Seet CS, Crooks GM. Notch signaling in Artificial Thymic Organoids recapitulates murine T cell development *in vitro*. Poster presentation at: International Society for Experimental Hematology Annual Meeting; 2018 Aug 23-26; Los Angeles, CA

PAPERS

1. Montel-Hagen A, Seet CS, Li S, Chick B, Zhu Y, Chang P, Tsai S, **Sun V**, Lopez S, Chen HC, He C, Chin CJ, Casero D, Crooks GM. Organoid-Induced Differentiation of Conventional T Cells from Human Pluripotent Stem Cells. *Cell Stem Cell.* **24**, 376-389.e8 (2019). doi:10.1016/j.stem.2018.12.011. PubMed PMID: 30661959.
2. Montel-Hagen A[*], **Sun V**[*], Casero D, Tsai S, Zampieri A, Jackson N, Li S, Lopez S, Zhu Y, Chick B, He C, de Barros SC, Seet CS, Crooks GM. In vitro recapitulation of murine thymopoiesis from single hematopoietic stem cells. *Cell Reports*. 27;33(4):108320 (2020). doi: 10.1016/j.celrep.2020.108320. Pubmed PMID: 33113379
3. **Sun V**, Sharpley M, Kaczor-Urbanowicz KE, Chang P, Montel-Hagen A, Lopez S, Zampieri A, Zhu Y, de Barros SC, Parkeh C, Casero D, Banerjee U, Crooks GM. The metabolic landscape of thymic T cell development *in vivo* and *in vitro*. *Frontiers in Immunology*. (in revision)

Chapter 1 – Introduction

Journey through thymic T cell differentiation

A critical requirement for robust, sustained immunological health is the ongoing generation of T cells from hematopoietic stem and progenitor cells (HSPCs) in the thymus. Postnatally, HSPCs originate from the bone marrow, circulate in the blood, and home to the thymus organ located above the heart.

The HSPCs that seed the thymus are a heterogenous pool of multipotent progenitors (1). Hematopoietic stem cells (HSC) and multipotent progenitors (MPP) possess the capacity to generate the various blood cell types in the body, but HSCs have the unique ability to self-renew and maintain the stem cell pool. Downstream progenitors are categorized by their increasingly limited potential for a specific immune cell lineage, mainly myeloid versus lymphoid lineages. For instance, lymphoid-primed MPPs (LMPP), which are a subset of MPPs, and common lymphoid progenitors (CLP) are more primed to differentiate into lymphoid cells, whereas common myeloid progenitors (CMP) are more primed to differentiate into myeloid cells (2).

When HSPCs enter the thymus, Notch signals present in the thymic microenvironment drive multipotent progenitors to progressively commit exclusively to a T cell fate (3, 4). Thymic epithelial cells (TEC) express Notch ligands including Jagged1, Jagged2, Delta-like-1 (DLL1), and Delta-like-4 (DLL4) (5). Moreover, TEC expression of Notch ligands, particularly DLL4, has been shown to be indispensable for T cell commitment (6).

The earliest thymocyte stages are phenotypically double negative (DN) for CD4 and CD8 markers. Committed thymocytes become double positive for CD4 and CD8 and proceed through pivotal developmental checkpoints to generate mature single positive CD8 (SP8) and CD4 (SP4) T cells (**Figure 1-1**). Current understanding of thymopoiesis is chiefly derived from mouse thymus

studies and has been shown to be similar in human thymus, though key differences will be discussed below.

The thymus architecture contains complex spatiotemporal interactions between precursor T cells, thymic epithelial cells (TEC), thymic mesenchyme, and additional hematopoietic cells such as dendritic cells (7-9). The outer region of the thymus is the cortex, and the inner region is the medulla. HSPCs arrive through blood vessels in the cortico-medullary junction. DN thymocytes traverse deeper into the cortex where the majority of developmental events occur.

In the mouse, DN stages can be subdivided by phenotypic markers into DN1, DN2, DN3, and DN4 populations (10). Within the DN1 compartment are the earliest thymic progenitors (ETP), which still retain multi-lineage potential including myeloid lineage (11). The Rothenberg group has further delineated DN2a and DN2b populations; during the DN2a to DN2b transition, transcriptional changes induce DN2b cells to lose alternative lineage potential and commit to the T cell lineage (12).

T cells are defined by the expression of a T cell receptor (TCR) with specific antigen recognition. As precursors commit to the T cell lineage, they initiate exclusive features of T cell development, specifically TCR gene rearrangements. TCR repertoire diversity is generated through somatic recombination of the variable (V), diversity (D), and joining (J) gene segments in TCR genes, which is called V(D)J recombination (13). V(D)J recombination occurs only in B and T cells for the development of antibodies and TCRs respectively. V(D)J recombination is directed by RAG (recombination activating gene) recombinases, RAG1 and RAG2, which are expressed at the DN2-3 and then DP stages (13, 14).

TCR gene rearrangements commence at the DN3 stage (13). Conventional T cells are defined by expression of a TCR alpha and beta chain. There is a subset of unconventional T cells

that express a TCR gamma and delta chain. DN2-3 cells that successfully rearrange both the TCR gamma and delta subunits instead become TCRγδ T cells (8, 13). Early DN cells are alternatively able to differentiate into other unconventional T cell lineages such as natural killer T cells (NKT) and innate lymphoid cells (ILCs) (15, 16). Our focus from now will be on the development of conventional TCRαβ cells.

DN3 cells transition from the DN3a stage to the DN3b stage after successful rearrangement of the TCR beta-chain, a process termed beta-selection (17). The TCR beta locus is rearranged first, and the TCR alpha locus undergoes rearrangement later in development during the DP stage. In the meantime, a pre-Ta surrogate chain binds the completed TCR beta-chain and forms a pre-TCR complex that promotes thymocyte survival and proliferation (18). DN3b cells then progress into the DN4 stage. Subsequent CD8 expression leads to the immature single positive CD8 (ISP8) stage, a molecularly distinct population (19).

In human thymus, early DN progenitors are defined by a different set of cell surface markers than that of mice and have been termed: Thy1, Thy2, and Thy3 (20) (**Figure 1-1**). The Thy1-3 stages express CD34, and the immature single positive stage is marked by acquisition of CD4 (ISP4) in human thymocytes (21, 22). Thy1 is the earliest thymic progenitor (ETP) in human thymocytes, Thy2 cells lose alternative lineage potential, and Thy3 cells are committed to the T lineage (Taghon 2009 Blood). Beta-selection is completed at the ISP4 stage in human, unlike at the DN3b stage in mouse (8, 22-24). Notch signaling has been shown to be required for the proliferation but not differentiation of thymocytes with a TCR-beta chain (24).

ISP cells rapidly differentiate into DP cells, which can be separated into “early” and “late” stages based on surface CD3 and TCRαβ expression; DP early cells do not express CD3 and TCRαβ on the surface, while DP late cells are $CD3^{+}TCR\alpha\beta^{+}$. CD3 is a co-receptor that is required

for TCR complex assembly and intracellular signaling (25). In DP early cells, RAG genes are re-expressed to facilitate TCRα chain rearrangement (14). A majority of DP early cells will fail to generate a productive TCR complex and will die by neglect (17).

Two subsequent TCR-dependent checkpoints in thymic T cell development are critical to ensure proper function of exported T cells: positive and negative selection (17). Thymic selection is primarily mediated by TECs that present peptide antigens on class I or class II major histocompatibility complex (MHC) molecules (26), specifically cortical TECs (cTEC) for positive selection and medullary TECs (mTECs) or dendritic cells for negative selection (27). During positive selection, only DP late cells with productive TCRs that interact with MHC peptide complexes survive. If DP late thymocytes bind to an MHC class I or II molecule, cells commit to the SP8 or SP4 lineage respectively.

However, thymocytes are later negatively selected if they express a TCR with too high of an affinity for self-antigens. After positive selection, thymocytes encounter mTECs, which exclusively express a gene called *AIRE* (autoimmune regulator) (27). *AIRE* enables promiscuous gene expression of proteins specific to tissues throughout the body that are not normally expressed elsewhere. Negative selection is also mediated through additional antigen-presenting cells (APC) such as dendritic cells. If SP cells bind too strongly to self-antigens, they are induced to undergo apoptosis. A significant portion of thymocytes die due to negative selection. Thus, negative selection induces central tolerance by preventing autoreactive T cells that could cause autoimmune diseases from exiting the thymus (27).

In mouse thymus, SP thymocytes mature further in the medulla and upregulate markers such as CD62L (L-selectin), a lymph-node homing receptor that promotes T cells to emigrate from

the thymus to peripheral lymph nodes (28). In human thymus, SP thymocytes initially express the CD45 RO isoform but switch to the CD45 RA isoform before thymic egress (29).

When activated in the periphery, most SP8 cells are cytotoxic T cells and actively kill infected or tumor cells, while most SP4 cells are helper T cells and support other immune cells; however, a subset of SP4 cells produced in the thymus are regulatory T cells (Treg) that suppress the immune system and facilitate immunological self-tolerance (30). Tregs express the transcription factor FoxP3 (Forkhead box P3) (30). Although most T cells that have a strong affinity for self-antigens are negatively selected, Tregs are an exception and survive despite possessing TCRs with a high affinity for self MHC peptide complexes. Tregs utilize the ability to recognize self-antigens to prevent autoimmunity and excessive inflammation.

In summary, early stages of thymocyte development are dependent on Notch signaling for T lineage commitment. After successful TCR alpha and beta rearrangement, the later stages of T cell development are directed by MHC-restricted TCR interactions with the thymic stroma. Thus, the ability of the adaptive immune system to specifically recognize foreign antigens relies on the thymus to provide a wide array of T cells with diverse functional TCRs.

The importance of in vitro T cell development

Developing T cells from stem cells *in vitro* is critical not only for the study of thymopoiesis, but also for the advancement of T cell immunotherapies. With age, the thymus involutes, or atrophies, and thymic stromal tissue is increasingly replaced by adipose tissue, resulting in diminished thymus size, architecture, and T cell output (31). Age-related decrease in thymic T cell output is linked to an increased incidence of infections and cancer (32). Additionally, involuted thymus tissue loses the capacity to maintain central tolerance and negatively select autoreactive T

cells, such that self-reactive T cells increase with age and predispose elderly to autoimmune diseases (33). As aging, autoimmune, and immunodeficiency disorders result in reduced, dysregulated, or absent thymic T cell production, generating T cells *in vitro* would be useful for reconstituting the immune system in immunocompromised patients and regulating autoimmune diseases (32, 34, 35).

In vitro-derived T cells could also be engineered for cancer immunotherapies. Cancer immunotherapy specifically harnesses the patient's own immune system to attack malignant tumors (35). Chimeric antigen receptor T-cells (CAR-T) is one promising form of immunotherapy, since the introduction of a CAR into SP8 T cells enhances their ability to target specific proteins highly expressed on the surface of a cancer cell type. CAR-T has been highly effective for patients with certain cancers, such as B cell leukemias and lymphomas (35).

Currently, CAR-T cells are genetically engineered using mature T cells collected from the patient's own blood. However, autologous T cells are often scarce, require *ex-vivo* expansion, are functionally impaired, have reduced *in vivo* activity after reinfusion into the patient, may have a mispairing between the transduced CAR-T and the endogenous TCR chain already present, or in extremely rare cases, may contain pro-leukemic mutations (34, 36-38). On the other hand, allogeneic T cells from healthy donors might recognize the recipient's cells as foreign, which could increase graft-versus-tumor activity but also increase the risk of graft-versus-host disease (GVHD) (34, 39). The need to personalize treatments for each patient is problematic due to issues with accessibility, scalability, and cost (40). An efficient, scalable, and GVHD-free method of generating engineered T cells would revolutionize immunotherapy treatment for patients.

A potential solution for improving CAR-T therapy is to develop engineered T cells from human stem cells *in vitro.* Unlike the potentially exhausted T cells circulating in the patient's

bloodstream, *in vitro* development would produce naïve antigen specific T-cells. Since HSPCs are not a self-renewing source and there are limited HSPCs available from a single donor, human pluripotent stem cells (PSC), which includes both human embryonic stem cells (hESC) and induced pluripotent stem cells (iPSC), would provide an unlimited, renewable source of cells (41). Moreover, PSCs can be easily and stably genetically modified, such that a pool of universal donor cells could be created by modifying the MHC genes to prevent rejection or ablating the TCR to prevent GVHD (41). Thus, to advance CAR-T and immunotherapies in general, there is a compelling need to improve current *in vitro* methods that are still limited in mature T cell yield and development, especially for human T cells.

Current in vitro methods for generating T cells from stem cells

Currently available models of *in vitro* T cell differentiation from HSPCs have revolutionized thymopoiesis studies, but the field continues to seek novel approaches to generate mature T cells more efficiently. Paving the way, fetal thymic organ cultures (FTOC) revealed that mature T cells could be made from explanted murine fetal thymic tissue cultures seeded with mouse or human HSPCs (42-44). On the other hand, FTOCs are technically challenging since they require primary murine fetal thymic tissue. Moreover, FTOCs do not efficiently support HSPCs from adult sources, such as mobilized peripheral blood (MPB) and bone marrow (BM), compared to HSPCs from fetal liver (45).

The breakthrough OP9-DL1 system demonstrated that a monolayer of stromal cells expressing DLL1 could support *in vitro* T cell development (46) (**Figure 1-2A**). However, T cell differentiation in the OP9-DL1 system still has limitations. For instance, standard OP9-DL1 cultures use serum-containing medium that introduces uncontrollable variability between

experiments (45). For human T cell differentiation, the OP9-DL1 system supports the development of early precursor T cells, but not mature human T cells. Again, fetal liver HSPCs show more efficient differentiation in OP9-DL1 cultures than adult MPB or BM-derived HSPCs (45). From mouse HSPCs, OP9-DL1 cultures produce mature SP8 T cells but not mature SP4 T cells.

The Crooks lab developed the artificial thymic organoid (ATO), a serum-free, three-dimensional (3D) culture system that allows human HSPCs to efficiently differentiate into mature and functional T cells (47) (**Figure 1-2B**). Instead of explanted fetal thymic tissue or the OP9-DL1 stromal line, the ATO uses another murine bone marrow stromal cell line called MS5 that is transduced with either DLL1 or DLL4. HSPCs from various sources were shown to differentiate efficiently in the ATO system, including human cord blood (CB), adult BM, adult MPB, and post-natal thymus (47). ATOs initiated with TCR-engineered HSPCs produced mature SP8 T cells that showed *in vitro* and *in vivo* antigen-specific toxicity (47). A limitation is that ATOs generate SP8 T cells, but not SP4 T cells from human HSPCs.

We also demonstrated that the ATO method produces mature T cells from human PSCs, including human ESCs and iPSCs (48). In addition to generating immunophenotypic populations identical to those seen in postnatal thymus, transcriptional data aligned PSC-derived T cells with primary naïve T cells (48). TCR-engineered PSCs seeded into the PSC-ATO system showed anti-tumor efficacy *in vitro* and *in vivo*. Thus, the PSC-ATO method could be used to create large-scale and off-the-shelf T cell therapies in the future. There are still limitations to the number of T cells that can be generated using the PSC-ATO method, and SP8 T cells are more efficiently produced than SP4 T cells.

Therefore, while there are several useful models available, further improvements are needed for both murine and human HSPC differentiation into T cells *in vitro*. The Crooks lab has

pioneered mature human T cell production using the ATO system. The work presented in Chapter 2 details the adaptation of the ATO method specifically for murine T cell differentiation.

Metabolism in T cell development

Genes encoding metabolic enzymes were widely considered to function as "house-keeping genes," though these genes are spatially and temporally regulated throughout development. There is increasing evidence that metabolic changes during development do not only control cellular energy, but also the availability of metabolites that play active signaling roles promoting epigenetic changes and cellular differentiation (49). For instance, the Banerjee lab established that in order for the mouse embryo to progress past the zygotic genome activation stage, certain mitochondrial tricarboxylic acid (TCA) cycle metabolites must first localize to the nucleus to direct epigenetic remodeling (50). Metabolite dysregulation, on the other hand, can drive malignant transformation by disrupting the epigenetic landscape and cell differentiation.

Targeting metabolism has gained interest as a method to boost immune cell differentiation and function. Studies have predominantly concentrated on HSPCs and peripheral T cells, not on thymic T cell differentiation (51, 52). It is well known that the metabolic state of HSPCs is intimately tied to their function and ability to engraft bone marrow after transplantation (53). Mitochondrial quality control especially affects HSPC self-renewal and fate decisions (54). T cells also switch on specific metabolic pathways as they differentiate into specialized effector cell types. For instance, promoting fatty acid oxidation enhances regulatory and memory CD4 T cell formation in contrast to other effector cells (51, 55, 56). After activation, naïve T cells undergo "metabolic reprogramming," in which they engage both glycolysis and oxidative phosphorylation to generate necessary metabolic intermediates (51). Transcriptional, proteomics, and metabolomic

profiling have revealed that the massive upregulation of glycolytic and mitochondrial pathways in response to T cell receptor (TCR)-mediated antigen recognition is critical for activated T cell function (57, 58). Metabolomics and proteomics in aged T cells revealed defective mitochondrial respiration and one-carbon metabolism upon activation resulting in decreased T cell proliferation and cytokine production; notably, addition of one-carbon metabolites enhanced the response of aged T cells to activation (59).

Similar integrative metabolic studies are lacking for thymic T cell differentiation, especially human thymopoiesis. Studying metabolic changes during human thymus development has faced several challenges. Metabolic measurements are difficult to achieve in complex tissues, cell-lines cannot capture progressive developmental phases, and previous *in vitro* T cell differentiation models did not support the development of mature human T cells. Metabolic parameters have been measured mostly in mouse models and early DN thymocytes or egressing T cells (60-62), but no studies have characterized the metabolic changes that occur throughout T cell development in mouse or human thymus.

Current understanding of thymocyte metabolism has been primarily shaped by transcriptional and genetic perturbation studies in murine thymus. The Immunological Genome Project Consortium (ImmGen) investigated microarray data in murine thymus and revealed a global transcriptional shutdown of "housekeeping" metabolic genes and *Myc* expression at the DP stage (63). Studies have shown that perturbing specific genes involved in metabolic pathways, particularly *Glut1, Raptor*, *Pkm2*, *Pparδ*, *Mpc1*, *Opa1*, and *Rpl22*, affects the DN to DP transition in murine thymocytes (61, 64-69).

For instance, a combination of NOTCH1, IL-7 receptor (IL-7R), pre-TCR, and mechanistic target of rapamycin complex1 (mTORC1) signals induce committed DN3 cells to

upregulate glycolytic metabolism, proliferate, and determine cell fate decisions toward the αβ versus γδ T cell lineage (60, 61, 70). Inhibiting glycolytic metabolism through loss of the glycolytic enzyme PKM2 blocked progression of DN3 cells to the DP stage (65), and loss of the mTORC1 component RAPTOR (regulatory-associated protein mTOR) prevented αβ and promoted γδ T cell commitment (61).

Control of mitochondria has also been shown to be critical for T cell progression between the DN3 to DP stage, as well as in T cells that have left the thymus. Removal of protein OPA1 (optic atrophy 1), which controls mitochondrial biogenesis and respiration, impairs respiration and cell number of DN3 cells, and affects the metabolism and function of mature memory T cells in the periphery (68). Independent studies showed that SP4 T cells undergo metabolic quiescence and are required to downregulate their mitochondrial content in order to exit the thymus into the periphery (62), and recent thymic emigrant (RTE) SP8 T cells have diminished mitochondrial mass upon activation compared to SP8 T cells that have matured in the periphery (71).

Hence, modulating metabolic programs is known to promote self-renewal of HSPCs, induce naïve peripheral T cells to differentiate into distinct effector T cells (55, 56), and metabolite addition improves the function of peripheral T cells from aged mice (59). Previous studies suggest that the control of glycolytic and oxidative phosphorylation programs play a critical role in early T cell development and peripheral T cell maturation, but studies have been mostly limited to mouse thymus (51, 70). Understanding metabolism during thymopoiesis is also important for developing immunotherapy strategies. Compared to genetic modifications in stem cells, manipulating a chemically defined culture media is ideal for the clinical translation of *in vitro*-derived engineered T cells. However, metabolic studies are lacking for T cell development in the human thymus. The

project presented in Chapter 3 provides the first in-depth and comprehensive study of mouse and human thymic T cell development *in vivo* and *in vitro*.

Figures

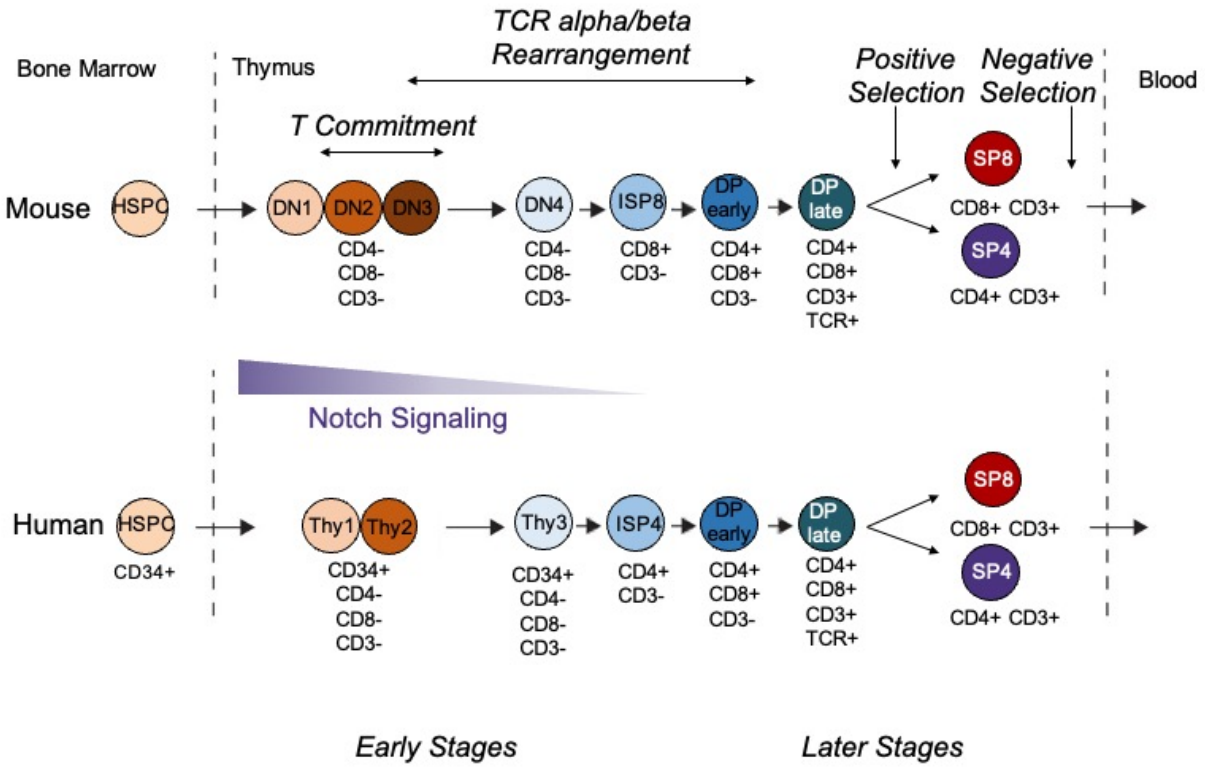

Figure 1-1. Overview of T cell development in mouse and human thymus

Schematic showing the parallels and differences between murine and human T cell development. HSPCs enter the thymus and encounter Notch ligands that instruct progenitors to commit to the T cell lineage by the end of the DN stages (DN1-4 in mouse; Thy1-3 in human). Early progenitors are identified as CD34+ in human. After the ISP stage (ISP8 in mouse; ISP4 in human), cells that successfully rearrange their TCRαβ subunits progress to the DP stages, which are further separated by the expression of the mature thymocyte CD3 marker. DP thymocytes undergo positive selection and develop into SP8 or SP4 T cells. After negative selection, mature SP T cells egress the thymus and enter the periphery.

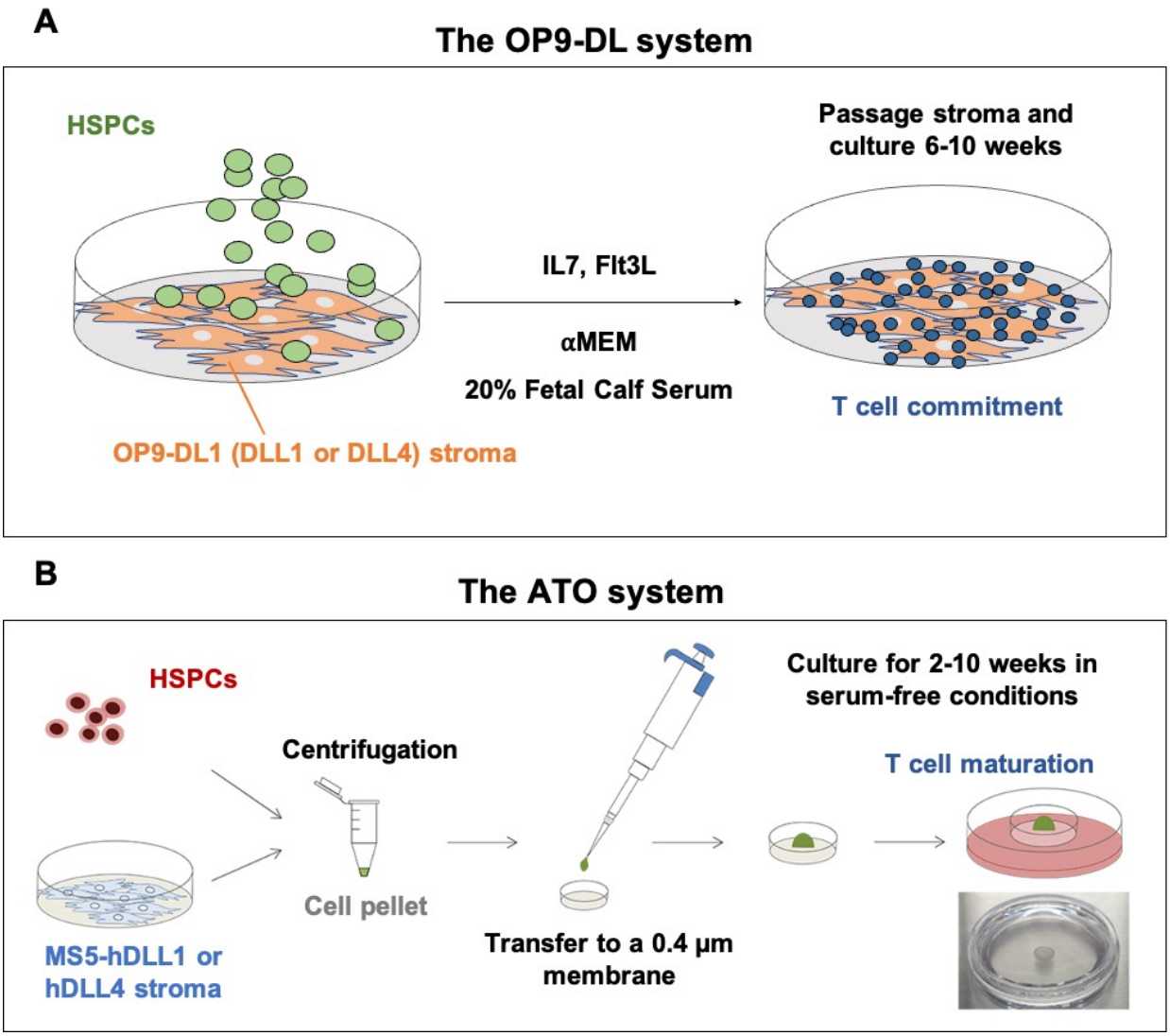

Figure 1-2. Stromal *in vitro* T cell differentiation systems

(**A**) The OP9-DL system consists of HSPCs grown on a 2D monolayer of OP9 stroma expressing mouse or human Notch-ligands (DLL1 or DLL4) with growth factors and serum-containing media; the culture requires frequent passaging of the 2D stromal cells.

(**B**) The artificial thymic organoid (ATO) system consists of human HSPCs aggregated in a 3D structure with a supportive MS5 stromal cell line expressing human Notch-ligands (hDLL1 or hDLL4). The organoid is plated on a 0.4 µm membrane that floats in 1 mL of serum-free media and can be cultured for several weeks without being disrupted.

Chapter 2 – *In vitro* recapitulation of murine thymopoiesis from single hematopoietic stem cells

Abstract

We report a serum-free, 3-D murine artificial thymic organoid (M-ATO) system that mimics normal murine thymopoiesis with the production of all T cell stages, from early thymic progenitors to functional single positive (CD8SP and CD4SP) TCRαβ and TCRγδ cells. RNA sequencing aligns M-ATO-derived populations with phenotypically identical primary thymocytes. M-ATOs initiated with *Rag1*$^{-/-}$ marrow produce the same differentiation block as seen in the endogenous thymus, and Notch signaling patterns in M-ATOs mirror primary thymopoiesis. M-ATOs initiated with defined hematopoietic stem cells (HSCs) and lymphoid progenitors from marrow and thymus generate each of the downstream differentiation stages allowing the kinetics of T cell differentiation to be tracked. Remarkably, single HSCs deposited into each M-ATO generate the complete trajectory of T cell differentiation producing diverse TCR repertoires across clones that largely match endogenous thymus. M-ATOs represent a highly reproducible and efficient experimental platform for the interrogation of clonal thymopoiesis from HSCs.

Introduction

Commitment to the T-cell lineage begins in the thymus from stem and progenitor cells that have trafficked from the bone marrow, and is induced by complex spaciotemporal interactions between precursor T cells and thymic epithelial cells, thymic mesenchyme and other hematopoietic cells (7-9). Among these interactions, Notch signaling from ligands in the thymic stroma (specifically Delta-like ligand 4 (DLL4)) is critical for the exclusive commitment of the

progenitor cells to the T cell lineage (6, 72, 73). Several *in vitro* systems have been developed to try to mimic the thymic microenvironment's ability to induce and maintain T-cell commitment and differentiation (46, 74, 75). Among them, the OP9-DL1 monolayer co-culture system revolutionized the field allowing the commitment of hematopoietic stem and progenitor cells (HSPCs) to the T cell lineage in a dish (46). However, monolayer systems have shown limitations: positive selection and thus production of mature TCRαβ$^+$ cells, especially CD4$^+$ T cells, is very limited. In addition, reproducibility is affected by variations in serum-containing medium.

We have recently developed an artificial thymic organoid (ATO) model of *in vitro* T cell differentiation from human HSPCs (47) as well as human pluripotent stem cells (48). Human ATOs reproducibly generate mature CD8 and CD4 T cells *in vitro* using 3D aggregates of hematopoietic stem and progenitor cells (HSPC) with a standardized Notch ligand-expressing stromal cell line in serum-free conditions. However, results using identical conditions with murine cells are suboptimal. We now report a modified ATO system that allows the highly efficient differentiation of murine bone marrow HSPCs to mature T cells *in vitro*. Murine ATOs (M-ATOs) mimicked normal murine thymopoiesis with the production of all immature and mature T cell subsets including TCRγδ$^+$ cells and conventional TCRβ$^+$ T cells (both CD8SP and CD4SP) and FoxP3$^+$ cells. Mature cells expressed CD62L, responded to TCR activation and exhibited a broad TCR Vβ repertoire consistent with positive selection. RNA sequencing of the different M-ATO-derived T cell subsets revealed a transcriptional profile highly similar to that of primary T cell populations from the murine thymus. M-ATOs could recapitulate thymopoiesis from different subsets of BM and thymus progenitor populations. The high efficiency of the M-

ATO system allowed the production of millions of T cells with a diverse repertoire from single highly purified HSCs.

Thus, murine ATOs are a technically simple, highly reproducible, and comprehensive platform to study the full range of murine T cell development and maturation from single hematopoietic stem cells and progenitors.

Materials and Methods

Cell lines

To generate MS5-mDLL4, MS5 cells (76) were transduced with a lentiviral vector encoding full-length murine *DLL4* with or without enhanced green fluorescent protein (eGFP). The full-length coding sequence of murine *DLL4* was synthesized (Integrated DNA Technologies, Skokie, IL) and cloned into the third-generation lentiviral vector pCCL-c-MNDU3 (gift from Dr. Donald Kohn, UCLA) with or without IRES-linked eGFP expression. Packaging and concentration of lentivirus particles was performed as previously described (47). The highest 5% DLL4-expressing cells were sorted by FACS using an anti-DLL4 antibody (**Biolegend, Cat# 130813**) and passaged in Dulbecco's Modification of Eagle's Medium (DMEM) (**Cellgro, Cat# 10-017-CV**) 10% fetal calf serum (FCS) (**Gemini, Cat# 900-208**). Stable expression was confirmed by flow cytometry for DLL4 expression or GFP expression after several weeks of culture, as well as qRT-PCR and DNA sequencing.

Mice

All animal experiments were conducted under a protocol approved by the UCLA Chancellor's Animal Research Committee. This study used 1–4-month-old mice of different backgrounds from Jackson Laboratory (Bar Harbor, Maine): C57BL/6 (**Cat# JAX:000664**) (including Foxp3-GFP (**JAX:006772**) mice and RAG1$^{-/-}$ mice **(JAX:002216)**), C3H/He **(JAX:000659)**, BALB/c **(JAX:000651)** and FVB (including Transgenic Notch Reporter mice **(JAX:020942)**) mice. Mice from both sexes were randomly allocated to experimental groups.

Isolation of murine bone marrow HSPCs for M-ATO culture

Fresh or frozen bone marrow cells were enriched for hematopoietic stem and progenitor cells by negative cells selection of Lin- cells by magnetic cell sorting (MACS) using Murine Lin depletion Kit (**Miltenyi, Auburn CA, Cat# 130-110-470**). Hematopoietic stem and progenitor cells were isolated by FACS sorting using the phenotypes as follow: (Lin$^-$ stands for: Ter119$^-$, TCRγδ$^-$, B220$^-$, CD19$^-$, CD11c$^-$, CD11b$^-$, Gr1$^-$, NK1.1$^-$, CD5$^-$, CD4$^-$, CD8$^-$, CD3$^-$).

Name of cell population	**Phenotype**
LSK (Lin$^-$ Sca1$^+$ cKit$^+$)	Lin$^-$ Sca1$^+$ cKit$^+$
HSC (Hematopoietic Stem Cell)	Lin$^-$ Sca1$^+$ cKit$^+$ CD48$^-$ CD150$^+$ IL7R$^-$
MPP (MultiPotent Progenitor)	Lin- Sca1$^+$ cKit$^+$ CD48$^-$ CD150$^-$ IL7R$^-$
LMPP (Lymphoid-primed MultiPotent Progenitor)	Lin- Sca1$^+$ cKit$^+$ IL7R$^+$ Flk2$^+$
CLP (Common Lymphoid progenitor)	Lin- Sca1^{Lo} cKit^{Lo} IL7R$^+$ Flk2$^+$

Sorted cells were immediately seeded into MS5-mDLL4 M-ATOs, as described below.

Murine artificial thymic organoid (M-ATO) cultures

M-ATOs were generated as previously described (47). MS5-mDLL4 cells were harvested by trypsinization and resuspended in serum free M-ATO culture medium ("D/F12-B27") composed of DMEM-F12 (**Gibco, Cat# 11320033**) (in some experiments, RPMI 1640 (**CellGro, Cat# 10-040-CV**) was used as basal media as indicated), 2% B27 supplement (**ThermoFisher Scientific, Grand Island, NY, Cat# 17504-044**) (in some experiments, 4% B27 was used as indicated), 30 μM L-ascorbic acid 2-phosphate sesquimagnesium salt hydrate (**Sigma-Aldrich, St. Louis, MO, Cat# A8960-5G**) reconstituted in PBS, 1% penicillin/streptomycin (**Gemini Bio-Products, West Sacramento, CA, Cat# 400-109**), 1% Glutamax (**ThermoFisher Scientific, Grand Island, NY, Cat# 35050-061**), 5 ng/ml rmFLT3L (**Peprotech, Rocky Hill, NJ, Cat# 250-31L**), 5 ng/ml rmIL-7 (**Peprotech, Cat# 217-17**), 10 ng/ml rmSCF (Peprotech, **Cat# 250-03**) (SCF was added only for the first week of culture) and beta mercaptoethanol (BME) (0.05mM) (**Sigma-Aldrich, Cat# M7522**). D/F12-B27 was made fresh weekly. $1.5x10^5$ MS5-mDLL4 cells were combined with purified murine HSPC cells (1- 4000 cells / ATO) in 1.5 ml Eppendorf tubes and centrifuged at 300 *g* for 5 min at 4˚C in a swinging bucket centrifuge. Supernatants were carefully removed, and the cell pellet was resuspended in 5 μl D/F12-B27 per M-ATO and mixed by brief vortexing. M-ATOs were plated on a 0.4 μm Millicell transwell insert (**EMD Millipore, Billerica, MA; Cat. PICM0RG50**) placed in a 6-well plate containing 1 ml D/F12-B27 per well. Medium was changed completely every 3-4 days by aspiration from around the cell insert followed by replacement with 1 ml with fresh D/F12-B27/cytokines. M-ATO cells were harvested by adding FACS buffer (PBS/0.5% bovine serum album/2mM EDTA) to each well and briefly disaggregating the M-ATO by pipetting with a 1 ml "P1000" pipet, followed by passage through a 50 μm nylon strainer.

For single cell M-ATO cultures, LSK or HSC cells were isolated as single cells in a 96-conical bottom plate in 200ul of D/F12-B27 medium by flow cytometry cell sorting (FACS ARIA). After centrifugation, $1.5x10^5$ MS5-mDLL4 cells were added in each well of the 96 well plate. The plate was then centrifuged at 300 *g* for 5 min at 4˚C. Supernatants were carefully removed, and each cell pellet was resuspended in 5 µl D/F12-B27 and plated on a 0.4 µm Millicell transwell insert as described above.

Isolation of murine thymocytes, splenocytes and M-ATO-derived cells

Thymic and spleen fragments from the mouse thymus were finely dissected in FACS buffer (PBS/0.5% bovine serum album/2mM EDTA) and disrupted by pipetting to release thymocytes into suspension, followed by passage through a 70 µm nylon strainer. Cells were then stained for flow cytometry.

M-ATO-derived T cells were harvested by adding FACS buffer (PBS/0.5% bovine serum album/2mM EDTA) to each cell insert and briefly disaggregating the M-ATO by pipetting with a 1 ml "P1000" pipet, followed by passage through a 70 µm nylon strainer. Cells were then stained for flow cytometry.

Flow cytometry cell sorting of thymic and M-ATO-derived T cell populations used the following surface phenotypes: (Lin^- stands here for: $Ter119^-$, $TCR\gamma\delta^-$, $B220^-$, $CD19^-$, $CD11c^-$, $CD11b^-$, $Gr1^-$, $NK1.1^-$).

Name of cell population	**Phenotype**
ETP (Early Thymic Progenitor)	Lin^- $CD4^-$ $CD8^-$ $c\text{-}Kit^{hi}$ $CD44^{hi}$ $CD25^-$
DN2	Lin^- $CD4^-$ $CD8^-$ $c\text{-}Kit^{hi}$ $CD44^{hi}$ $CD25^+$
DN3	Lin^- $CD4^-$ $CD8^-$ $CD44^-$ $CD25^+$

ISP8	Lin^- $CD4^-$ $CD8^+$ $CD3^-$
DP early	Lin^- $CD4^+$ $CD8^+$ $CD3^-$ $TCR\beta^-$
DP late	Lin^- $CD4^+$ $CD8^+$ $CD3^+$ $TCR\beta^+$
CD8SP	Lin^- $CD4^-$ $CD8^+$ $CD3^+$ $TCR\beta^+$ $CD62L^+$
CD4SP	Lin^- $CD4^+$ $CD8^-$ $CD3^+$ $TCR\beta^+$ $CD62L^+$

TCR Vβ expression analysis by flow cytometry

Total cells isolated from pooled M-ATOs or murine thymi were stained for Lin (Ter119, TCRγδ, B220, CD19, CD11c, CD11b, Gr1, NK1.1), CD3, CD4, CD8, in conjunction with the anti-mouse TCR Vβ Screening panel (**BD, Biosciences, Cat# 557004**). Lin^- $CD3^+CD8^+CD4^-$ cells and Lin^- $CD3^+CD8^-CD4^+$ cells were gated for analysis, and Vβ family usage was determined by percent $FITC^+$, representing a different Vβ antibody per tube, per the manufacturer's protocol.

T cell cytokine assays

Mature CD8SP and mature CD4SP cells from M-ATOs were isolated by magnetic negative selection using the $CD8^+$ T Cell Isolation Kit (**Miltenyi Biotech, Cat# 130-104-075**) and the $CD4^+$ T cell Isolation Kit (**Miltenyi Biotech, Cat# 130-104-454**) respectively and sorted by FACS or magnetic selection (**Miltenyi Biotech, Cat# 130-091-7558**) to further isolate CD8SP $CD62L^+$ cells and CD4SP $CD62L^+$ cells. Purified T cell populations were plated in 96-well U-bottom plates in 200 µl RPMI 1640 (**CellGro, Cat# 10-040-CV**) with 5% fetal calf serum (**Hyclone, Cat# SH30070.03**) and 0.05mM beta mercaptoethanol (BME) (**Sigma-Aldrich, Cat# M7522**). PMA/ionomycin/protein transport inhibitor cocktail or control protein transport inhibitor cocktail (**eBioscience, San Diego, CA, Cat# 00-4975-03**) were added to each well and incubated for 6h.

Cells were washed and stained for CD3, CD4, and CD8 (**Biolegend, San Diego, CA**) prior to fixation and permeabilization with an intracellular staining buffer kit (**eBioscience, San Diego, CA, Cat# 88-8824-00**) and intracellular staining with antibodies against IFNγ, TNFα, and IL-2 (**Biolegend, San Diego, CA).**

T cell activation and proliferation assays

For Cell Trace Violet (CTV) cell proliferation assays, M-ATO-derived CD8SP and CD4SP T cells were isolated as described above and labeled with 5 μM CTV (**Invitrogen, Cat# C34557**). Labeled cells were incubated with anti-CD3/CD28 beads per manufacturer's protocol (**ThermoFisher Scientific, Grand Island, NY, Cat# 11456D**) in RPMI 1640 (**CellGro, Cat# 10-040-CV**) with 5% fetal calf serum (**Hyclone, Cat# SH30070.03**) and 0.05mM beta mercaptoethanol (BME) (**Sigma-Aldrich, Cat# M7522**) with 20 ng/ml rmIL-2 (**Peprotech, Rocky Hill, NJ, Cat#** 212-12), and plated in 200 μl per well of 96-well round-bottom plates. On day 3, cells were washed and stained for CD25 (**Biolegend, San Diego, CA**) and analyzed by flow cytometry.

Immunofluorescence imaging of M-ATOs

M-ATOs were fixed in 4% Formaldehyde (**Sigma-Aldrich, Cat# F8775**) for 30 minutes at room temperature followed by 3x10 min washes in PBST (0.3% Triton X-100) and a 1-hour block in PBST/BSA (2% BSA). M-ATOs were stained with anti-CD8a (**clone 53-6.7; Biolegend**) and anti-mDLL4 (**clone HMD4-1; Biolegend**) at a 1:100 dilution, anti-CD4 (**clone RM4-5; Biolegend**), anti-GFP (**clone FM264G; Biolegend**) at a 1:100 dilution, anti-CD3 (**clone 145-2C11; Biolegend**) at a 1:50 dilution overnight at 4 ºC. Secondary antibodies AlexaFluor-594-

conjugated anti-rat IgG (H+L) (**Jackson ImmunoResearch, Cat# 712-585-150**) or AlexaFluor-488-conjugated anti-rat IgG (H+L) (**Jackson ImmunoResearch, Cat# 712-485-153**) were added at a 1:200 dilution for 2 hours at room temperature. For anti-mDLL4, anti-hamster biotin (**Jackson ImmunoResearch, Cat# 127-065-160**) was added at a 1:500 dilution for 2 hours at room temperature, and then AlexaFluor-594-conjugated Streptavidin (**Jackson ImmunoResearch, Cat# 016-580-084**) was added at a 1:800 dilution for 30 minutes at room temperature. Each M-ATO was mounted individually in Vectashield Antifade Mounting Medium (**Vector Laboratories, Cat# H1000**) on a concavity microscope slide (**Fisher Scientific**). Immunofluorescence images were acquired on a Zeiss LSM 880 confocal microscope equipped with Airyscan and Zen software (**Zeiss**).

Flow cytometry

All flow cytometry stains were performed in PBS/0.5% BSA/2 mM EDTA for 20 min on ice. TruStain FcX (**Biolegend, San Diego, CA, Cat#101320**) was added to all samples for 5 min prior to antibody staining. DAPI (**Life technologies, Cat# D1306**) was added to all samples (except intracellular staining) prior to analysis.

For intracellular cytokine expression analysis, cells were stained for surface markers prior to fixation and permeabilization with the True-Nuclear Transcription Factor Buffer Set (**Biolegend, San Diego, CA, Cat# 424401**) followed by intracellular staining with cytokine antibodies.

Analysis was performed on an LSRII Fortessa, and FACS sorting on FACSARIA or FACSARIA-H instruments (**BD Biosciences, San Jose, CA**) at the UCLA Broad Stem Cell Research Center Flow Cytometry Core.

For all analyses (except intracellular staining) $DAPI^+$ cells were gated out, and single cells were gated based FSC-H vs. FSC-W and SSC-H vs. SSC-W.

Anti-mouse antibody clones used for surface and intracellular staining were obtained from **Biolegend (San Diego, CA)** or **Miltenyi Biotech**.

Flow cytometry antibody	**SOURCE**	**IDENTIFIER**
Anti-mouseCD3 (Clone145-2C11)	Biolegend	Cat# 100312, RRID:AB_312677
Anti-mouse CD4 (Clone RM4-5)	Biolegend	Cat# 100550, RRID:AB_2562099
Anti-mouse CD5 (Clone 53-7.3)	Biolegend	Cat# 100627, RRID:AB_2563930
Anti-mouse CD8a (Clone 53-6.7)	Biolegend	Cat# 100708, RRID:AB_312747
Anti-mouse CD11b (Clone M1/70)	Biolegend	Cat# 101228, RRID:AB_893232
Anti-mouse CD11c (Clone N418)	Biolegend	Cat# 117328, RRID:AB_2129641
Anti-mouse CD16/32 (TruStain FcX) (Clone 93)	Biolegend	Cat# 101320, RRID:AB_1574975
Anti-mouse CD19 (Clone 1D3/CD19)	Biolegend	Cat# 152406, RRID:AB_2629815
Anti-mouse CD25 (PC61)	Biolegend	Cat# 102016, RRID:AB_312865
Anti-mouse CD27 (LG.3A10)	Biolegend	Cat# 124226, RRID:AB_2565792
Anti-mouse CD28 (37.5)	Biolegend	Cat# 102127, RRID:AB_2650628
Anti-mouse CD44 (IM7)	Biolegend	Cat# 103059, RRID:AB_2571953
Anti-mouse CD45 (clone 30-F11)	Biolegend	Cat# 103116, RRID:AB_312981
Anti-mouse CD45R/B220 (Clone RA3-6B2)	Biolegend	Cat# 103236, RRID:AB_893354
Anti-mouse CD62L (MEL-14)	Biolegend	Cat# 104438, RRID:AB_2563058

Anti-mouse Ly-6G/Ly-6C (Gr-1) (Clone RB6-8C5)	Biolegend	Cat# 108428, RRID:AB_893558
Anti-mouse NK1.1 (Clone PK136)	Biolegend	Cat# 108728, RRID:AB_2132705
Anti-mouse interferon γ (Clone XMG1.2)	Biolegend	Cat# 505806, RRID:AB_315400
Anti-mouse IL-2 (Clone JES6-5H4)	Biolegend	Cat# 503826, RRID:AB_2650897
Anti-mouse TCRβ (Clone H57-597)	Biolegend	Cat# 109234, RRID:AB_2562350
Anti-mouse TCRγδ (Clone GL3)	Biolegend	Cat# 118120, RRID:AB_2562566
Anti-mouse TNFα (Clone MP6-XT22)	Biolegend	Cat# 506339, RRID:AB_2563127
Anti-mouse TER-119 (clone Ter119)	Biolegend	Cat# 116228, RRID:AB_893636
Anti-mouse CD150 (Clone TC15-12F12.2)	Biolegend	Cat# 115941, RRID:AB_2629660
Anti-mouse CD117 (c-KIT) (Clone ACK2)	Biolegend	Cat# 135122, RRID:AB_2562042
Anti-mouse Ly-6A/E (Sca-1) (Clone D7)	Biolegend	Cat# 108114, RRID:AB_493596
Anti-mouse CD48 (Clone HM48-1)	Biolegend	Cat# 103432, RRID:AB_2561463
Anti-mouse CD127 (IL-7R) (Clone REA680)	Miltenyi Biotech	Cat# 130-122-938, RRID:AB_2783928
Anti-mouse CD135 (Flk-2) (Clone A2F10)	Biolegend	Cat# 135306, RRID:AB_1877217
Anti-mDLL4 (clone HMD4-1)	Biolegend	Cat# 130813, RRID:AB_2246026

Flow cytometry data were analyzed with FlowJo software (**Tree Star Inc.**).

RNA sequencing (RNA-seq) and data analysis

RNA was extracted from each of the indicated Thymic or M-ATO-derived populations isolated by FACS, as described above, and total RNA isolated using the RNeasy Micro kit (Qiagen). (Lin^- stands here for: $Ter119^-$, $TCR\gamma\delta^-$, $B220^-$, $CD19^-$, $CD11c^-$, $CD11b^-$, $Gr1^-$, $NK1.1^-$).

Name of cell population	**Number of replicates (n)**	**Phenotype**
ETP thymus	2	Lin^- $CD4^-$ $CD8^-$ c-Kit^{hi} $CD44^{hi}$ $CD25^-$
ETP M-ATO	2	Lin^- $CD4^-$ $CD8^-$ c-Kit^{hi} $CD44^{hi}$ $CD25^-$
DN2 thymus	2	Lin^- $CD4^-$ $CD8^-$ c-Kit^{hi} $CD44^{hi}$ $CD25^+$
DN2 M-ATO	2	Lin^- $CD4^-$ $CD8^-$ c-Kit^{hi} $CD44^{hi}$ $CD25^+$
DN3 thymus	2	Lin^- $CD4^-$ $CD8^-$ $CD44^-$ $CD25^+$
DN3 M-ATO	2	Lin^- $CD4^-$ $CD8^-$ $CD44^-$ $CD25^+$
ISP8 thymus	2	Lin^- $CD4^-$ $CD8^+$ $CD3^-$
ISP8 M-ATO	2	Lin^- $CD4^-$ $CD8^+$ $CD3^-$
DP early thymus	2	Lin^- $CD4^+$ $CD8^+$ $CD3^-$ $TCR\beta^-$
DP early M-ATO	2	Lin^- $CD4^+$ $CD8^+$ $CD3^-$ $TCR\beta^-$
DP late thymus	2	Lin^- $CD4^+$ $CD8^+$ $CD3^+$ $TCR\beta^+$

DP late M-ATO	2	Lin^- $CD4^+$ $CD8^+$ $CD3^+$ $TCR\beta^+$
CD8SP thymus	2	Lin^- $CD4^-$ $CD8^+$ $CD3^+$ $TCR\beta^+$ $CD62L^+$
CD8SP M-ATO	2	Lin^- $CD4^-$ $CD8^+$ $CD3^+$ $TCR\beta^+$ $CD62L^+$
CD4SP thymus	2	Lin^- $CD4^+$ $CD8^-$ $CD3^+$ $TCR\beta^+$ $CD62L^+$
CD4SP M-ATO	2	Lin^- $CD4^+$ $CD8^-$ $CD3^+$ $TCR\beta^+$ $CD62L^+$

1.5 ng of total RNA was input to generate sequencing libraries with SMARTer Stranded Total RNA-Seq (Pico) Kit (Clonetech, Cat. 635005). Paired-end 150 bp sequencing was performed on an Illumina HiSeq 3000. A total of 32 libraries were multiplexed and sequenced in 5 lanes. Raw sequence files are available at NCBI's Gene Expression Omnibus (GSE146224). An independent set of RNA-Seq libraries for thymic subsets generated by the Immgen consortium (GSE127267) was downloaded from NCBI's Gene Expression Omnibus (Bioproject ID PRJNA429735) and analyzed in-house (**Table S2-1**).

The STAR ultrafast universal RNA-seq aligner v2.7.0d (77) was used to align the reads to a genome index that includes both the genome sequence (GRCm38 mouse primary assembly) and the exon/intron structure of known mouse gene models (Gencode M20 comprehensive genome annotation). Alignment files were used to generate strand-specific, gene-level count summaries with STAR's built-in gene counter. Data from the Immgen dataset was not strand-specific. Independent filtering was applied as follows: genes with less than half-count per million in all samples, count outliers or low mappability (<50bp) were filtered out for downstream analysis (20, 78). This masked set included a total of 13760 mouse protein coding genes.

Expression estimates provided throughout were computed in units of fragments per kilobase of mappable length and million counts (FPKMs). Count-based normalized and variance-stabilized data was used for all ordination, differential and clustering analyses, and all figures unless otherwise noted.

Principal component analysis (PCA, Figure 4A-B) was performed with the function prcomp in R (https://www.R-project.org/) using standardize data as input. To facilitate the integration of in-house and external datasets, standardization was performed independently prior to PCA.

Differential expression analyses was performed with DESeq2 (Bioconductor, v3.7, RRID:SCR_015687)(78). We performed pair-wise comparisons between and within thymocyte subsets from both thymic and M-ATO. We defined a set of 2554 variable genes for further analyses as: fold-change greater than 4, Benjamini-Hochberg adjusted Wald test p-value less than 0.01 in at least one pair-wise test, and a minimum expression of 4 FPKMs in at least one sample. This set of most variable genes was then subjected to model-based clustering using MBCluster.Seq (79) to classify them based on their overall abundance profile across populations (**Figure 2-4C-D**). We set the starting number of clusters to 100, and then manually merged them to generate a set of 26 non-redundant gene classes (**Table S2-1**).

Functional enrichment for genes selected in the tests and clusters above was performed with Metascape (80).

Fold changes between two developmentally proximal populations were employed to perform Gene Set Enrichment Analysis (81) using gene expression signatures from independent studies (Figure S4). We analyzed the following transitions in both M-ATO-derived and thymic populations from this study: the *ETP/DN2* transition from our samples was compared against the

"ETP < DN2" (higher expression in DN2) and "ETP > DN2" (higher expression in ETP) signatures from the Molecular Signature Database (MSigDB) and similarly for *DN2/DN3* (MSigDB: DN2 > DN3, DN2 < DN3). For the *ISP/DPearly* transition we employed a signature for the most regulated genes between double negative and double positive cells (MSigDB: DN > DP, DN < DP). For the *DPlate/CD4SP* and *DPlate/CD8SP* transitions we retrieved a signature from the Immgen microarray database (63) with genes most differential between $DP69^+$ cells (double positive $CD69^+$ cells, early positive selection) and $4SP24^-$ ($CD4^+$ single positive $CD24^-$ mature T-cells) or $8SP24^-$ ($CD8^+$ single positive $CD24^-$ mature T-cells) respectively. Finally, the divergence between our *CD4SP* and *CD8SP* single positive populations in both M-ATOs and thymus was compared against a signature from the $4SP24^-$ vs. $8SP24^-$ mature thymic T-cells contrast from Immgen. Each of the previous signatures typically included a list of the 150 to 200 most up- or down-regulated genes between any two populations. All plots in Figure 4 and Figure S4 were generated in Matlab (MATLAB, version release 2017a, The MathWorks, Inc, RRID:SCR_001622).

Data and Code Availability

The Gene Expression Omnibus (GEO) accession number for the RNA sequencing data reported in this paper is GEO: GSE146224.

Quantification and statistical analysis

In all figures, *n* represents independent experiments and data are represented as mean ± standard deviation (s.d.) or mean ± standard error of the mean (SEM) as indicated. Statistical analysis was performed using GraphPad Prism software and *p*-values were calculated from the two-tailed unpaired *t* test or multiple t-test. The *p*-values are directly indicated on the figure,

above the corresponding graphs. *$p< 0.05$; **$p< 0.01$; and ***$p< 0.001$ were considered statistically significant.

Results

Murine ATOs recapitulate the early stages of murine T cell development

To generate a robust and highly reproducible *in vitro* system that supports the earliest stages of murine T cell commitment as well as positive selection, we modified our previously developed serum-free ATO model (47, 48). MS5 stromal cells transduced with murine DLL4 (hereafter referred to as MS5-mDLL4) were aggregated with murine HSPCs (defined as Lin- $Sca1^+$ $cKit^+$ hereafter referred to as LSK) from fresh or frozen C57BL/6 murine young adult (1-4 months) bone marrow and deployed on a cell culture insert at the air-liquid interface (**Figure 2-1A**).

In contrast to human ATOs, we identified DMEM-F12 as the optimal basal medium for murine cultures (**Figure S2-1A**). As in the human system, we used the B27 supplement as a replacement for fetal calf serum. This serum-free medium (hereafter referred to as D/F12-B27) was supplemented for the entire culture period, with Fms-related tyrosine kinase 3 (Flt3L), Interleukin (IL)-7, ascorbic acid, and beta mercapto-ethanol (BME) (**Figure 2-1A**); for the first week of culture Stem Cell Factor (SCF) was also added.

Murine ATOs (M-ATOs) induced commitment of HSPCs to the T cell lineage by week 2 while cells expressing markers of non-T cell lineages (CD11b, CD11c, GR1, CD19, B220 and NK1.1; hereafter referred to as Lin) decreased markedly (**Figure 2-1B**). M-ATOs rapidly produced γδ T cells which later decreased in frequency as conventional TCRβ T cells were generated. The Immature Single Positive $CD8^+$ (ISP8) and $CD8^+CD4^+$ double positive (DP) populations emerged

from the CD8-CD4- double negative (DN) cells between week 2 and week 3 and were maintained long term (**Figure 2-1B and 1C**).

Typically, cell numbers generated in M-ATOs peaked at week 3 with an average 12,000-fold increase when initiated with 500 LSK cells in a single ATO. Cell numbers slightly dropped at week 5 but remained constant until the end of the culture at week 8 (**Figure 2-1C**). Interestingly a lower concentration (2%) of B27 supplement to that used in the human system (4%) was beneficial for longer term cultures (**Figure S2-1B**).

We analyzed subsets of the $CD4^-$ $CD8^-$ double negative (DN) population over time using the standard CD44 and CD25 markers (10) (**Figures 2-1B, 1D and 1E).** Daily analysis during the first 2 weeks of culture demonstrated progression of the cultures from the DN1 through DN4 stages with DN3 cells predominating after the first week of culture (**Figure 2-1D and 1E**). A detailed analysis of the earliest stages using c-kit expression as described by the Rothenberg group (12), further delineated progression through early thymic progenitors (ETP), DN2a and DN2b populations (**Figure 2-1E and Figure S1C**). DN3a and DN3b subsets could also be discriminated based on either CD28 expression (82) or intracellular TCRβ (iTCRβ) (73, 83) (**Figure S2-1D**).

T cell maturation in murine ATOs

Analysis of more mature T cells demonstrated the emergence of $CD3^+TCR\beta^+$ cells between week 2 and week 3 of culture. This population was maintained throughout culture and contained $CD4^+CD8^+$ (DP), $CD4^-$ $CD8^+$ (CD8SP) and $CD8^-CD4^+$ (CD4SP) mature T cells (**Figure 2-2A and 2B**). A population of $CD3^+CD4^-CD8^-$ cells consistent with previously described innate T cells (84, 85) was also observed (**Figure 2-2A**).

40-80% of CD8SP T cells and 5-15% of CD4SP T cells displayed a $CD62L^+$ $CD44^{lo}$ phenotype consistent with conventional mature naïve T cell phenotype produced in the normal thymus (86-88) (**Figure 2-2C**). CD8SP and CD4SP $CD62L^+$ cells exhibited polyfunctional production of interferon (IFN)- γ, tumor necrosis factor alpha (TNF-α) and IL-2 in response to phorbol 12-myristate13-acetate (PMA) and ionomycin (**Figure 2-2D**). Both CD8SP and CD4SP proliferated and upregulated the activation marker CD25 in response to anti-CD3/CD28 and IL-2 stimulation (**Figure 2-2E**). Immunofluorescence staining of whole mounted M-ATOs at week 4 demonstrated abundant $CD4^+$ and $CD8^+$ T-lineage cells interspersed with MS5-mDLL4 stromal cells (**Figure 2-2F**). Further analysis demonstrated the presence of DP, CD8SP and CD4SP cells (**Figure S2-2A and S2B**).

M-ATOs do not contain thymic epithelial cells which are responsible for the selection of CD4SP in the thymus through MHC class II expression. Consistent with this, CD4SP were produced at lower frequency compared to the thymus (**Figure 2-2B**). We hypothesized that the ability to generate any CD4SP in M-ATOs was made possible by positive selection mediated via MHC-Class II expressing hematopoietic cells generated from the HSPC that initiated the ATOs. Indeed, the analysis of non-T lineage cells in 5-week M-ATOs revealed that a small percentage of cells belonged to the myeloid lineage and that some expressed MHC Class II molecules. As in the human system, M-ATOs produced some dendritic cells but no B cells were detected in M-ATOs after 5 weeks (**Figure S2-2C**).

FoxP3 (Forkhead box P3) is a transcription factor specifically expressed in $CD4^+CD25^+$ regulatory T cells and required for their development (89). Six weeks after initiating M-ATOs with LSK cells from FoxP3 reporter mice, a subset of the CD4SP cells co-expressed GFP (Foxp3) and CD25, suggesting the production in M-ATOs of cells with a regulatory T cell (Treg) phenotype

(**Figure 2-2G**). Of the two phenotypic Treg precursors that have been described, $CD25^{neg}$ $Foxp3^{+}$ (90, 91) were at very low frequency whereas a robust population of $CD25^{+}$ $FoxP3^{-}$ (92) was detected (**Figure 2-2G**).

T cell differentiation and TCR diversity in M-ATOs using different murine backgrounds.

The studies described above were performed with bone marrow cells harvested from C57BL/6 mice. There are known intrinsic differences between murine strains in terms of blood cell and T cell development, including CD4SP/CD8SP predominance (93). To verify that the M-ATO model was applicable to other murine models, we compared the use of LSK cells harvested from the bone marrow of the C3H/He (the strain from which the MS5 stromal line was derived) (76), BALB/c and FVB murine strains. In all backgrounds, M-ATOs efficiently supported T cell differentiation although with slightly different kinetics (**Figure 2-3A and Figure S2-3A-C**). C3H/He and FVB strains generated more CD4SP cells than CD8SP, typical of normal thymopoiesis, whereas in M-ATOs from C57BL/6 and Balb/c, CD8SP predominated relative to CD4SP (**Figure 2-3A, Figure S2-3A-C**).

Analysis of TCR diversity via Vβ expression revealed that both the CD8SP and CD4SP cells generated in M-ATOs from the four different murine backgrounds exhibited a broad repertoire (**Figure 2-3B, Figure S2-3D**). Vβ5.1,5.2, Vβ11 and Vβ12 TCR-bearing T lymphocytes are known to be clonally eliminated, either completely or partially through negative selection in the thymi of C3H/He and BALB/c mice, but not in C57BL/6 or FVB mice (94-103). As expected, Vβ5.1,5.2, Vβ11 and Vβ12 expression was almost undetectable in endogenous thymocytes from C3H/He and BALB/c mice. In contrast, M-ATO-derived cells from C3H/He and BALB/c mice showed significantly increased cells expressing these Vβ segments (**Figure 2-3B and 3C**). M-

ATOs derived from control C57BL/6 or FVB strains in which Vβ5.1,5.2, Vβ11 and Vβ12 TCR segments are not negatively selected in the thymus showed similar expression of these segments in endogenous thymocytes and M-ATO-derived T cells (**Figure 2-3C**). These data are consistent with a lack of negative selection during M-ATO-induced T cell differentiation with the potential for survival of more self-reactive T cells in ATOs.

Transcriptional analysis of T-cell differentiation in M-ATOs

Principal component analysis (PCA) using global genome wide expression profiles for all populations from M-ATOs, thymus (THY hereafter) and the Immgen dataset (63) revealed the major transcriptional events known to operate during T cell development and the relatedness between thymic and M-ATO-derived populations (**Figure 2-4A).** The first principal component (PC1, 43% of total variance) fully correlated with the developmental progression from ETPs to positively selected cells. Top PC1-ranked genes (**Figure 2-4B**, left) included both legacy hematopoietic progenitor genes (*Cd34, Bcl11a, Hhex, Mpo and Spi1* among others) which were repressed after the ETP/DN2 stages, and genes up-regulated during T cell lineage commitment and maturation (*Ikzf3, Id3, Cd2, Cd4* and *Cd8* genes, among others). The second principal component (PC2, 26% of total variance) was associated with genes with peak or repressed expression in the transition from DN3 to DP cells (**Figure 2-4A)**. PC2 segregated immature (ETP) and mature (single positive) populations from those involved in the transitions around TCR re-arrangements, the top PC2-ranked gene being *Ptcra*, which encodes the pre-T cell antigen receptor alpha, along with the recombinase genes *Rag1/2*, among others (**Figure 2-4B,** right).

We next performed unsupervised hierarchical model-based clustering of thymic and M-ATO-derived populations. Due to differences in baseline gene expression, we normalized and

compared the pattern of gene expression within and between thymus and M-ATO-derived samples in several ways. To capture all the sources of variability contributing to the PCA map above, we first classified the genes by their overall expression profile, using an unsupervised approach and stringent thresholds. We then identified a set of most variable genes (2554 mouse genes) using pair-wise statistical tests within (e.g., THY-ETPs vs THY-DN2s), and between (THY_ETPs vs ATO-ETPs) each compartment. To better visualize gene expression trends, clusters were reordered to match peaked gene expression in the cluster with developmental stages (from ETPs to SPs) (**Figure 2-4C**). Hierarchical model-based clustering and heatmap visualization revealed that our approach captured a rich mosaic of expression profiles. As with the PCA, THY and M-ATO expression profiles were highly correlated overall, and largely mimicked the profiles of reference populations from Immgen.

Model-based clustering was also performed on the combined dataset (THY+ATO) so that both compartments have the same weight on the obtained groups. We identified a total of 29 gene clusters (**Table S2-1**), with distinct expression profiles. The average normalized expression profile for all genes in select clusters are displayed, and representative genes in each cluster are listed (**Figure 2-4D**). Individual gene expression levels within each cluster are provided in **Table S2-1**. Our unsupervised classification recapitulated the expected behavior of genes with known functions in thymic T-cell differentiation, both in THY and M-ATO-derived subsets.

Finally, Gene Set Enrichment Analyses (GSEA) for selected transcriptional transitions revealed that the set of most regulated genes between developmentally proximal populations in THY and M-ATO samples were largely similar (**Figure S2-4**), both showing significant enrichment scores when compared against independent thymocyte gene signatures.

Rag1 deficiency and notch signaling patterns are recapitulated in M-ATOs

As the M-ATO system closely mirrors phenotypic and transcriptional T cell development in the primary thymus, we next assessed two signaling pathways that are critical for thymopoiesis.

First, we used a *Rag1* (Recombination Activating Gene 1) deficient (*Rag1*$^{-/-}$) mouse to test whether TCR-dependent developmental checkpoints still applied within the M-ATO system. In M-ATOs generated from *Rag1*-/- marrow LSK cells, DP cells were absent, matching the phenotype of the *Rag1*-/- thymus (**Figure 2-5Ai and 5Aii**) (104). Both the M-ATO and thymus from *Rag1*-/- mice showed normal progression through the DN1/DN2 to the DN3 stage but a block in transition from DN3 to DN4 (**Figure 2-5Bi and 5Bii**). A small population of ISP8 cells (Immature Single Positive CD8 cells: CD3^{-} CD4^{-} CD8^{+}) was also detected in both M-ATO and thymus from *Rag1*-/- mice. Although a DP population emerged later in culture (data not shown), CD3 and TCRβ were never expressed over the course of the culture, again consistent with *Rag1*-/- thymocytes (**Figure 2-5Ci and 5Cii**).

To determine whether Notch signaling during T cell development in the M-ATO resembles that of the endogenous thymus, we used LSK cells from a Transgenic Notch Reporter (TNR) mouse line (105). In both endogenous thymocytes and M-ATO cells, Notch reporter activity fell from the DN2b to the DN3a stage, and again during the DN3a to DN3b transition (**Figure 2-5D and 5E**); the latter marks the stage during which thymocytes undergo beta-selection and when RNA expression of Notch targets is markedly decreased (63, 73, 82). Thus, the M-ATO system was able to recapitulate changes in Notch reporter activity in highly defined stages of T cell development.

The kinetics of T cell differentiation are captured by initiation of M-ATOs with different progenitor populations.

We next interrogated if the M-ATO system was able to recapitulate T cell development when seeded with different phenotypic progenitors in the hematopoietic hierarchy. From C57BL/6 bone marrow, the following phenotypes were tested in M-ATOs; HSC (LSK IL7R$^-$ CD150$^+$ CD48$^-$), MPP: Multi-Potent Progenitors (LSK IL7R$^-$ CD150$^-$ CD48$^-$), LMPP: Lymphoid-primed Multi-Potent Progenitors (LSK IL7R$^+$ Flk2$^+$), and CLP: Common Lymphoid Progenitors (Lin$^-$ c-Kit^{Lo} Sca^{Lo} IL7R$^+$ Flk2$^+$). In addition, the following populations were isolated from thymus and tested in M-ATOs: ETP: Early thymic progenitors (Lin$^-$ c-Kit^{Hi} CD44^{Hi} CD25$^-$), DN2 (Lin$^-$ CD4$^-$CD8$^-$ c-Kit^{Hi} CD44^{Hi} CD25$^+$), and DN3 (Lin$^-$ CD4$^-$ CD8$^-$ c-Kit$^-$ CD44$^-$ CD25$^+$). Analyses at weeks 1, 2 and 6 were performed to assess the kinetics of T-cell development (**Figure 2-6 A-D**). At week 1, only M-ATOs initiated with the most T-committed population tested (thymic DN3) had reached the ISP8 and DP stages, while the M-ATO-derived cells initiated from all the other more immature subsets remained at the DN stage (**Figure 2-6A and 6D)**. However closer analysis of the DN subsets at week 1 showed only HSC-initiated M-ATOs remained at the DN1 stage, MPP had generated a mix of DN1-3, LMPP, CLP and ETP had generated a mix of DN2 and DN3;only DN3 subsets remained in the M-ATOs initiated from DN2 and DN3 populations (**Figure 2-6A and Figure S2-5A**). By week 2 of culture, HSC and MPP-seeded M-ATOs were still almost entirely at the DN stage, whereas M-ATOs initiated from all the lymphoid progenitors (LMPP, CLP and all thymic progenitors) had begun to produce DP cells and CD3$^+$ TCRβ$^+$ cells (**Figure 2-6B and 6D**). Within the DN cells that remained in cultures, a logical further progression through the subsequent stages was seen from each type of initiating cell (**Figure S2-5B**). By week 6 all hematopoietic subsets tested in M-ATOs had produced mature T cells (**Figure 2-6C and 6D**). A

detailed time course analysis of T cell differentiation from HSCs is shown in **Figure S2-5C and S2-5D.**

Interestingly, M-ATOs initiated with the most immature stem and progenitor cells (specifically HSC, MPP and LMPP) generated a higher frequency of CD4SP cells (**Figure 2-6C, Figure S2-5E**). CDSP4 output was barely detectable when initiating M-ATOs with CLPs and later populations.

The M-ATO system supports thymopoiesis from isolated single cells.

The efficiency of T cell differentiation in M-ATOs was next tested using limiting numbers of marrow LSK cells to initiate cultures with a fixed number of MS5-mDLL4 per M-ATO. The cell number and phenotype generated from each M-ATO was similar over a range of 4,000 to as few as 5 initiating LSK cells (**Figure 2-7A**). The observation that hematopoietic cells undergo a comparable amount of proliferation regardless of the initiating number of cells in the ATO was consistent throughout extensive studies. We therefore speculate that there are constraints related to the physical size of ATOs, possibly due to gas exchange and nutrient availability.

We next tested the feasibility of generating M-ATOs seeded with single FACS-isolated LSK cells. Of 48 M-ATOs plated, 7 produced sufficient cells for analysis by week 3 (**Figure 2-7B**). All 7 of the M-ATOs analyzed revealed a phenotype consistent with T cell commitment (negative for other lineage markers and exhibiting the phenotype of DN populations). Clones showed variations in terms of cell number and stage of differentiation, reflecting the heterogeneity of the LSK HSC/progenitor population. As expected, higher cell numbers were observed in those clones that had already progressed to the DP stage at time of analysis (**Figure 2-7B**).

The ability of M-ATOs to support clonal T cell development from highly purified HSC was then tested by seeding single cells from the $CD150^{+}CD48^{-}$ phenotypic subset of the LSK population into each M-ATO. At week 3 the cloning efficiency was at least 12% (6 clones out of 48 M-ATOs could be analyzed) (**Figure 2-7C**); at this early time point, none of the M-ATOs had progressed past the DN stage (**Figure 2-7C, Figure S2-6A**). Interestingly however, the 3 week clones were not fully synchronized with some still mostly at the DN1 stage and others already exclusively at the DN3 stage (**Figure 2-7C and Figure S2-6A**), suggesting that the cells within the HSC phenotype were at slightly different states of T lymphoid priming when isolated (Rothenberg, 2011). At week 6-7, depending on the technical efficiency of the single cell seeding, 25% to 49% of the M-ATOs showed cell growth, and all clones analyzed revealed T cell commitment, most of them containing DP and $TCR\beta^{+}CD3^{+}$ CD4SP and CD8SP (**Figure 2-7D and Figure S2-6B-C**). Cell output in single HSC-seeded M-ATOs ranged from $2x10^{6}$ to $10x10^{6}$ by week 6 to 7 **(Figure 2-7D and Figure S2-6C)**. Intracellular detection of the Treg-associated transcription factor FOXP3 revealed that 4 out of 6 analyzed M-ATOs seeded with a single HSC produced $CD4^{+}CD25^{+}Foxp3^{+}$ Treg-like cells (**Figure 2-7E)**. Analysis of TCR diversity via Vβ expression by flow cytometry on 12 independent M-ATOs, each generated from a single HSC revealed that both the CD8SP and CD4SP produced in M-ATOs exhibited a broad repertoire with a similar pattern of Vβ usage seen across M-ATO clones (**Figure 2-7F**) and in bulk cultures and normal thymus of the same C57BL/6 strain (**Figure 2-3B**).

Discussion

We have shown here a simple and powerful *in vitro* model of murine T cell differentiation that faithfully recapitulates the exquisitely controlled progression of key

phenotypic and transcriptional events that define normal thymopoiesis. The quantitative and temporal consistency of the M-ATO system provides an experimental and quantitative platform that can be used to test how extrinsic and intrinsic factors affect the process of T cell commitment and maturation. The M-ATO system allows the rigorous interrogation of T cell potential in highly purified HSC and progenitor populations, including LMPP and CLP from the marrow, and multipotent and T cell committed progenitors in the thymus. Impressively, M-ATOs seeded with single HSCs were able to generate a diverse array of mature thymocytes including polyclonal CD4SP and CD8SP, TCRβ cells and $FOXP3^{+}CD4^{+}CD25^{+}$ cells.

Despite the remarkable fidelity in the transcriptional profiling of populations from normal thymus and M-ATOs, a few subtle differences were noted. $TCR\beta^{+}CD3^{+}$ DP cells from M-ATOs partially overlapped transcriptionally with the more immature $TCR\beta^{-}CD3^{-}$ DP population from endogenous thymus, possibly due to earlier surface expression of TCRβ/CD3 on DP cells in the M-ATO. Also, basal expression of genes known to be transcriptional targets of Notch signaling was higher in M-ATO populations. Nonetheless, the overall transcriptional profile of Notch targets during T cell development was conserved, and using the TNR mouse model in the ATO closely mirrored the pattern of Notch signaling during T cell development seen *in vivo*.

Based on an *in vivo* thymic implant model, cellular turnover for the replacement of thymocytes in the mouse thymus has been estimated to take 4 weeks (106). The kinetics of T cell development was similar in the M-ATOs, with the generation from HSC of all stages of thymocytes including single positive cells by week 4. The more immature the initiating population, the slower the onset of T cell development, with at least 2 extra weeks in lag time seen with highly purified HSC compared with the more lymphoid committed progenitors LMPP and CLP.

Unlike the endogenous thymus (107-109), the M-ATOs are not constantly seeded with bone marrow progenitors; however, T cell production can be maintained in M-ATOs for several weeks. Thymus transplantation experiments have also shown that thymocytes are able to maintain T cell production without the input of bone marrow progenitors for several weeks, a process called thymus autonomy (110-112). However, although thymus autonomy has been associated with the development of T-ALL (113, 114) in mice, M-ATO-derived thymocytes maintained a highly diverse TCR Vβ repertoire without evidence of clonal outgrowth for at least 10 weeks of analysis.

The analysis of the TCR Vβ repertoire in M-ATO-derived thymocytes showed that some clones naturally eliminated in the thymus were present in M-ATOs, strongly suggesting that negative selection does not occur in the organoid system. This finding is consistent with the absence of thymic epithelial cells in ATOs. Although rare dendritic cells are detected in M-ATO cultures, their presence does not appear to be sufficient to induce negative selection. The detection of $GFP^{+}CD4^{+}CD25^{+}$ cells in M-ATOs generated from FOXP3-reporter mice is phenotypic evidence that Tregs are produced in M-ATOs, but definitive conclusions will require functional studies of these cells.

In the absence of thymic epithelium, positive selection of CD8SP cells is presumed to occur through MHC class I ligands ubiquitously presented by the stromal cells and the hematopoietic cells generated in the cultures. Monolayer murine co-cultures have not permitted the production of CD4SP cells, possibly because of a lack of Class II expression or inefficiency of TCR-MHC interactions in these systems. The murine ATO system however clearly does generate CD4SP cells. Similar to human HSPC-derived ATOs (47), M-ATOs contain a population of hematopoietic cells that express MHC-class II, though at a lower frequency than in the normal thymic microenvironment. It is interesting to note that M-ATOs seeded with hematopoietic populations

with broad lineage (including myeloid) potential (HSC, MPP and LMPP) readily generated CD4SP cells, whereas those initiated from progenitors with more restricted, lymphoid only potential (CLP and thymic progenitors) did not, supporting the idea that it is the presence of non-lymphoid lineages that provide the required Class II presentation. It is also possible that the 3-D structure of the ATO model provides more optimal interactions between MHC-class II expressing cells and T cell precursors than do monolayer systems; of note other 3D systems (fetal thymic organ cultures and reaggregated primary stromal organoids) also allow positive selection and T cell maturation (44, 115-117). In addition, 3D structures may allow easier migration of maturing T cells away from Notch ligand-expressing stromal cells, a process that is seen during migration through the normal cortical-medullary thymic architecture. The M-ATO system offers a simple, reproducible, and modular platform to further explore the specific mechanisms of positive selection and the many other fundamental processes that drive T cell development.

Acknowledgements

We gratefully acknowledge the expert technical assistance of Felicia Codrea, Jessica Scholes, and Jeffrey Calimlim from the UCLA Broad Stem Cell Research Center (BSCRC) Flow Cytometry Core; as well as the Technology Center for Genomics and Bioinformatics (TCGB) at UCLA and the Translational Pathology Core Laboratory (TPCL) at UCLA. We thank L. Coulombel for generously providing us with MS-5 cells many years ago. This work was supported by the National Institute of Health (NIH Bethesda, MD) grants RO1AG049753 (GMC), R21AI119927 (GMC), 5P30AG028748/UL1TR000124 (NCATS/UCLA CTSI) (D.C), P30CA016042 (NCI) (TCGB and TPCL cores), KL2TR001882 (NIH/NCATS/UCLA CTSI) (CSS), K08CA235525 (NIH/NCI) (CSS), NIH T32GM008042 (V.S) and the Connie Frank and

Evan Thompson Program for Collaborative Restorative Transplantation Research. VS acknowledges the support of the Eli and Edythe Broad Center of Regenerative Medicine and Stem Cell Research at UCLA Training Program.

Author contributions

Conceptualization, A.M.-H., V.S., C.S.S., and G.M.C.; Methodology, A.M.-H., and V.S.; Formal analysis, D.C.; Investigation, A.M.-H., V.S., S.T., A. Z., N.J., S. L., S.L., Y. Z., B.C. C. H.; Data Curation, D.C.; Writing – Original Draft, A.M.-H., V.S., and G.M.C.; Writing – Review and Editing, A.M.-H., V.S., C.S.S., S.C.D., and G.M.C.; Supervision, G.M.C.; Funding acquisition, G.M.C.

Declaration of interests

A.M.-H., C.S.S., and G.M.C. are listed on patent/s relating to this work. A.M.-H., C.S.S., and G.M.C. are co-founders of PLUTO Immunotherapeutics Inc. and act as consultants for the company.

Figures

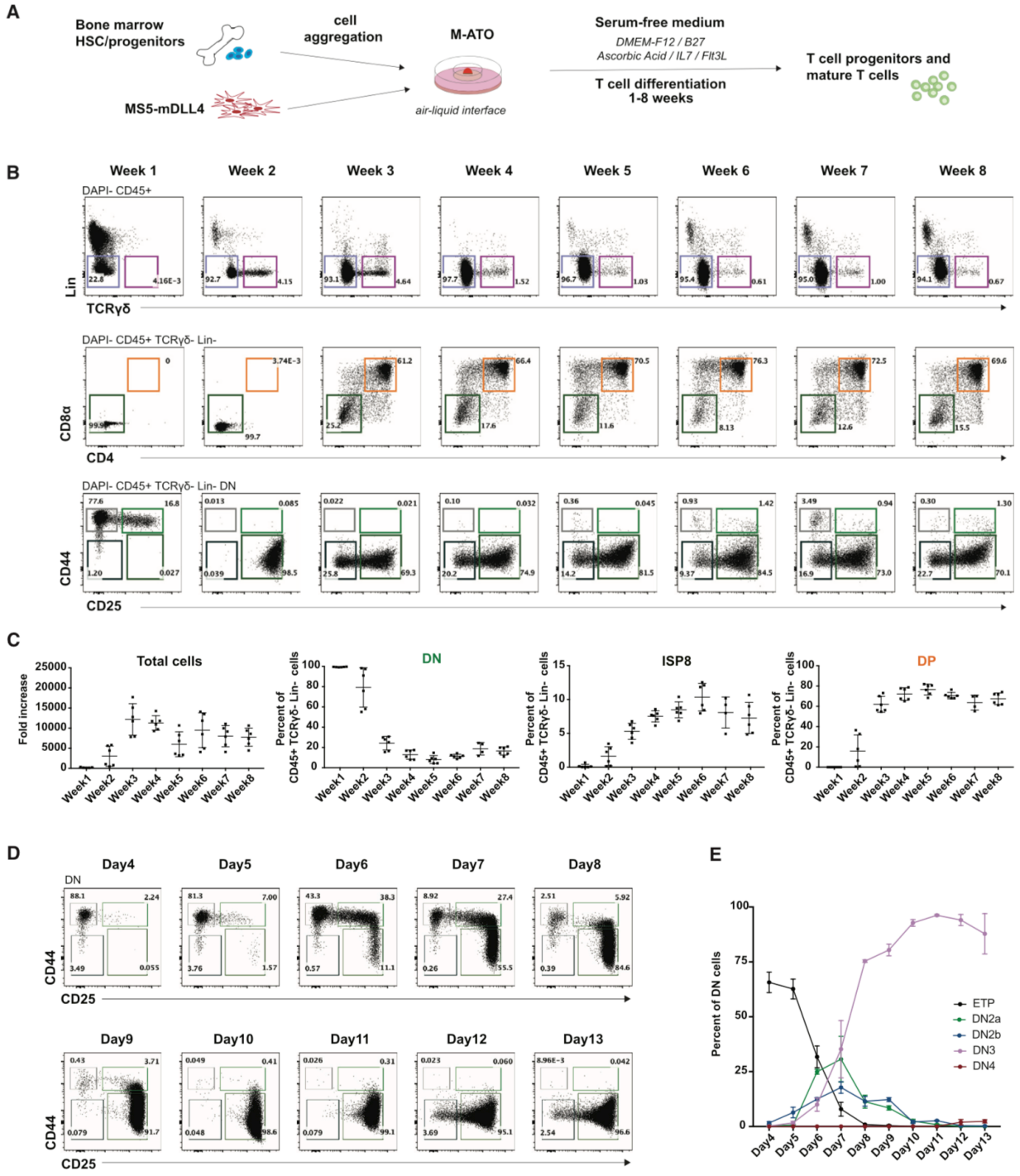

Figure 2-1. Kinetics of Early T Cell Differentiation in Murine ATOs

(**A**) Schematic of the M-ATO system.

(**B**) Representative kinetic analysis of T cell differentiation from bone marrow lineage-negative, $Sca1^+$, $cKit^+$ (LSK) isolated from C57BL/6 wild-type (WT) mice at the indicated time points, gated on $CD45^+$ cells to exclude non-hematopoietic cells. Middle and bottom rows: cells are gated on CD11b, CD11c, Gr1, CD19, B220, and NK1.1 (Lin neg) and TCRgd cells. Bottom row: cells are further gated on double-negative (DN) cells CD8CD4 to analyze DN subsets: DN1 ($CD44^+CD25$), DN2 ($CD44^+CD25^+$), DN3 ($CD44CD25^+$), and DN4 (CD44CD25) (Figure S1C).

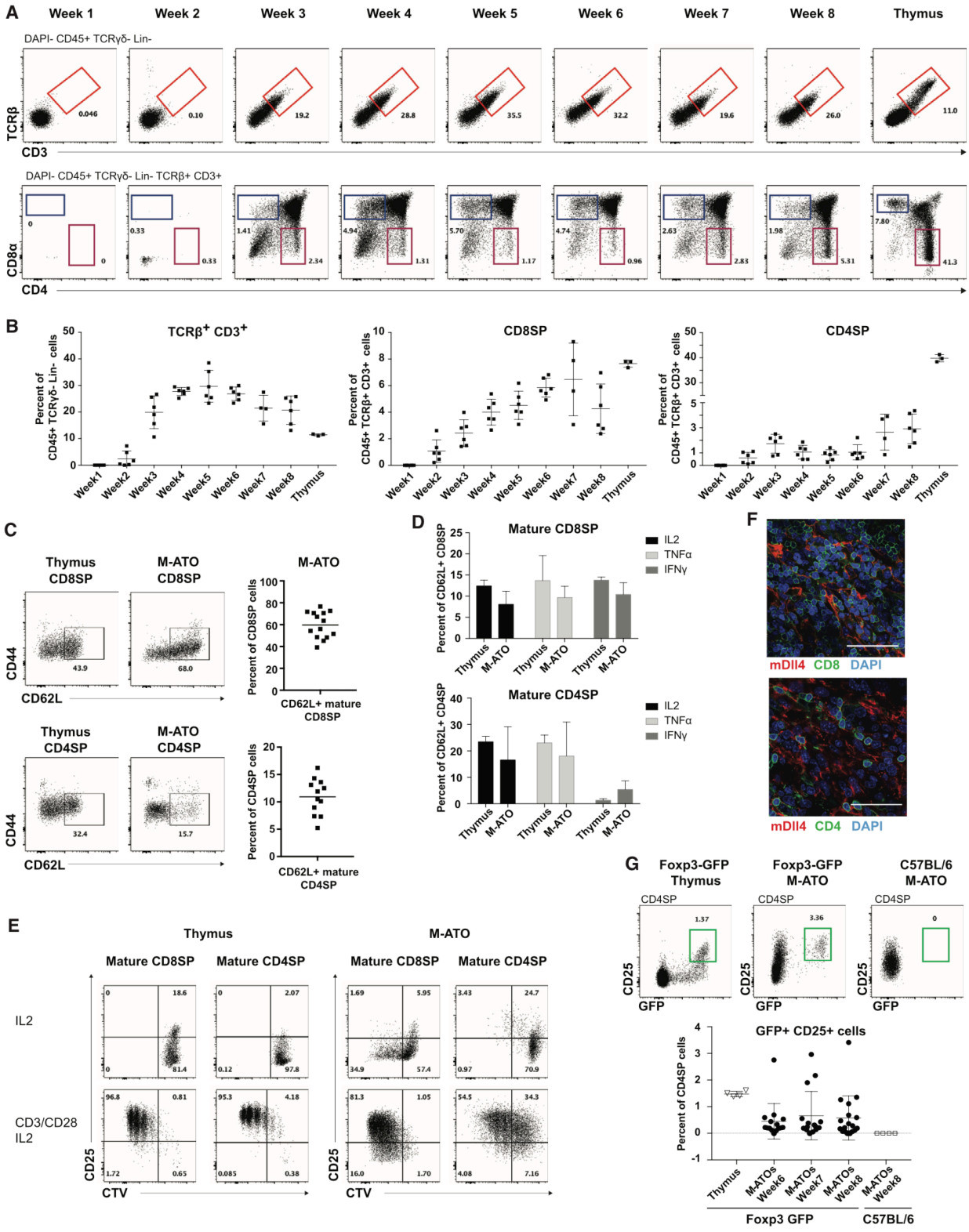

Figure 2-2. Murine ATOs Generate Functional CD8SP and CD4SP Mature T Cells and Foxp3^{+} CD4^{+} Treg-like Cells

(**A**) Representative kinetic analysis of T cell maturation from LSK cells isolated from C57BL/6 WT mice at the indicated time points gated on $CD45^+$ TCRgd Lin. CD4 and CD8 mature single-positive cells (CD4SP and CD8SP respectively) are gated on $TCRb^+$ $CD3^+$ cells (bottom row).

(**B**) Frequencies of $TCRb^+$ $CD3^+$ cells (left) are shown as percentage of total $CD45^+$ TCRgd Lin cells; CD8SP cells ($CD8^+$ CD4 $CD3^+$ $TCRb^+$) (middle) and CD4SP cells (CD8 $CD4^+$ $CD3^+$ $TCRb^+$) (right) are shown as percentage of $CD45^+$ $TCRb^+$ $CD3^+$ cells in M-ATOs and in the thymus. Error bar denotes ±SD (M-ATO, n = 6 independent experiments; thymus, n = 3).

(**C**) Expression of the maturation marker CD62L on CD8SP and CD4SP cells in week 7 M-ATOs. Summary of data on CD62L expression shown as percentage of CD8SP and CD4SP (n = 12 independent M-ATOs).

(**D**) Polyfunctional cytokine production by thymic or M-ATO-derived $CD62L^+$ CD8SP (top) and $CD62L^+$ CD4SP (bottom) after treatment with PMA + ionomycin for 6 h. Error bar denotes ± SEM (thymus SP8 and SP4, n = 2; M-ATO SP8, n = 5; M-ATO SP4, n = 2).

(**E**) Proliferation (as measured by dilution of CellTrace Violet (CTV) and activation (upregulation of CD25) of thymic (left) and M-ATO-derived (right) $CD62L^+$ CD8SP and $CD62L^+$ CD4SP after 3 days of treatment with IL2 ± anti-CD3/CD28 stimulation. Data are representative of three independent experiments.

(**F**) Representative immunofluorescence analysis (n = 3) for CD8 (green) and mDLL4 (red) expression (upper) and CD4 (green) and mDLL4 (red) (lower) in week 4 M- ATOs. Nuclei were stained with DAPI. Scale bars, 50 mm.

(G) GFP expression in CD4SP cells from thymocytes harvested from the Foxp3-GFP reporter mouse (left), generated in week 7 M-ATOs from LSK cells isolated from Foxp3-GFP (middle) or C57BL/6 WT mice (right). Frequencies of $Foxp3^+$ $CD25^+$ Treg-like T cells are shown as

percentage of total CD4SP T cells in thymus (n = 4) or in M-ATOs over time (n = 15 independent M-ATOs).

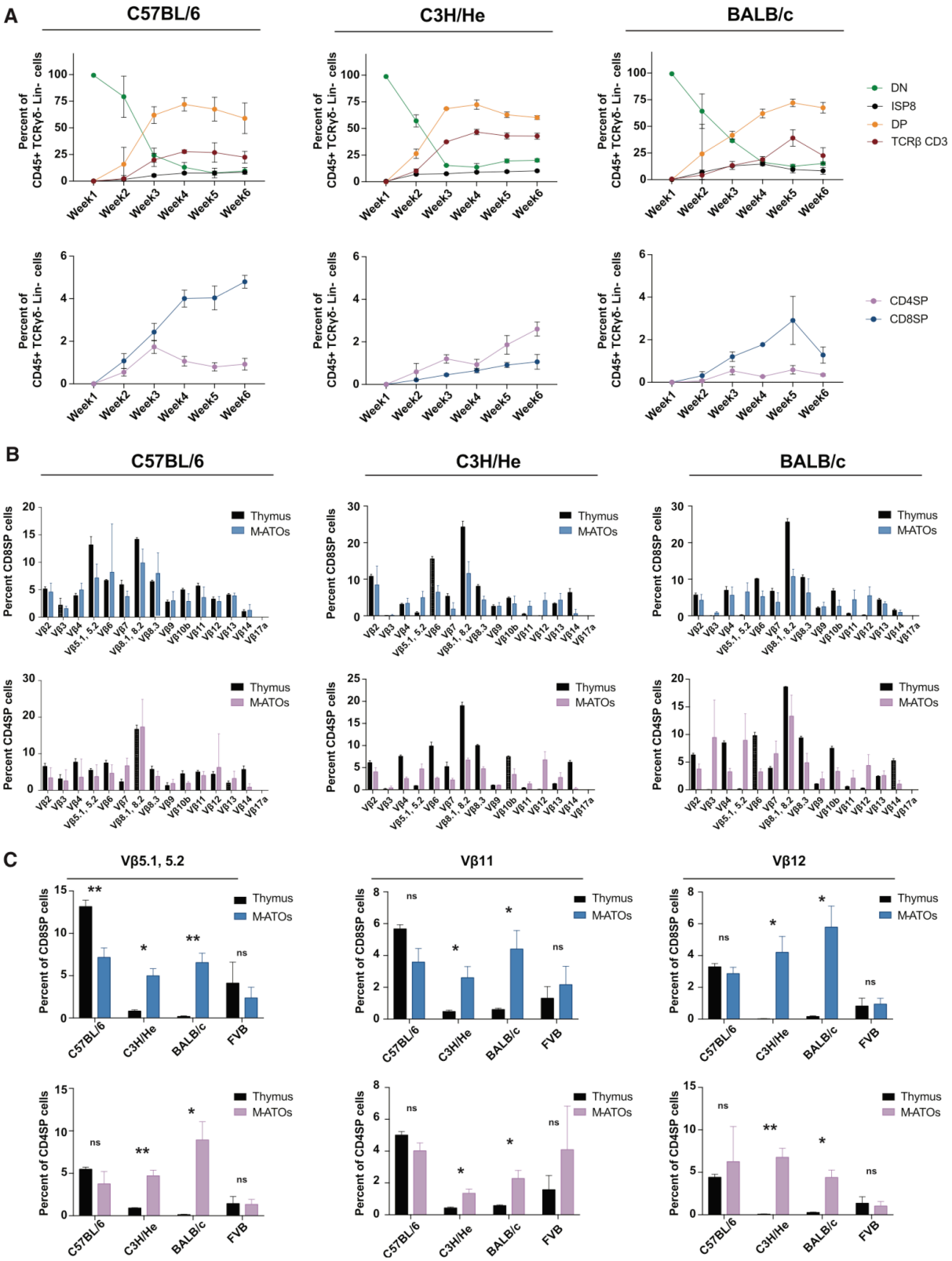

Figure 2-3. T Cell Differentiation and Maturation in M-ATOs from Different Murine Genetic Strains

(**A**) Frequencies of the different T cell populations generated in M-ATOs from LSK from the C57BL/6, C3H/He, and BALB/c backgrounds shown as percentage of total $CD45^+$ TCRgd Lin cells over time. Error bars denote ±SD (C57BL/6, n = 6; C3H/He, n = 3; BALB/c, n = 3 independent experiments).

(**B** and **C**) TCR Vb expression in T cells from thymus and M-ATOs from different murine genetic strains.

(**B**) TCR diversity in $CD3^+$ CD8SP (top) and $CD3^+$ CD4SP (bottom) T cells from week 6 M-ATOs or murine thymi, as shown by flow cytometry analysis of the frequency of TCR Vb family expression in 3 murine backgrounds.

(**C**) Comparison of the Vb5.1,5.2, Vb11, and Vb12 Vb TCR segments expression in $CD3^+$ CD8SP (top) and $CD3^+$ CD4SP (bottom) T cells by flow cytometry in the thymus versus M-ATOs in four murine backgrounds. Error bar denotes ± SD (C57BL/6 thymus, n = 4; C57BL/6 M-ATO, n = 5; C3H/He thymus, n = 4; C3H/He M-ATO, n = 4; BALB/c thymus, n = 4; BALB/c M-ATO, n = 5; FVB thymus, n = 4; FVB M-ATOs, n = 4 independent experiments). Significance: *$p < 0.05$, **$p < 0.01$, and ***$p < 0.001$ (multiple t tests).

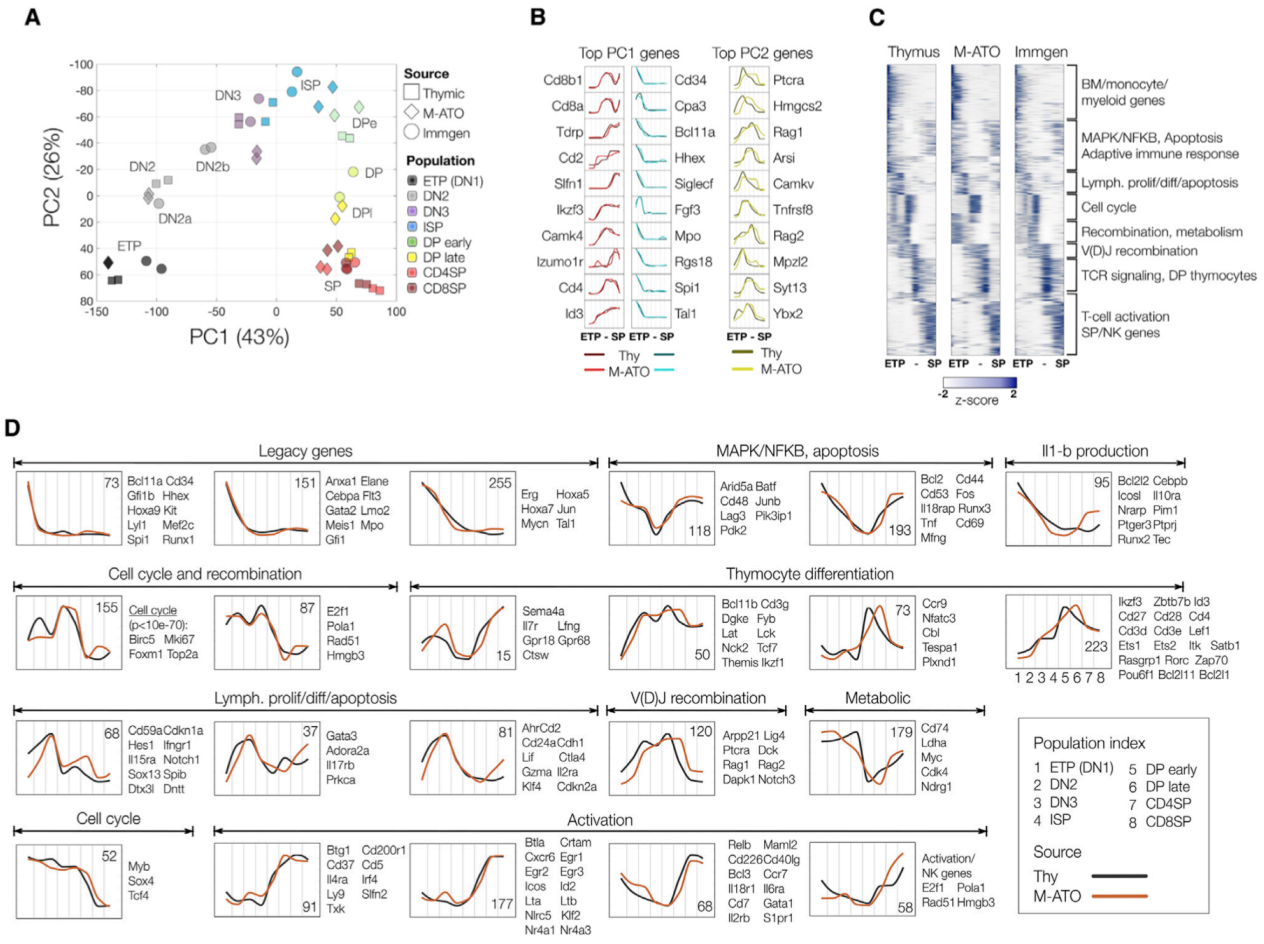

Figure 2-4. Transcriptional Regulation in M-ATO-Derived Thymocytes Recapitulates T Cell Developmental Programs In Vivo

(**A**) Principal-component analysis (PCA) of gene expression for M-ATO-derived and thymic populations. The first two components (PC1 and PC2) are shown along with the percentage of gene expression variance explained. Clustering was obtained with data from all detected genes without additional filters, using two in- dependent replicates for samples generated in this work. Data from equivalent populations profiled by the Immgen consortium was mapped to the same PCA axes as an independent control. Phenotypes for all populations and sources shown are provided in **Table S2-1**. (Immgen data contained total DP rather than distinguishing early versus late.)

(**B**) Gene expression profile in M-ATO-derived and thymic populations for genes with high PCA loadings. For each gene and source, the y axis represents the average gene expression profile (two replicates per population) normalized to the mean expression across all populations. The x axis represents samples sorted as in (A), from progenitor (ETP) to mature single-positive (SP) T cells. Left: genes with the highest loadings on PC1. The top ten genes with increasing or decreasing gene expression are shown. Right: top ten genes with the highest loading on PC2.
(**C**) Hierarchical model-based clustering of 2,554 highly variable genes classified as differentially expressed (Wald-adjusted p value < 0.01, fold change > 4) within and between thymic and M-ATO-derived populations. The x axis represents samples sorted as in (A), and data for two biological replicates per sample are shown. Clustering was performed using raw count data, and each individual heatmap represents variance-stabilized gene expression data normalized as *Z*-scores. Annotations correspond to representative functional categories for genes in each major cluster.
(**D**) Hierarchical selected gene clusters and representative genes obtained from model-based analysis of highly variable genes. For each cluster, the average normalized profile in M-ATO-derived and thymic populations for all genes in the cluster is shown. The number of genes classified in each cluster is displayed in the inset. Clusters are grouped by overall gene expression trends and functional annotations. Representative genes in each cluster are highlighted; the full classification is provided in **Table S2-1**.

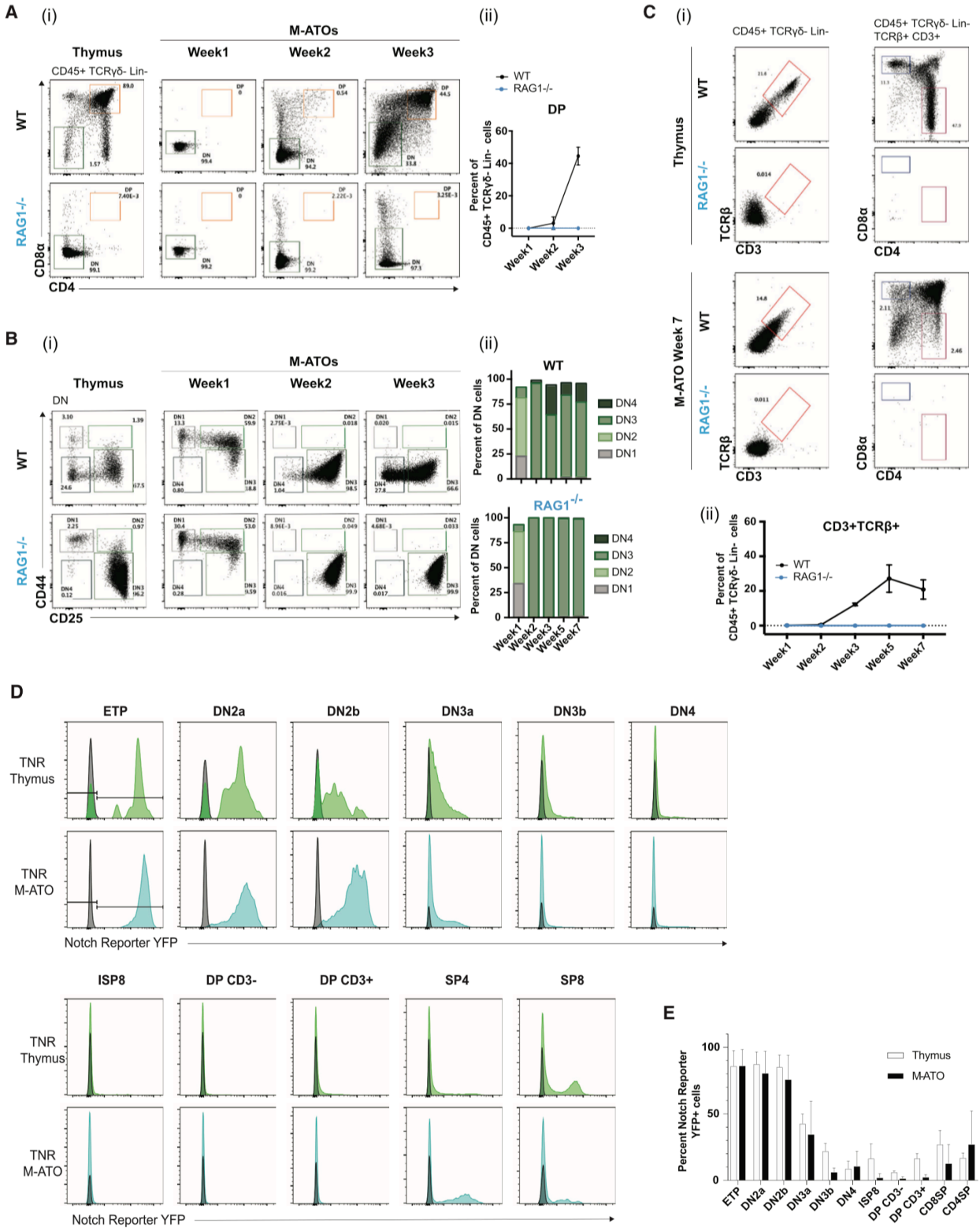

Figure 2-5. T Cell Differentiation in M-ATOs from Knockout and Reporter Murine Models Mimics the In Vivo Thymocyte Phenotype

(**A–C**) T cell differentiation in M-ATOs from LSK harvested from Rag1$^{/}$ and WT mice. Thymus phenotype is shown as comparison.

(**A**) (**i**) Representative kinetic analysis of DN and DP populations in M-ATOs. (ii) Frequency of DP population is shown as percentage of CD45^{+} TCRgd Lin cells. (B) (i) Representative kinetic analysis of DN development in M-ATOs. (ii) Frequency of DN1–DN4 populations are shown as percentage of total DN cells.

(**C**) (**i**) TCR and CD3 expression in M-ATOs. (ii) Frequency of TCRb^{+}CD3^{+} population is shown as percentage of CD45^{+} TCRgd Lin cells. Significance: (i) Data are representative of three biological replicates. (ii) Error bars denote ± SD (n = 3 independent experiments). (**D** and **E**) Notch activity in mouse thymus and M-ATO thymocyte populations using the transgenic Notch reporter (TNR) mouse model.

(**D**) Representative analysis of Notch reporter YFP expression levels in populations from the mouse thymus (top row, green) and M-ATO (bottom row, blue), shown in comparison with a negative control (gray).

(**E**) Frequency of TNR YFP^{+} cells in each thymocyte population from mouse thymus (white bars) and M-ATO (black bars). Error bars denote ± SD (n = 6 independent experiments).

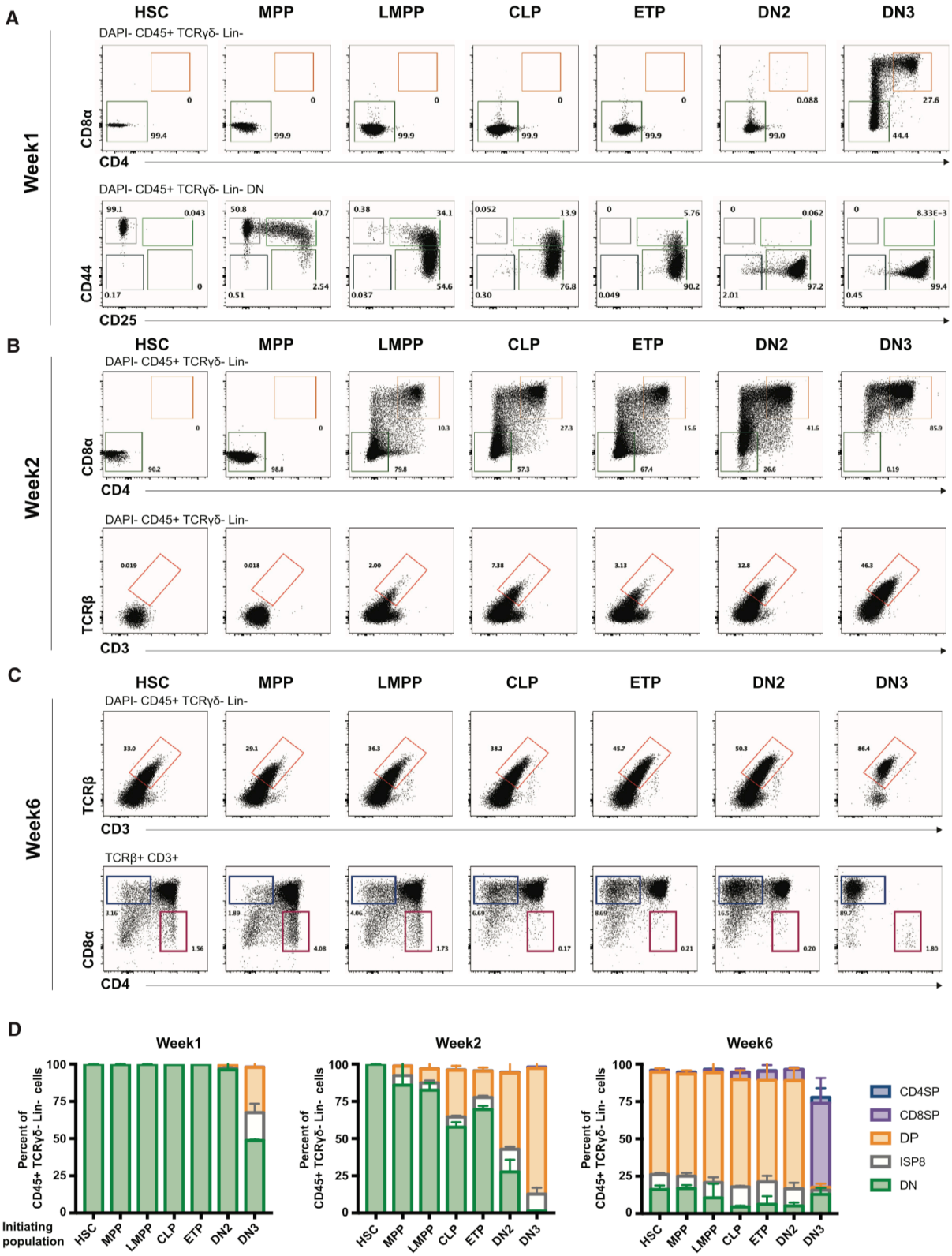

Figure 2-6. M-ATOs Recapitulate T Cell Differentiation from Different Hematopoietic Subsets

(A–C) Different subsets in the hematopoietic hierarchy from HSCs to T cell progenitors were isolated from the bone marrow and the thymus of C57BL/6 WT mice and seeded into M-ATOs. From the bone marrow: HSC (hematopoietic stem cell) (LinSca1^{+}cKit^{+}CD48CD150^{+}IL7R); MPP (multi-potent progenitor) (LinSca1^{+}c-Kit^{+}CD48CD150IL7R); LMPP (lymphoid-primed multi-potent progenitor) (LinSca1^{+}c-Kit^{+}IL7R^{+}Flk2^{+}); and CLP (common lymphoid progenitor) (LinSca1^{Lo}c-Kit^{Lo} IL7R^{+}Flk2^{+}). From the thymus: ETP (LinCD4CD8c-Kit^{hi} CD44^{hi}CD25); DN2 (Lin CD4 CD8 c-Kit^{hi} CD44^{hi} CD25^{+}); and DN3 (Lin CD4 CD8 CD44 CD25^{+}). Representative phenotypes of M-ATO-derived cells are shown at weeks 1 (A), 2 (B), and 6 (C). Data are representative of three biological replicates.

(D) Frequencies of T cell populations shown as percentage of total CD45^{+} TCRgd Lin cells initiated from the different hematopoietic subsets in week 1, week 2, and week 6 M-ATOs. Error bars denote ± SD (n = 3 independent experiments).

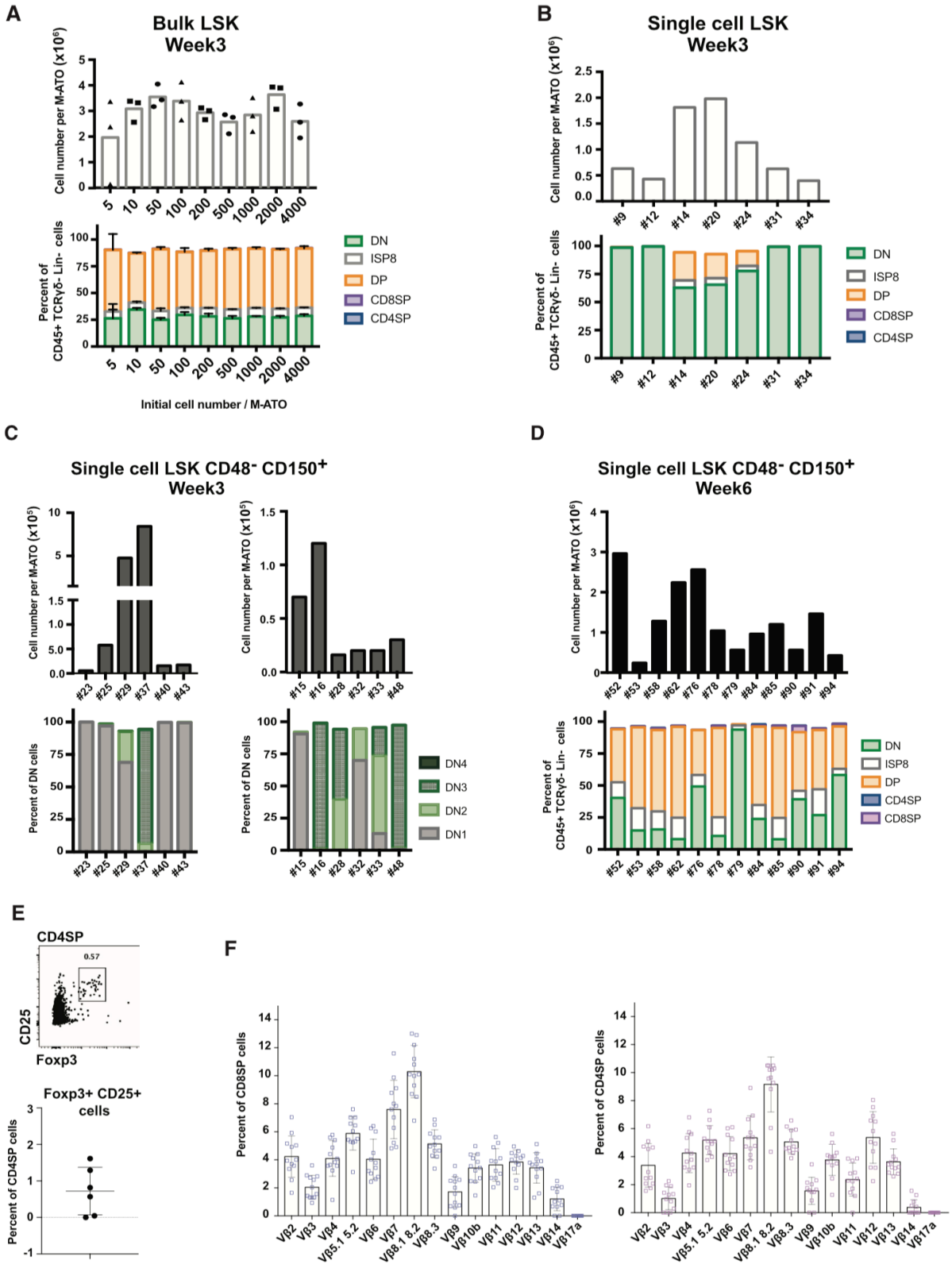

Figure 2-7. The M-ATO System Supports Full T Cell Differentiation from Isolated Single Cells

(**A**) Cell numbers and phenotype in week 3 M-ATOs initially seeded with different numbers of LSK isolated from C57BL/6 WT mice (5 to 4,000 cells per ATO). Top: total cell number per M-ATO. Bottom: frequency of cell populations as percentage of $CD45^+$ TCRgd Lin cells. Error bars denote ± SD (n = 3 independent experiments).

(**B**) Cell numbers (top) and phenotype (bottom) at week 3 in M-ATOs seeded with a single LSK cell from bone marrow. Seven independent M-ATOs are shown.

(**C** and **D**) Cell numbers (top) and phenotype (bottom) from weeks 3 (**C**) and 6 (**D**) M-ATOs initially seeded with a single (LSK $CD48CD150^+$) HSC cell from C57BL/6 WT mice. Twelve independent M-ATOs are shown from two independent experiments (left and right). (**C**) Frequencies of the DN1, DN2, DN3, and DN4 populations are shown as percentage of total DN cells, which represent 100% of the cells in week 3 M-ATOs. (**D**) Frequencies of the T cell populations are shown as percentage of total $CD45^+$ TCRgd Lin cells in week 6 M-ATOs.

(**E**) Expression of the transcription factor Foxp3 via intracellular staining on CD4SP cells from thymocytes harvested from week 9 M-ATOs initially seeded with a single (LSK CD48 $CD150^+$) HSC. Frequencies of $Foxp3^+CD25^+$ Treg-like T cells are shown as percentage of total CD4SP T cells. $Foxp3^+CD25^+$ Treg-like T cells are detectable in five of six independent experiments.

(**F**) TCR diversity in $CD3^+$ CD8SP (left) and $CD3^+$ CD4SP (right) T cells from 12 week 6–7 M-ATOs generated from a single (LSK $CD48CD150^+$) HSC as shown by flow cytometry analysis of the frequency of TCR Vb family expression. Error bar denotes ± SD (n = 12 independent experiments).

Chapter 3 – The Metabolic Landscape of Thymic T cell development *in vivo* and *in vitro*

Abstract

Although metabolic pathways have been shown to control differentiation and activation in peripheral T cells, metabolic studies on thymic T cell development are still lacking, especially in human tissue. In this study, we use transcriptomics and extracellular flux analyses to investigate the metabolic profiles of primary thymic and *in vitro*-derived mouse and human thymocytes. Core metabolic pathways, specifically glycolysis and oxidative phosphorylation, undergo dramatic changes between the double-negative (DN), double-positive (DP), and mature single-positive (SP) stages in murine and human thymus. Remarkably, despite the absence of the complex multicellular thymic microenvironment, *in vitro* murine and human T cell development recapitulated the coordinated decrease in glycolytic and oxidative phosphorylation activity between the DN and DP stages seen in primary thymus. Moreover, by inducing *in vitro* T cell differentiation from *Rag1*$^{-/-}$ mouse bone marrow, we show that reduced metabolic activity at the DP stage is independent of TCR rearrangement. Thus, our findings suggest that highly conserved metabolic transitions are critical for thymic T cell development.

Introduction

There is a rapidly growing body of evidence that metabolic changes have a key role in regulating the function, differentiation, and T cell receptor (TCR)-mediated activation of mature peripheral T cells (51, 58, 70, 118-121). However, far less is known about the role of metabolism during thymopoiesis, where profound shifts in transcription, cues from the thymic microenvironment, and TCR rearrangement and signaling all combine to direct the development of a diverse array of T cells from uncommitted progenitors (9, 122-124). Metabolic studies of

human thymopoiesis are particularly lacking due to the technical challenges of using primary human tissue for functional assays.

After seeding the thymus organ, hematopoietic stem and progenitor cells (HSPCs) progressively commit to a T cell fate. The earliest thymocyte stages are called “double negative” (DN), reflecting the absence of expression for both CD4 and CD8 surface markers. Murine thymocytes progressively committing to the T cell lineage are characterized as DN1, DN2, DN3, DN4; subsequent acquisition of CD8 expression leads to the immature single positive CD8 (ISP8) stage. In human thymus, early DN progenitors express CD34 and can be further defined as Thy1, Thy2, and Thy3; in contrast to murine thymopoiesis, the stage that follows these progenitors is marked by acquisition of CD4 (ISP4) (20-22). Committed thymocytes that successfully rearrange the T cell receptor beta subunit (TCRβ) co-express CD4 and CD8, becoming so-called “double positive” (DP). After DP cells proceed through positive selection, they generate single-positive CD8 (SP8) or CD4 (SP4) T cells.

Current understanding of thymocyte metabolism has been mostly shaped by transcriptional and genetic perturbation studies in murine thymus. The Immunological Genome Project Consortium (ImmGen) has described a global transcriptional shutdown of metabolic genes at the DP stage in murine thymocytes that was not a result of exit from the cell cycle, but instead associated with downregulation of ribosomal proteins, RNA translation, and *Myc* expression (63). Independent studies have shown that perturbation of genes involved in metabolic pathways, such as *Glut1*, *Raptor*, *Pkm2*, *Pparδ*, *Mpc1*, *Opa1*, and *Rpl22*, disrupt the DN to DP transition in murine thymocytes (61, 64-69). Metabolic transitions appear to be critical for proper T cell development yet have not been investigated in-depth in human thymopoiesis. In addition, most studies have primarily focused on the metabolism of either early thymocyte stages

or mature T cells in the thymus separately (62); a complete characterization of metabolic shifts from the DN-SP stages has not yet been performed in mouse or human primary thymus.

The thymopoiesis field has greatly benefited from *in vitro* models of T cell differentiation from HSPCs. One such model is the artificial thymic organoid (ATO), a serum-free system that generates mature T cells from various HSPC sources, such as mouse bone marrow (125), human cord blood (47), and induced human pluripotent stem cells (iPSCs) (48). Considering the challenges of studying metabolic changes during *in vivo* human thymocyte development, *in vitro* models such as the ATO are potentially more tractable to perform metabolic measurements and perturbations. However, studies have not yet probed how well *in vitro* models reflect *in vivo* thymocyte metabolic activity.

This report uses transcriptomics and extracellular flux analyses to metabolically profile human and murine thymocytes ranging from early DN to mature SP stages. We also compare the metabolic profiles of primary thymic populations to those of *in vitro* ATO-derived populations from the DN to DP stages. Our study thus uncovers fundamental metabolic patterns in T cell development that are conserved in human and murine thymus, as well as *in vitro* culture conditions.

Materials and Methods

Ethics statement

All bone marrow and thymus harvesting from mice were conducted according to the National Institutes of Health Guide for Care and Use of Experimental Animals under a protocol approved by the UCLA Chancellor's Animal Research Committee (ARC).

Cord blood and thymus samples were acquired through the UCLA Translational Pathology Core Laboratory (TPCL) and Children's Hospital Los Angeles, respectively. As all samples were considered waste tissue without patient identifiers, the Institutional Review Board (IRB) deemed this work as not human subject research.

Mice

All animal experiments were conducted under a protocol approved by the UCLA Chancellor's ARC. This study used 1-4 month-old mice from Jackson Laboratory (Bar Harbor, Maine): C57BL/6 (**Cat# JAX:000664**) mice and RAG1$^{-/-}$ mice **(JAX:002216)**). Mice from both sexes were randomly allocated to experimental groups.

Cell Lines

The generation of MS5-mDLL4 and MS5-hDLL4 cell lines in our lab has been previously described (48, 125).

Isolation of murine bone marrow HSPCs for M-ATO culture

Fresh or frozen bone marrow cells were enriched for HSPCs by negative cells selection of Lin- cells by magnetic cell sorting (MACS) using Murine Lin depletion Kit (**Miltenyi, Auburn CA, Cat# 130-110-470**). HSPCs were isolated by FACS sorting using following phenotype: LSK (Lin$^-$ Sca1$^+$ cKit$^+$; Lin$^-$ stands for: Ter119$^-$, TCRγδ$^-$, B220$^-$, CD19$^-$, CD11c$^-$, CD11b$^-$, Gr1$^-$, NK1.1$^-$, CD5$^-$, CD4$^-$, CD8$^-$, CD3$^-$). Sorted cells were immediately seeded into MS5-mDLL4 M-ATOs.

Murine artificial thymic organoid (M-ATO) cultures

M-ATOs were generated as previously described (125). MS5-mDLL4 cells were harvested by trypsinization and resuspended in serum free M-ATO culture medium ("D/F12-B27") composed of DMEM-F12 (**Gibco, Cat# 11320033**), 2% B27 supplement (**ThermoFisher Scientific, Grand Island, NY, Cat# 17504-044**), 30 μM L-ascorbic acid 2-phosphate sesquimagnesium salt hydrate (**Sigma-Aldrich, St. Louis, MO, Cat# A8960-5G**) reconstituted in 1X PBS, 1% penicillin/streptomycin (**Gemini Bio-Products, West Sacramento, CA, Cat# 400-109**), 1% Glutamax (**ThermoFisher Scientific, Grand Island, NY, Cat# 35050-061**), 5 ng/ml rmFLT3L (**Peprotech, Rocky Hill, NJ, Cat# 250-31L**), 5 ng/ml rmIL-7 (**Peprotech, Cat# 217-17**), 10 ng/ml rmSCF (Peprotech, **Cat# 250-03**) (of note SCF was added only for the first week of culture) and beta mercaptoethanol (BME) (0.05mM) (**Sigma-Aldrich, Cat# M7522**). D/F12-B27 was made fresh weekly. $1.5x10^5$ MS5-mDLL4 cells were combined with purified murine HSPCs (100-4000 cells / ATO). M-ATOs were plated on a 0.4 μm Millicell transwell insert (**EMD Millipore, Billerica, MA; Cat. PICM0RG50**) placed in a 6-well plate containing 1 ml D/F12-B27 per well. Medium was changed completely every 3-4 days by aspiration from around the cell insert followed by replacement with 1 ml with fresh D/F12 and cytokines.

Isolation of murine thymocytes and M-ATO-derived cells

Thymic fragments from the mouse thymus were finely dissected in FACS buffer (1X PBS/0.5% bovine serum album/2mM EDTA) and disrupted by pipetting to release thymocytes into suspension, followed by passage through a 70 μm nylon strainer. Cells were then stained for flow cytometry.

At the indicated times, M-ATO-derived T cells were harvested by adding FACS buffer (1X PBS/0.5% bovine serum album/2mM EDTA) to each cell insert and briefly disaggregating the M-

ATO by pipetting with a 1 ml "P1000" pipet, followed by passage through a 70 µm nylon strainer. Cells were then stained for flow cytometry.

For Seahorse Extracellular Flux Analyses, thymocytes from mouse thymus and M-ATO were enriched for DN, ISP8, and SP8 cells by negative selection of $CD4^-$ cells, whereas DP early and SP4 cells were enriched in the $CD4^+$ cell fraction, using magnetic cell sorting (MACS) with PE-CD4 (RM4-4) antibody and Anti-PE Microbeads Kit (**Miltenyi, Auburn CA, Cat: #130-048-801**).

Flow cytometry cell sorting of mouse thymic and M-ATO-derived T cell populations used surface phenotypes as detailed in **Table S3-1**.

Isolation of human $CD34^+CD3^-$ HSPCs

Neonatal umbilical cord blood was obtained from discarded cord and placental units from deliveries at UCLA. All tissue samples were obtained under UCLA Institutional Review Board (IRB)-approved protocols or exemptions. All samples were enriched for mononuclear cells by Ficoll-Paque (GE Healthcare Life Sciences, Pitssburgh, PA) gradient centrifugation followed by positive selection of $CD34^+$ cells by magnetic cell sorting (MACS) using the CD34 MicroBead Kit UltraPure (Miltenyi Biotec, Auburn, CA). After MACS, $CD34^+$-cell-enriched fractions were utilized immediately or cryopreserved. Prior to use, cryopreserved cells were thawed, and the residual T cells were depleted by FACS by sorting for $CD34^+CD3^-$ cells, which were immediately seeded into H-ATOs.

Human Cord Blood Artificial thymic organoid (H-ATO) cultures

Generation of H-ATO cells were performed as previously described (47, 48), with the exception of the recombinant human IL-7 concentration in culture medium. MS5-hDLL4 cells were harvested and resuspended in serum-free H-ATO culture medium ('RB27'), which was composed of RPMI 1640 (Corning, Manassas, VA), 4% B27 supplement (ThermoFisher Scientific, Grand Island, NY), 30 M l-ascorbic acid 2-phosphate sesquimagnesium salt hydrate (Sigma-Aldrich, St. Louis, MO) reconstituted in 1X PBS, 1% penicillin–streptomycin (Gemini Bio-Products, West Sacramento, CA), 1-2% Glutamax (ThermoFisher Scientific, Grand Island, NY), 5 ng/ml recombinant human FLT3 ligand (rhFLT3L) and 2.5-5 ng/ml recombinant human IL-7 (rhIL-7) (Peprotech, Rocky Hill, NJ). RB27 was made fresh weekly. 1.5 x 10^5 MS5-hDLL4 cells were combined with 1 x10^2 to 1 x10^5 purified $CD34^+CD3^-$ cells per H-ATO. For each H-ATO, a 0.4-m Millicell Transwell insert (EMD Millipore, Billerica, MA; Cat. PICM0RG50) was placed in a 6-well plate containing 1 ml RB27 per well. Medium was changed completely every 3–4 d by aspiration from around the cell insert followed by replacement with 1 ml fresh RB27 and cytokines. H-ATOs were cultured for up to 10 weeks.

Isolation of human thymocytes and H-ATO-derived cells

Postnatal human thymi were obtained under an IRB exemption as discarded waste from patients undergoing cardiac surgery at Children's Hospital Los Angeles (CHLA). Thymic fragments were finely dissected in RPMI medium (Cellgro) and disrupted by pipetting to release thymocytes into suspension, followed by passage through a 70-µm nylon strainer. Cells were analyzed fresh on the same or the following day.

At the indicated times, H-ATO cells were harvested by adding FACS buffer (0.5% BSA and 2 mM EDTA in 1X PBS) to each well and briefly disaggregating the H-ATO by pipetting with a 1 ml 'P1000' pipet tip, followed by passage through a 50-m nylon strainer.

For Seahorse Extracellular Flux Analyses, thymocytes from human thymus or human ATO were enriched for DN, ISP4, and SP4 cells by negative selection of $CD8^-$ cells, or enriched for DN and SP8 cells by negative selection of $CD4^-$ cells using magnetic cell sorting (MACS) with PE-CD8 (HIT8a) or PE-CD4 (OKT4) antibody respectively and Anti-PE Microbeads UltraPure Kit (**Miltenyi, Auburn CA, Cat: #130-105-639**).

Flow cytometry cell sorting of human thymic and H-ATO-derived T cell populations used the surface phenotypes as detailed in **Table S3-1**.

Flow cytometry

All flow cytometry stains were performed in 1X PBS/0.5% BSA/2 mM EDTA for 20 min on ice. TruStain FcX (**Biolegend, San Diego, CA, Cat#101320** for mouse, **Cat#422302** for human) was added to all murine samples for 5 min prior to antibody staining. DAPI (**Life technologies, Cat# D1306**) was added to all samples prior to analysis.

Analysis was performed on an LSRII Fortessa, and FACS sorting on FACSARIA or FACSARIA-H instruments (**BD Biosciences, San Jose, CA**) at the UCLA Broad Stem Cell Research Center Flow Cytometry Core.

For all analyses $DAPI^+$ cells were gated out, and single cells were gated based on FSC-H vs. FSC-W and SSC-H vs. SSC-W. Gating strategies were performed as detailed in **Table S3-1** and presented in previous reports (47, 125).

Anti-mouse and anti-human antibody clones used for surface and intracellular staining were obtained from **Biolegend (San Diego, CA)** or **BD Bioscience** (**San Jose, CA),** and are listed below. Flow cytometry data were analyzed with FlowJo software (**Tree Star Inc.**).

Flow cytometry antibody	**Clone**	**Source**	**Identifier**
Anti-mouse CD16/32 (TruStain FcX)	93	Biolegend	Cat# 101320, RRID:AB_1574975
Anti-mouse CD3	145-2C11	Biolegend	Cat# 100312, RRID:AB_312677
Anti-mouse CD4	RM4-5	Biolegend	Cat# 100550, RRID:AB_2562099
Anti-mouse CD4	RM4-4	Biolegend	Cat# 116006, RRID:AB_313691
Anti-mouse CD5	53-7.3	Biolegend	Cat# 100627, RRID:AB_2563930
Anti-mouse CD8a	53-6.7	Biolegend	Cat# 100708, RRID:AB_312747, Cat# 100706, RRID:AB_312745
Anti-mouse CD11b	M1/70	Biolegend	Cat# 101228, RRID:AB_893232
Anti-mouse CD11c	N418	Biolegend	Cat# 117328, RRID:AB_2129641
Anti-mouse CD19 (Clone 1D3/CD19)	1D3/CD19	Biolegend	Cat# 152406, RRID:AB_2629815
Anti-mouse CD25	PC61	Biolegend	Cat# 102016, RRID:AB_312865
Anti-mouse CD44	IM7	Biolegend	Cat# 103059, RRID:AB_2571953
Anti-mouse CD45R/B220	30-F11	Biolegend	Cat# 103116, RRID:AB_312981
Anti-mouse CD45R/B220	RA3-6B2	Biolegend	Cat# 103236, RRID:AB_893354
Anti-mouse Ly-6G/Ly-6C (Gr-1)	RB6-8C5	Biolegend	Cat# 108428, RRID:AB_893558
Anti-mouse NK1.1	PK136	Biolegend	Cat# 108728, RRID:AB_2132705
Anti-mouse TCRβ	H57-597	Biolegend	Cat# 109234, RRID:AB_2562350
Anti-mouse TCRγδ	GL3	Biolegend	Cat# 118120, RRID:AB_2562566, Cat# 118118, RRID:AB_10612756
Anti-mouse TER-119	Ter119	Biolegend	Cat# 116228, RRID:AB_893636
Anti-mouse CD62L	MEL-14	Biolegend	Cat# 104438, RRID:AB_2563058
Anti-mouse CD117 (c-KIT)	ACK2	Biolegend	Cat# 135122, RRID:AB_2562042
Anti-mouse Ly-6A/E (Sca-1)	D7	Biolegend	Cat# 108114, RRID:AB_493596
Human TruStain Fcx		Biolegend	Cat# 422302, RRID:AB_2818986
Anti-human CD3 Biolegend	UCHT1	Biolegend	Cat# 300426, RRID:AB_830755, Cat# 300472, RRID:AB_2687178
Anti-human CD1a	HI149	Biolegend	Cat# 300128, RRID:AB_2565566

Anti-human CD5 Biolegend	UCHT2	Biolegend	Cat# 300612, RRID: AB_314098, Cat# 300630, RRID:AB_2566473
Anti-human CD8a Biolegend	SK1	Biolegend	Cat# 344734, RRID: AB_2565243
Anti-human CD7	CD7-6B7	Biolegend	Cat# 343116, RRID:AB_2632912
Anti-human CD8a	RPA-T8	Biolegend	Cat# 301006, RRID:AB_314124
Anti-human CD8a	HIT8a	Biolegend	Cat #300908, RRID:AB_314112
Anti-human CD4	OKT4	Biolegend	Cat# 317410, RRID:AB_571955
Anti-human CD4 Biolegend (clone RPA-T4)	RPA-T4	Biolegend	Cat# 300556, RRID: AB_2564392
Anti-human CD34 Biolegend (clone 581)	581	Biolegend	Cat# 343506, RRID: AB_1731862, Cat# 343514, RRID:AB_1877168
Anti-human CD45 Biolegend (clone HI30)	HI30	Biolegend	Cat# 304036, RRID: AB_2563129
Anti-human CD45RA Biolegend (clone HI100)	HI100	Biolegend	Cat# 304122, RRID: AB_893357
Anti-human CD45RO Biolegend (clone UCHL1)	UCHL1	Biolegend	Cat# 304234, RRID: AB_2563819
Anti-human CD56 Biolegend (clone HCD56)	HCD56	Biolegend	Cat# 318318, RRID: AB_2561944
Anti-human CD14	M5E2	Biolegend	Cat# 301814, RRID:AB_389353
Anti-human CD19	HIB19	Biolegend	Cat# 302216, RRID:AB_314246
Anti-human TCRab Biolegend (clone IP26)	IP26	Biolegend	Cat# 306718, RRID: AB_10612569
Anti-human TCRgd Biolegend (clone B1)	B1	Biolegend	Cat# 331222, RRID: AB_2562317
Anti-mouse CD29 Biolegend (clone HMb1-1)	HMb1-1	Biolegend	Cat# 102222, RRID: AB_528790

Extracellular Flux Analysis

Thymocytes were centrifuged onto a XF96 well plate coated with Poly-D-Lysine and washed twice with DMEM assay medium containing 5 mM glucose, 2 mM L-glutamine, 1 mM sodium pyruvate, and 5mM HEPES. OCR and ECAR were measured under basal conditions and in response to 2 μM oligomycin, two injections of 0.75 μM fluoro-carbonyl cyanide phenylhydrazone (FCCP), and 2 μM Antimycin/Rotenone using the XF-96 Extracellular Flux

Analyzer (**Seahorse Bioscience**). Extracellular flux rates were normalized to cell number in each well using the Wave software (**Agilent**). Raw data were imported into R to calculate extracellular flux measurements: basal ECAR = baseline ECAR; basal OCR = baseline OCR – Rot/AA OCR; maximal OCR = maximum OCR – Rot/AA OCR; spare respiratory capacity = maximal OCR – basal OCR; OCR/ECAR ratio = basal OCR/basal ECAR) (57).

Data Availability Statement

RNA sequencing dataset is available from NIH's Sequence Read Archive (SRA) repository (PRJNA741323). A detailed description of data analysis and the software used can be found in method details. The raw data and R code supporting the conclusions of this article will be available by the authors upon request.

Quantification and statistical analysis

In all figures, *n* represents independent experiments and data are represented as mean ± standard deviation (s.d.). Statistical analysis was performed using R or GraphPad Prism software, *p*-values were calculated from the two-tailed unpaired *t* test or multiple t-test, adjusted *p*-values were calculated using the Benjamini-Hochberg method. The *p*-values are directly indicated on the figure, above the corresponding graphs. * or # $p< 0.05$; ** or ## $p< 0.01$; and *** or ### $p< 0.001$ were considered statistically significant.

Correlation analysis

Extracellular flux data was asinh transformed with a cofactor of 5. RNA-seq data were count-based normalized and variance-stabilized as described below, and *Z*-score normalization was performed

on genes from specified metabolic pathways in each compartment. To represent gene expression in the DN compartment, the weighted average of DN1-3 or Thy1-3 gene expression were calculated according to the proportion of each population in at least 3 experimental samples. The following weighted averages were used. Mouse thymus: DN1 (4%), DN2 (3%), DN3 (93%). M-ATO: DN1 (1%), DN2 (1%), DN3 (98%). Human thymus: Thy1 (0.1%), Thy2 (59.9%), Thy3 (40%). Human ATO: Thy1 (0.1%), Thy2 (79.9%), Thy3 (20%). Correlation between extracellular flux and metabolic gene expression data across all thymocyte populations (DN, ISP, SP8, and SP4 in M- and H-THY; or DN, ISP, and DP early in M- and H-ATO) were calculated using the ggcorr R package. Adjusted *p*-values for each Pearson correlation coefficient were calculated using the Benjamini-Hochberg method, and plots were created using the ggplot2 R package.

RNA sequencing and data analysis

The preparation and analysis of mouse thymus and M-ATO RNA-seq libraries for thymic subsets have been previously described and raw sequence files are available at NCBI's GEO (GSE146224) (125). For the new human thymus and H-ATO libraries reported here, RNA was extracted from each of the indicated human thymic or H-ATO-derived populations isolated by FACS, as described above and in **Table S3-1**. Total RNA was isolated using the RNeasy Micro kit (**Qiagen**). Sequencing libraries were prepared with the Ovation RNA-seq system V2 kit (**NuGEN**). Paired-end 150 bp sequencing was performed on the Illumina HiSeq 4000.

The STAR ultrafast universal RNA-seq aligner v2.7.0d (77) was used to align reads to a genome index including both the genome sequence (GRC38 primary assembly) and the comprehensive genome annotation from Gencode (version 36). Alignment files were used to generate strand-specific, gene-level count summaries with STAR's built-in gene counter.

Expression estimates provided were computed in units of fragments per kilobase of mappable length and million counts (FPKMs). Count-based normalized and variance-stabilized data (78) was used for all ordination, differential and clustering analyses, and all figures unless otherwise noted. Principal component analysis (PCA) was performed with the function prcomp in R (https://www.R-project.org/) using standardized data as input. To facilitate the integration of the datasets, standardization was performed independently prior to PCA.

Differential expression analyses was performed with DESeq2 (Bioconductor, v3.7, RRID:SCR_015687) (78). We performed pair-wise comparisons between sequential thymocyte populations within human thymic or H-ATO compartments, or between analogous human thymic and H-ATO-derived populations. We defined a set of 769 variable genes (**Table S3-2**) for further analyses as: fold-change greater than 2, Benjamini-Hochberg adjusted Wald test *p*-value less than 0.01 in at least one pair-wise test, and a minimum expression of 5 FPKMs in at least one sample; genes with less than half-count per million in all samples, count outliers, or low mappability (<50bp) were filtered out from the differential gene expression analysis (20, 78, 125). This set of most significantly variable genes was subjected to model-based clustering using MBCluster.Seq (79) to classify them based on their overall abundance profile across populations (**Figure 2-1B**). We set the starting number of clusters to 100, and then manually merged them to generate a set of 16 non-redundant gene classes.

Functional enrichment for genes selected in the tests and clusters above was performed with Metascape (80). All heatmap visualizations were created using pheatmap R package, and all line plots were created using spline function and ggplot2 package in R.

Results

Experimental Approach for Metabolic Profiling of Murine and Human T Cell Differentiation

To investigate the metabolic landscape of thymic T cell differentiation in murine and human systems, we followed the workflow presented in **Figure 3-1A**. We acquired transcriptional datasets in analogous thymocyte populations from murine thymus (M-THY hereafter), human thymus (H-THY hereafter), and *in vitro* systems. To generate *in vitro* thymocytes, HSPCs isolated from mouse bone marrow or human cord blood were seeded in mouse ATO (M-ATO hereafter) and human ATO (H-ATO hereafter) systems respectively (47, 125). Thymocytes were isolated from primary thymus or ATO-derived cultures and subjected to bulk RNA-sequencing, or extracellular flux measurements that reflect glycolytic and oxidative phosphorylation (OXPHOS) activity. Thymocyte developmental stages included in the analyses are shown (**Figure 3-1B, Table S3-1**). As the SP4 population is scarce in H-ATOs, these were not collected for transcriptional analysis.

Transcriptional Analysis of Primary Human Thymus and H-ATO

We recently reported that transcriptional regulation in M-ATO-derived thymocytes recapitulates T cell developmental programs in mouse thymus (125). Here, we similarly examined transcriptional profiles of phenotypically identical populations from primary human thymus and H-ATO.

Principal-component analysis (PCA) using global genome-wide expression profiles showed that H-THY and H-ATO-derived populations overall exhibited a similar progression

along the first and second principal components (PC1: 23.34% variance; PC2: 12.96% variance) (**Figure 3-2A**).

Next, we performed unsupervised hierarchical model-based clustering on human thymic and ATO-derived populations. Due to differences in baseline gene expression, we first normalized gene expression data and then classified genes by their overall expression profile using an unsupervised approach and stringent thresholds. We used pairwise statistical tests between sequential populations within each sample tissue (e.g., H-THY ISP4 versus H-THY DP early), or between equivalent populations in thymic and ATO tissues (H-THY SP8 versus H-ATO SP8), to identify a set of most variable genes (769 human genes) that were then subject to hierarchical model-based clustering (provided in **Table S3-2**). In a summary heatmap shown in **Figure 3-2B**, we reordered each cluster of differentially expressed genes to match peak expression with developmental stage (DN to SPs). We included annotations and representative genes for each cluster based on our previous transcriptional analyses in murine thymocytes (125). Human thymic and ATO gene expression patterns were highly similar overall and featured key markers of T cell development.

Gene ontology (GO) enrichment analysis of the top 500 ranked genes in PC1 and PC2 revealed that the category of metabolic processes was highly enriched in both PC1 and PC2 (**Figure 3-2C**). Several metabolic genes were also classified as being differentially expressed during development and clustered together, e.g., *HK2, ATIC, AHCY,* and *UCK2* (**Figure 3-2B**). Thus, metabolic gene signatures are a major component of the transcriptional differences between human thymocyte stages.

Transcription of Core Metabolic Pathways in Primary Murine and Human Thymocytes

As global transcriptional analyses suggested that significant metabolic changes occur during thymopoiesis, we next performed a supervised analysis using a manually curated list of genes originally derived from the KEGG database. We focused on genes encoding enzymes directly involved in major oxidative and biosynthetic pathways, particularly glycolysis, *de novo* purine nucleotide synthesis, tricarboxylic acid cycle (TCA), and the electron transport chain (ETC) (**Figure 3-3**). We also analyzed other essential metabolic pathways, including fatty acid beta-oxidation (FAO), pentose phosphate pathway (PPP), *de novo* pyrimidine nucleotide synthesis, and the purine salvage pathway (**Figure S3-1**). In both primary murine and human thymus, the expression of most glycolytic genes, such as *LDHA, HK2, GAPDH, PGAM1,* and *TPI1* were high at the DN1-DN3 or Thy1-3 stages (**Figure 3-3A-B**). After a marked peak at the ISP stage, transcription dramatically declined in the DP thymocytes. The subsequent SP stages showed some recovery in the transcription of glycolytic genes. Notably, enzyme isoforms in the glycolytic pathway displayed reciprocal gene expression at the ISP-DP transition: *Ldhb* vs *Ldha* (M-THY), *Pfkp* vs *Pfkl* (M-THY), *HK1* vs *HK2* (M-THY and H-THY), *PFKP* vs *PFKM* (H-THY). Overall, genes within the *de novo* purine synthesis, TCA and ETC pathways showed a similar pattern in primary thymocytes as seen for the glycolytic genes (**Figure 3-3A-B**, **Figure S3-1A-B**). FAO, PPP, *de novo* pyrimidine synthesis, and purine salvage pathways also showed a marked fall in transcription at the DP stages in primary thymus samples (**Figure S3-1A-B**). Thus, murine and human thymocytes isolated from primary thymus shared a highly conserved pattern of core metabolic programs at distinct stages of T cell development, with a peak in transcription during the transitional ISP stage and a dramatic fall in the early (TCR^-) and late (TCR^+) DP stages.

Transcriptional Pattern of Core Metabolic Programs During Murine and Human *In Vitro* Thymopoiesis

Next, we examined metabolic transcriptional patterns in murine and human *in vitro* thymopoiesis using the ATO system. Similar to the primary thymocytes in M-THY and H-THY, coordinated metabolic gene expression patterns were seen in the M-ATO and H-ATO: glycolytic gene expression, including that of *LDHA, HK2, GAPDH, PGAM1,* and *TPI1,* was highest in DN-ISP stages, decreased at the DP stages, and recovered at the SP stages (**Figure 3-3C-D**). Enzyme isoform switching was again seen in the M-ATO and H-ATO at the ISP-DP transition in *Ldhb* vs *Ldha* (M-ATO), *Pfkp* vs *Pfkl* (M-ATO), and *HK1* vs *HK2* (H-ATO). Gene expression in the nucleotide synthesis, TCA, FAO, and PPP pathways was also lowest at the DP stages in both ATO systems as well. (**Figure 3-3C-D, Figure S3-1C-D**). A subset of metabolic genes showed an inverse pattern, e.g., *DLST* (TCA) and *ADA* (purine salvage) were upregulated at the DP stage across all conditions (in both species, *in vivo,* and *in vitro*) (**Figure 3-3; Figure S3-1**).

Although metabolic gene expression was largely conserved across *in vivo* and *in vitro* conditions, some differences were noted. In contrast to DN1 cells in primary mouse thymus, DN1 cells in the M-ATOs exhibited high metabolic gene expression levels that were sustained rather than peaking at the ISP8 stage; moreover, the sharp downregulation of metabolic gene expression seen in the M-THY was delayed in the M-ATO, with the nadir observed at the DP late instead of DP early stage (**Figure 3-3A, C; Figure S3-1A, C**). These subtle differences were also observed in the H-ATO. However, the starkest difference between H-ATO and H-THY samples was the uncoordinated expression of mitochondrial ETC genes in the H-ATO (**Figure 3-3B, D**; **Figure S3-1B, D**).

Metabolic Extracellular Flux Dynamics are Conserved in Murine and Human Thymocytes

To investigate whether metabolic gene transcription patterns reflect bioenergetic changes during T cell development, we assessed metabolic extracellular flux data in developing T cells from primary human thymus and murine thymus (**Figure 4A-B**). We measured extracellular acidification rate (ECAR) and oxygen consumption rate (OCR), indicators of glycolysis and oxidative phosphorylation (OXPHOS) respectively, at basal conditions and after addition of pharmacological agents. When the drug FCCP is added, oxygen consumption is uncoupled from ATP synthesis and cells are induced to utilize their maximal respiratory capacity. Given the RNA-seq results, we chose to compare total DN, ISP, and the subset of DPs that do not yet express cell surface TCR ("DP early"), as well as SP4 and SP8 cells.

In primary murine thymus, DN and ISP8 cells had higher basal ECAR and OCR than DP and SP cells (**Figure 3-4A**). DN cells exhibited a robust response to mitochondrial uncoupling with high maximal OCR and spare respiratory capacity (SRC) (**Figure 3-4A, Figure S3-2A**). In contrast, DP early cells showed the lowest basal ECAR and OCR, and essentially no change between basal and maximal OCR in response to FCCP stimulation. ISP8 cells had similar basal ECAR and OCR to DN cells but were less able to respond to FCCP addition compared to DN cells.

The pattern of metabolic flux was similar in human thymus, with DN and ISP4 cells showing high basal ECAR, basal OCR, maximal OCR, and SRC (**Figure 3-4B**, **Figure S3-2B**). Again, DP cells showed low basal ECAR and OCR, and almost no difference between OCR at baseline and in response to FCCP stimulation. Interestingly, in murine and human primary thymus, there was higher glycolytic and oxidative phosphorylation activity in SP8 cells compared to SP4 cells, as shown by significantly higher basal ECAR and OCR (**Figure 3-4A-B**).

Thus, as suggested by transcriptional profiles in primary human and murine thymocytes, metabolic activity is highest in the early DN-ISP populations, drops significantly at the DP early stage, and shows some recovery in the SP populations.

Metabolic Flux Dynamics in Thymocytes Generated *In Vitro*

We next measured glycolytic activity and mitochondrial respiration in the DN, ISP, and DP early populations generated *in vitro* from M-ATO and H-ATO. SP populations from the ATO were not included due to the high cell numbers (>300,000 cells) required for robust extracellular flux measurements per experiment. In the M-ATO, DN cells had the highest basal ECAR and OCR, as well as the strongest response to FCCP addition with high maximal OCR and SRC (**Figure 3-4C; Figure S3-2C**). Basal ECAR and OCR in ISP8 cells were higher than that of DP early cells but lower than that of DN cells; moreover, ISP8 cells were less able than DN cells to respond to mitochondrial uncoupling. DP early cells showed the lowest basal ECAR and OCR, and very little difference between basal and maximal OCR.

Similar to M-ATOs, DN and ISP4 cells from H-ATOs exhibited high basal ECAR and OCR, and a robust response to FCCP stimulation producing high maximal OCR and SRC (**Figure 3-4D, Figure S3-2D**). DP early cells showed the lowest basal ECAR and OCR, and essentially no difference in baseline and maximal OCR.

No major differences in OCR and ECAR results were seen when comparing M-THY and M-ATO thymocytes, other than a lower SRC in DN cells from M-ATO compared to those from M-THY (**Figure S3-2E**). H-THY and H-ATO thymocytes also showed comparable OCR and ECAR results, except that basal ECAR was higher in DP early cells from H-ATO than that from H-THY (**Figure S3-2F**).

Overall, the ATO systems recapitulated the metabolic shift from high to low glycolytic and OXPHOS activity between the DN to DP stages observed in primary thymus. Thus, *in vivo* and *in vitro* developing thymocytes reveal a strikingly conserved pattern in metabolic activity during thymopoiesis.

Correlation Analyses of Metabolic Transcriptional and Bioenergetics Profiles in Thymus and ATO T Cell Development

As transcriptional and bioenergetics data appear to match in all systems except the ETC in the H-ATO, we performed further quantitative analyses to uncover the relationship between the two datasets. Correlation analyses between gene expression data and extracellular flux measurements were performed across thymocyte populations in M-THY, M-ATO, H-THY, or H-ATO (**Figure 3-1A**). Transcription levels of most glycolytic genes positively correlated with glycolytic flux results across all thymocyte sources (M-THY, M-ATO, H-THY, H-ATO), including *LDHA*, *HK2, PGAM1*, and *PGK1*; again, the few glycolytic genes that showed negative correlation with ECAR were isoforms noted earlier, e.g., *Ldhb* and *Pfkp* in M-ATO, and *HK1* in H-THY and H-ATO (**Figure 3-5A-D**, **Table S3-3**).

In M-THY, M-ATO, and H-THY, RNA levels of most ETC pathway genes were positively correlated with mitochondrial respiration activity (**Figure 3-5A-C**). In keeping with the disorganized pattern of ETC gene expression seen in the H-ATOs (**Figure 3-3D**, **Figure 3-1D**), there was an overall inverse correlation of transcription with mitochondrial respiration activity in this model (**Figure 3-5D**). Nonetheless, the ETC genes *COX5A, NDUFA8,* and *NDUFV1* were consistently positively correlated with OCR in all systems.

Previously, the ImmGen report in murine thymus showed that the downregulation of ribosomal genes was associated with the decrease in metabolic genes at the DP stage (63). Therefore, we next probed whether structural ribosomal gene expression patterns strongly correlated with metabolic flux data. Mitochondrial ribosomal gene expression was the highest at the DN-ISP stages and lowest at the DP early-DP late stages in M-THY, H-THY, and M-ATO (**Figure 3-6A-D**). However, in the H-ATOs, the majority of mitochondrial ribosomal genes showed an uncoordinated expression pattern similar to that of the ETC genes (**Figure 3-6D, Figure 3-3D**). Correspondingly, mitochondrial ribosomal expression positively correlated with basal mitochondrial respiration rates in M-THY, H-THY, and M-ATO (**Figure 3-6E-G**), while most mitochondrial ribosomal genes in the H-ATO correlated inversely or not at all with basal OCR, as seen previously with the ETC genes (**Figure 3-6H, Figure 3-5D**). We also analyzed cytoplasmic ribosomal gene expression in H-THY and H-ATO, both of which showed global downregulation at the DP stages (**Figure S3-3A-B**). In contrast to the mitochondrial ribosomal genes, cytoplasmic ribosomal gene expression positively correlated with basal glycolytic and respiration rates not only in the H-THY but also in the H-ATO (**Figure 3-3C-D**).

Lastly, we assessed the gene expression of key signaling molecules and transcription factors that are known to regulate metabolic programs (120, 126-128), and analyzed how well their transcriptional pattern correlated with extracellular flux data (**Figure S3-4A-H**). Since changes in basal ECAR and basal OCR were closely associated in thymocyte populations, we focused our analyses on basal OCR. First, we looked for metabolic regulators whose gene expression showed a consistently similar trend to basal OCR. In all systems, *NOTCH1* gene expression was strongly associated with basal mitochondrial respiration. Next, we examined key differences in metabolic regulator expression between primary thymus and the ATO systems.

STAT3, *STAT5*, and *NFE2L2* were positively correlated with basal OCR in both the M-ATO and H-ATO but showed poor correlation in primary murine and human thymus. Most notably, whereas *MYC* gene expression was positively correlated with basal respiration in M-THY, H-THY, and M-ATO, *MYC* was inversely correlated with basal OCR in the H-ATO system. We carefully reviewed *MYC* expression in the H-ATO and observed peak expression in the Thy1 population, and then similar expression levels in the Thy2-3, ISP4, and DP early populations (**Figure S3-4D**). The inverse correlation of *MYC* expression in the H-ATO was entirely driven by the persistence of high *MYC* expression in the DP early stage, even though DP early cells exhibit the lowest basal OCR (**Figure S3-4D, H**, **Figure 3-4D**).

Thus, correlation analyses confirmed that metabolic transcriptional profiles reflected functional metabolic activity in both primary thymus and the ATO system; mitochondrial respiration in the human *in vitro* system (H-ATO) was the sole exception to this pattern.

Thymocyte Metabolism in the Absence of TCR rearrangement

Since key metabolic transitions occur between stages undergoing TCRβ rearrangement (DN3 in mouse or ISP4 in human) and TCRα rearrangement (DP early), we tested the effect of removing TCR-dependent signaling on thymocyte metabolism using a *Rag1* (recombination activating gene 1)-deficient (*Rag1*$^{-/-}$) mouse model in the M-ATO (8, 14, 22, 24, 104). As expected, HSPCs from *Rag1*$^{-/-}$ marrow were unable to generate any CD3^{+}TCRαβ^{+} T cells in M-ATOs, and consistent with prior reports of *Rag1*$^{-/-}$ thymus, Week 3 M-ATO cultures did not progress past the DN stage (**Figure 3-7A**) (125). However, DPs have been reported to be able to develop in the *Rag1*$^{-/-}$ and *Rag2*$^{-/-}$ thymus through TCRβ chain-independent pathways (129, 130), and *RAG*-deficient human HSPCs have been shown to develop into CD3^{-}TCRαβ^{-} DP thymocytes

in H-ATOs (131). Interestingly, $CD3^-TCR\alpha\beta^-$ DPs were generated from *Rag1*$^{-/-}$ murine marrow by week 5 of M-ATO culture, allowing us to examine the metabolic flux of DP early cells and their precursors in the absence of TCR rearrangement (**Figure 3-7A**).

DN cells from *Rag1*$^{-/-}$ M-ATOs exhibited significantly decreased basal OCR and ECAR compared to that of WT DN cells (**Figure 3-7B)**. Nonetheless, similar to WT M-ATOs, basal ECAR and basal OCR dropped significantly in DP early cells from *Rag1*$^{-/-}$ M-ATOs (**Figure 3-7B)**. Thus, glycolytic and OXPHOS activity is at least partly dependent on *Rag1* activity in DN cells, but the metabolic shutdown at the DP early stage still occurs in the absence of TCR rearrangement.

Discussion

This report integrates comprehensive transcriptomics and extracellular flux data to present the first comparative analysis of metabolic dynamics during normal human and murine thymopoiesis. In addition, we show that metabolism is largely conserved during *in vitro* T cell development in which the complex multi-cellular and spatial organization of the thymus is absent. Previous studies have separately investigated microarray data in murine thymus (63), metabolic parameters in early murine thymocyte stages (61, 68), single cell RNA-seq in human thymus (132, 133), GLUT1 expression in human thymocytes (134), and metabolic parameters in activated human T cells (57, 135). Our combined analyses demonstrate that metabolic transcriptional profiles generally reflect functional metabolic activity and reveal remarkably conserved metabolic shifts during critical stages of T cell development (**Figure 3-8**). Thymocytes prior to the DP stage demonstrate peak gene expression levels of enzymes directly involved in glycolytic, TCA, and ETC pathways, as well as the highest glycolytic and OXPHOS

activity. At the DP early stage, glycolysis and mitochondrial respiration are invariably reduced in all murine and human systems, even in *Rag1*$^{-/-}$ M-ATOs. SP thymocytes exhibit metabolic gene expression and activity that is relatively increased compared to DP cells, but does not recover fully to the levels seen in early T cell development stages.

Transcriptional metabolic patterns and metabolic extracellular flux results in ATO-derived thymocytes were largely analogous to those of primary thymocytes. The fidelity of thymocyte metabolic dynamics *in vitro* is impressive, considering the differences in the microenvironment, including gas exchange, supportive tissue, and nutrient availability. Besides the lack of thymic epithelium, *in vitro* models are usually cultured in room air and media with supraphysiological cytokine concentrations, whereas the thymic medulla is thought to be hypoxic and nutrient availability is likely more localized (136). These findings suggest that, with the exception of Notch signaling, key metabolic changes during T cell development do not require the complex architecture of the primary thymus.

Despite a similar overarching pattern in development, some differences were noted between endogenous and *in vitro*-derived T cells. Our data suggests that thymocytes potentially utilize a higher fraction of their bioenergetic capacity at basal conditions *in vitro* compared to *in vivo*. This could be due to enriched media conditions. It is also possible that transcriptional differences seen in the DN1/Thy1 populations may reflect differences in HSPC origin. Although DN1 cells isolated from the thymus are transcriptionally closely related to their HSPC precursors in the marrow, exposure to the thymic microenvironment rapidly initiates transcriptional changes (20); HSPCs seeded in ATOs may be a more heterogeneous progenitor population, a minority of which are poised to launch T cell commitment (20, 47, 125). In addition, as described previously in the M-ATO, the global transcriptional profile in TCRβ^{+}CD3^{+} “DP late” cells from ATOs

partially overlaps with that of TCRβ^{-}CD3^{-} "DP early" cells from primary thymus, suggesting earlier surface expression of TCRβ/CD3 on DP cells *in vitro*; this may explain the apparent mismatch in transcriptional downregulation of core metabolic genes at the DP late stage instead of the DP early stage in the ATO (125).

Mitochondrial respiration and spare respiratory capacity are consistently low in H-ATO-derived DP early cells, yet the transcriptional regulation of the ETC and mitochondrial ribosomal genes is uncoordinated in the H-ATO. *MYC* expression appears to also be dissociated with mitochondrial respiration specifically in DP early cells in the H-ATO system. Although it is unclear why the human ATOs but not the mouse ATOs showed a lack of coordination between respiratory metabolism and ETC genes, additional regulatory mechanisms, including post-translational processes, may be controlling mitochondrial metabolism.

Loss of *Rag1* had a deleterious impact on metabolism in the earlier DN stage of T cell development, consistent with previous reports of reduced glycolytic rates in *Rag2*$^{-/-}$ DN3 cells (60). On the other hand, the downregulation of basal respiratory and glycolytic activity at the DP early stage occurred regardless of the presence of TCR rearrangement. Therefore, metabolic downregulation in DP early cells is independent of TCR-mediated signaling.

"DP early" cells by definition do not express CD3 or TCR on the cell surface, so they are either precursors to the TCRβ^{+}CD3^{+} DP late cells that have yet to undergo positive selection, or are DPs that will never generate a productive TCR complex and will eventually die by neglect (137). We only isolated live DP early cells for our metabolic analyses; nevertheless, we cannot exclude the possibility that some of the DP early cells studied were undergoing apoptosis at the time of analysis.

Alterations in cytokine signaling pathways could be contributing to the highly specific metabolic downregulation in DP early cells. IL7RA is known to be down-regulated in murine and human DP cells (138, 139); however, DPs express high levels of other pro-survival cytokine receptors (140). Cytokine signal transduction has been shown to be suppressed in DP cells by suppressor of cytokine signaling (SOCS) and restored by TCR signaling (140). Thus, a combination of environmental signals as well as intrinsic mechanisms may be instructing DP early cells to undergo behavior reminiscent of growth factor deprivation in anticipation of low survival rates (141, 142). Moreover, the rise in metabolic activity in SP cells after the DP stages could be due to a restoration of cytokine signaling sensitivity.

NOTCH1 gene expression was highly associated with metabolic changes during development, supporting models that propose an interplay between Notch signaling and metabolic processes (60, 61, 63). While our analyses show a strong correlation between specific metabolic regulators and metabolic activity during thymocyte development in primary thymus or ATO systems, definitive experiments are required to study whether transcription factors such as NRF2 (*NFE2L2*) and STAT3/5 play an important role in controlling metabolism *in vitro*.

Though several studies have probed the mechanisms required for the DN-DP metabolic transitions in mice, further studies are needed to study the mechanisms and role of metabolic shifts in human thymocytes. This work will inform the thymocyte metabolism field by identifying critical species-conserved metabolic profiles in endogenous and *in vitro* murine and human thymic T cell differentiation.

Acknowledgements

We gratefully acknowledge the expert technical assistance of Jeffrey Calimlim, Felicia Codrea, and Jessica Scholes from the UCLA Broad Stem Cell Research Center (BSCRC) Flow Cytometry Core; the expert technical assistance of Dr. Linsey Stiles from the UCLA Mitochondrial and Metabolism Core; the Technology Center for Genomics and Bioinformatics (TCGB) at UCLA and the Translational Pathology Core Laboratory (TPCL) at UCLA; as well as the Next Generation Sequencing Core at the Salk Institute for Biological Studies. We thank Dr. Christopher S. Seet from UCLA for reviewing the manuscript. We thank Dr. Felix J. Hartmann and Dr. Sean C. Bendall from Stanford University and Katherine Sheu from the Hoffmann Lab at UCLA for assistance with developing R code for analysis, and Dr. Kai Yang and Dr. Hongbo Chi for sharing their thymocyte Seahorse assay protocol.

Author contributions

Conceptualization, V.S., M.S., G.M.C, U.B.; Methodology, V.S. and M.S.; Formal analysis, V.S. and M.S.; Investigation, V.S., M.S., A.M.-H., P.C., A.Z., S.L., S.C.D., Y.Z.; Data Curation, V.S., K.E.K-U., D.C.; Human Thymus Sample Contribution, C.P.; Writing – Original Draft, V.S., and G.M.C.; Writing – Review and Editing, V.S., M.S., D.C., S.C.D., and G.M.C.; Supervision, G.M.C.; Funding acquisition, G.M.C., U.B.

Conflicts of interest

A.M.-H. and G.M.C. are listed on patents relating to this work. A.M.-H. and G.M.C. are co-founders of PLUTO Immunotherapeutics Inc.

Figures

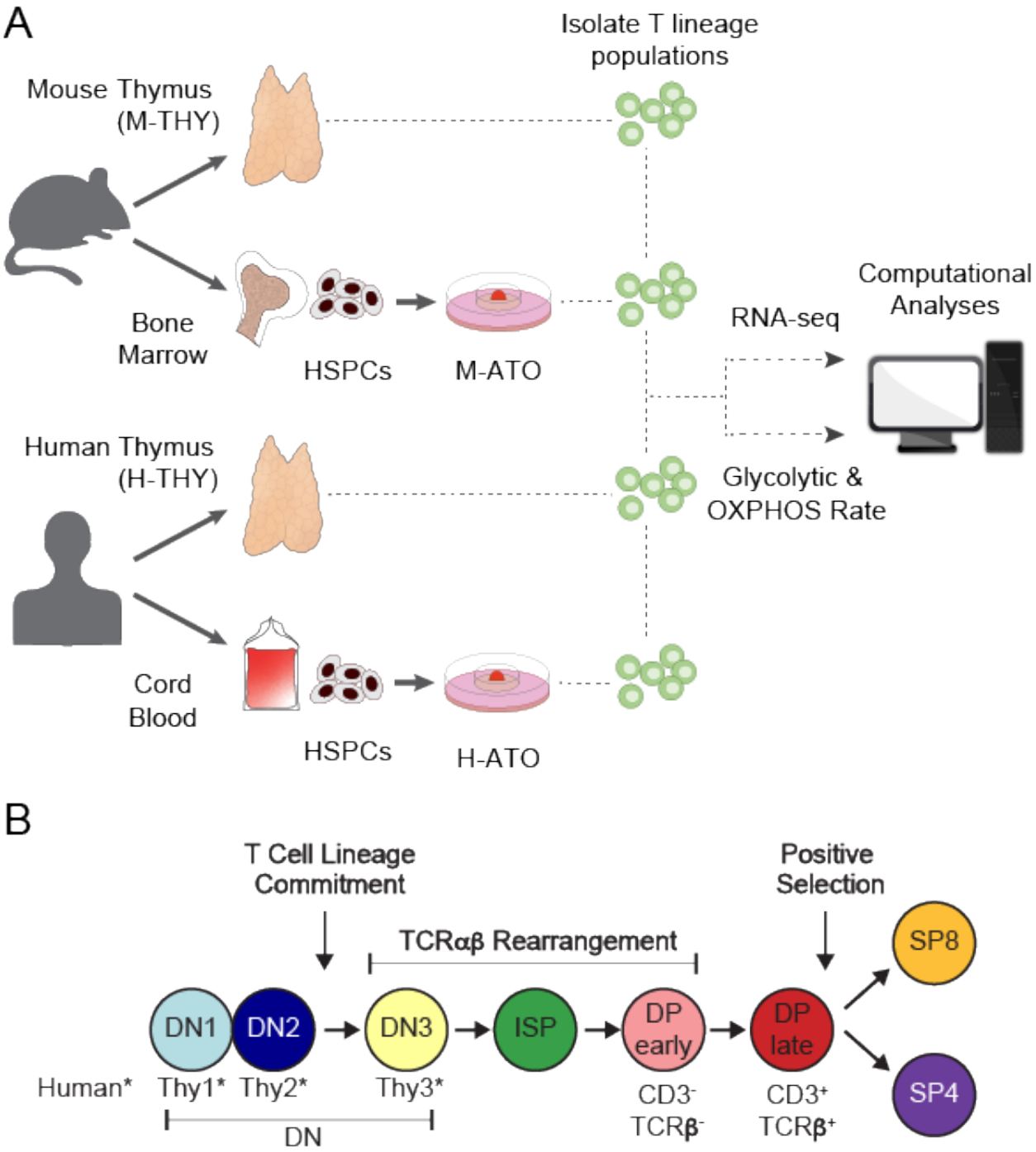

Figure 3-1: Experimental Schema for Metabolic Analysis of Murine and Human T cell Development in Primary Thymus and *In Vitro* ATO Cultures

(**A**) Murine (M-THY) and human (H-THY) thymus tissue were harvested for thymocytes. HSPCs isolated from mouse bone marrow or human cord blood were seeded in M-ATO and H-ATO systems respectively. T lineage populations isolated from each tissue were subject to RNA-seq or extracellular flux measurements to determine glycolytic and respiration rates (Seahorse Assay). Metabolic transcriptional and flux results were integrated to determine statistical correlation between datasets.

(**B**) Schematic of T lineage populations isolated for RNA-seq analyses or Seahorse Assays. Detailed population phenotypes for isolation are provided in **Table S3-1**. (*****DN populations are named DN1-3 in mouse, and Thy1-3 in human.)

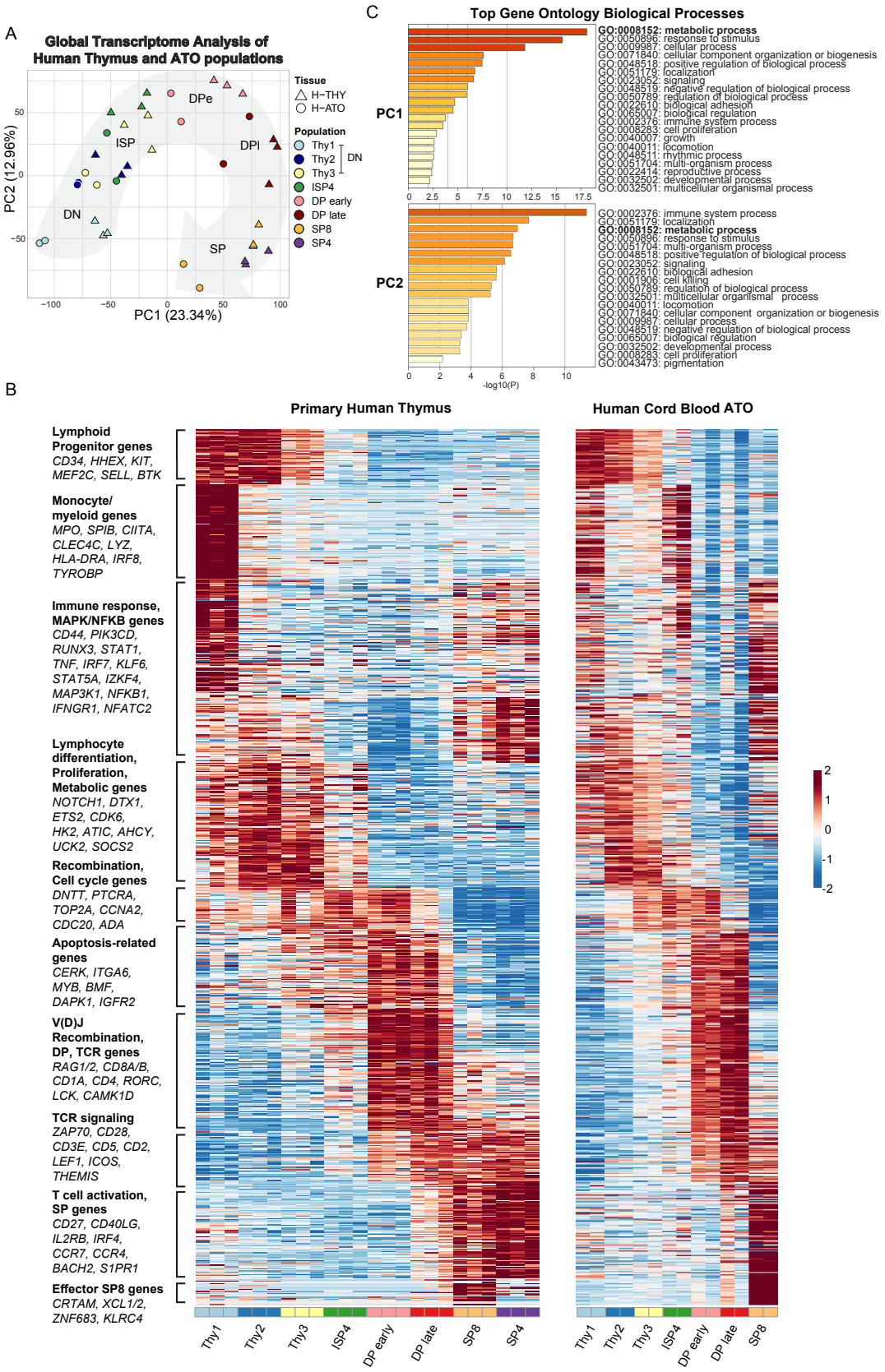

Figure 3-2: Global Transcriptional Profiling of Human T cell Differentiation

(**A**) Principal-component analysis (PCA) of gene expression for human thymic and H-ATO-derived populations. PC1 and PC2 are shown along with the percentage of gene expression variance explained. Clustering was obtained with data from all detected genes without additional filters. Population phenotypes from each source are provided in **Table S3-1**. SP4 population was not collected from H-ATO. Background arrow shows direction of differentiation. (n=3 independent replicates for H-THY; n=2 for H-ATO)

(**B**) Hierarchical model-based clustering of 769 highly variable genes classified as differentially expressed (Wald adjusted p value < 0.01, fold change > 4) within and between human thymic and ATO-derived populations. The x axis indicates populations isolated for analysis. Each heatmap represents *z*-scores of normalized variance-stabilized gene expression data. Annotations correspond to representative functional categories for genes in each major cluster. Representative genes in each cluster are shown; the full list of genes as ordered in the heatmap is provided in **Table S3-2**. (n=3 independent replicates for H-THY; n=2 for H-ATO)

(**C**) Top GO terms significantly enriched in PC1 and PC2.

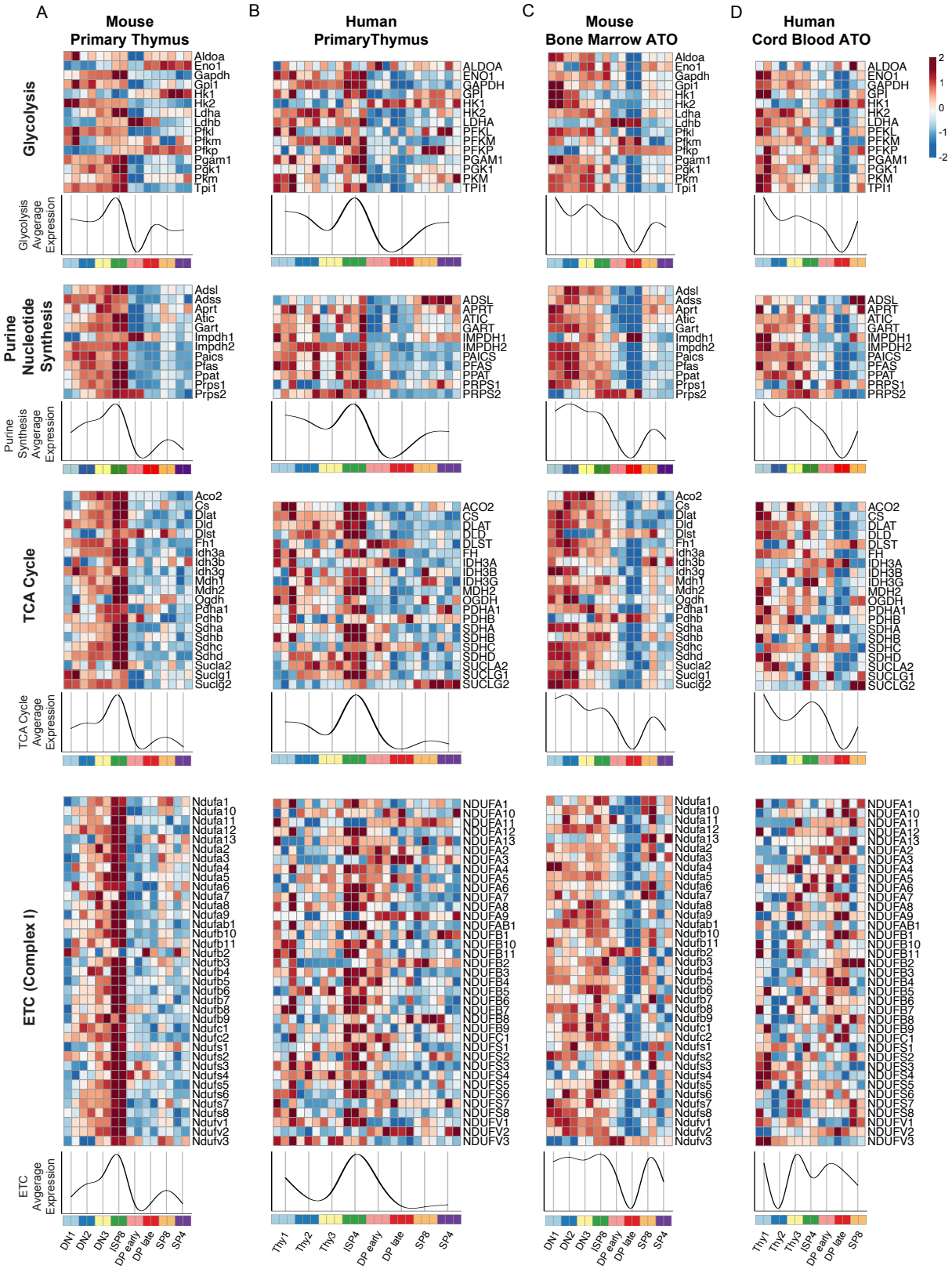

Figure 3-3: Core Metabolic Pathways Display Similar Gene Expression Pattern in Murine

and Human Thymocyte Development

(**A-D**) Heatmaps of metabolic gene expression patterns in (**A**) primary mouse thymocytes (M-THY), (**B**) primary human thymocytes (H-THY), (**C**) mouse bone marrow ATO (M-ATO), and (**D**) human cord blood ATO (H-ATO). Major metabolic pathways are displayed: Glycolysis, nucleotide synthesis, TCA cycle, and ETC (*only de novo purine synthesis and an abbreviated ETC heatmap for Complex I is shown, additional nucleotide synthesis pathways and ETC complexes are included in* **Figure S3-1**). Each individual heatmap represents *z*-scores of normalized variance-stabilized gene expression data. Line plots represent the average *z*-score for all genes in the heatmap. The x axis indicates populations isolated for analysis. SP8 and SP4 are distinct lineage fates but are represented in a linear progression for visualization purposes. (n=2 independent replicates per population in M-THY; n=3 in H-THY; n=2 in M-ATO; n=2 in H-ATO)

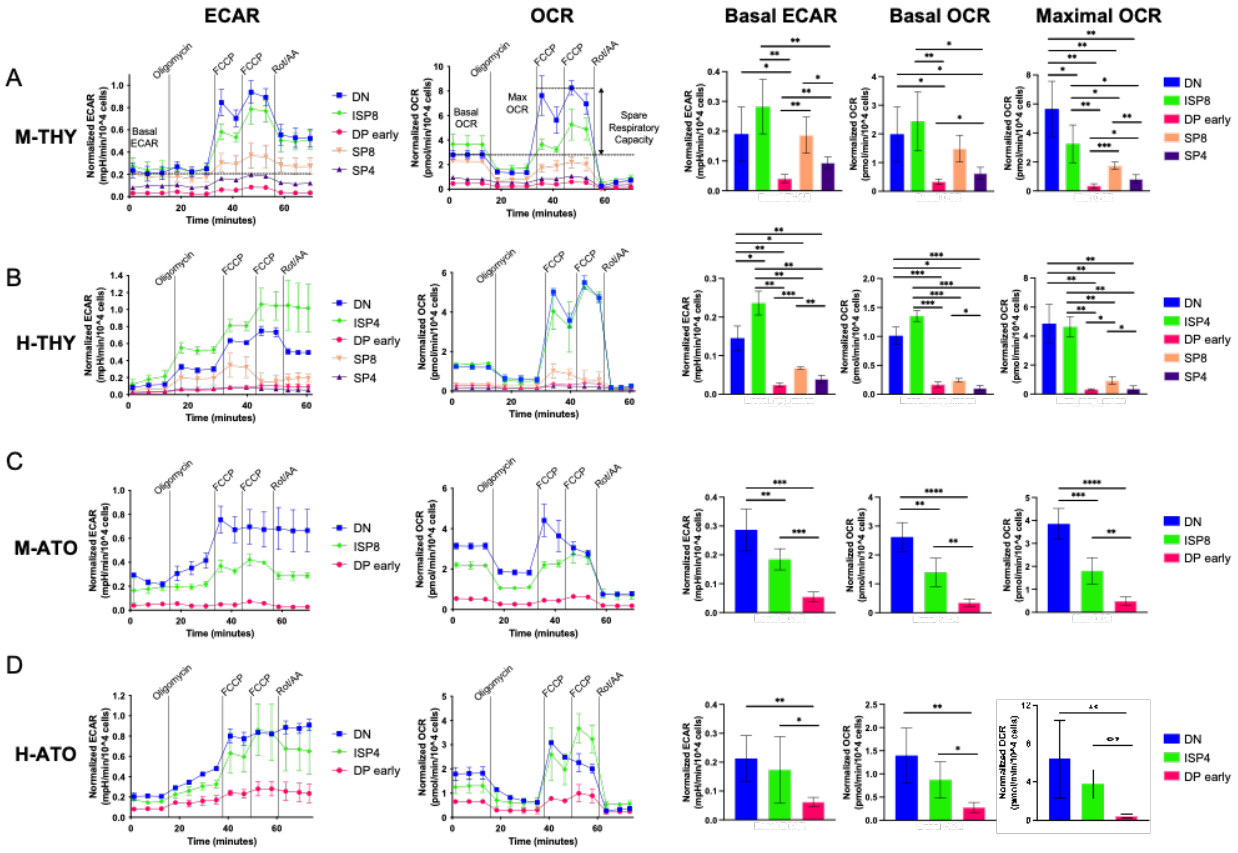

Figure 3-4: Metabolic Flux Dynamics in Primary and *In Vitro* Murine and Human Thymocytes

(**A-D**) Extracellular flux analyses of thymocyte populations in (**A**) M-THY, (**B**) M-ATO, (**C**) H-THY, and (**D**) H-ATO. ECAR (left) and OCR (right) measurements are displayed for each time point over the course of several pharmacologic agents: oligomycin, FCCP, and Rotenone/Antimycin (Rot/AA). Line plots on the left show one representative experiment out of n=6 independent experiments in M-THY; n=6 M-ATO; n=3 H-THY (except for ISP4: n=2); n=6 H-ATO (except for ISP4: n=5). Symbols and error bars represent mean +/- sd for 2-4 technical replicates (wells). Measurements are normalized to cell number per well. The bar graphs on the right consist of aggregated data from all experiments. Basal ECAR, basal OCR, and maximal OCR

for each population were calculated as described in methods and compared. (error bars: sd, significance: multiple t-test p values * $p < 0.05$; ** $p < 0.01$, *** $P < 0.001$)

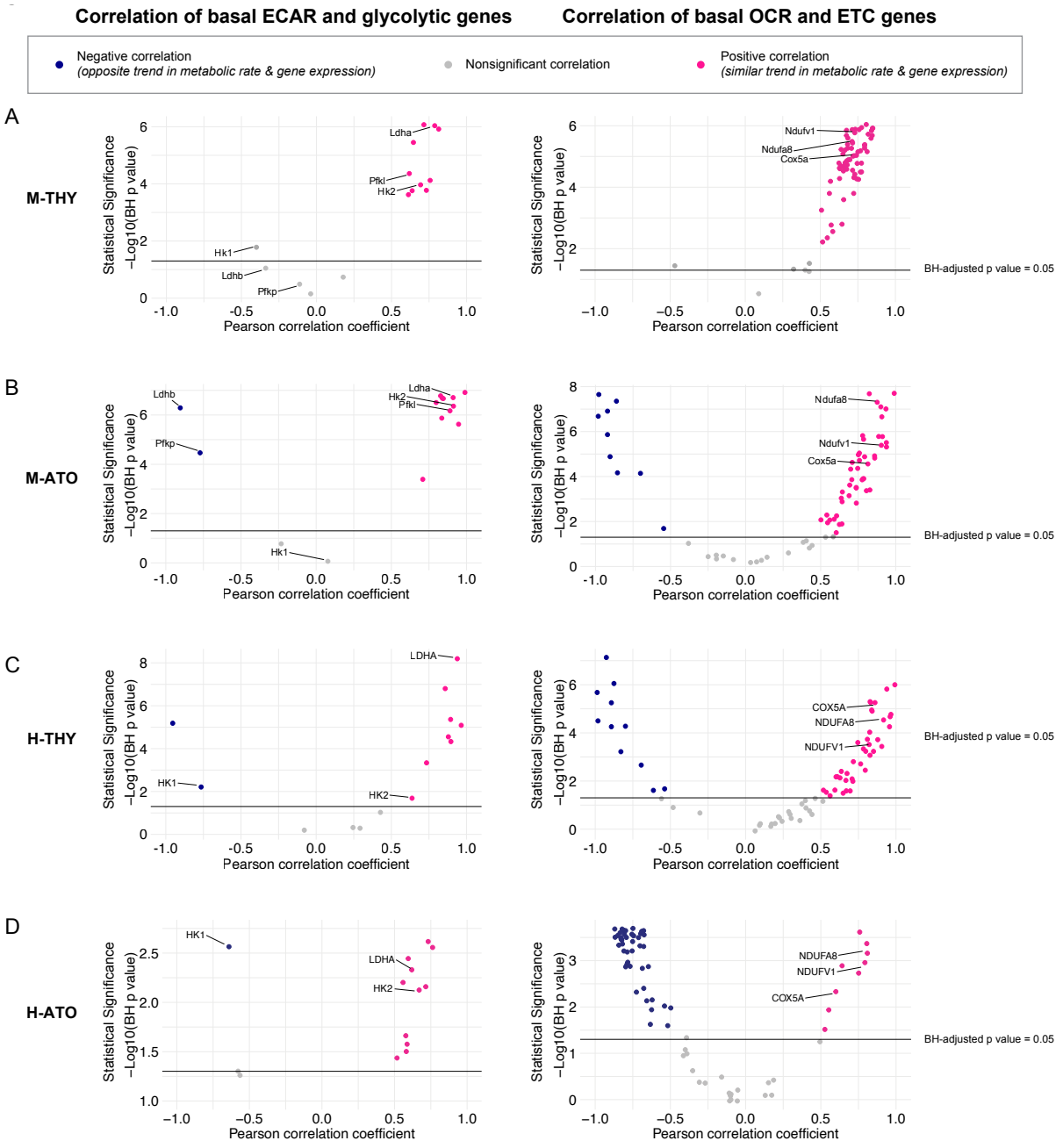

Figure 3-5: Correlation between Glycolytic or OXPHOS Transcriptional and Extracellular Flux Data in Murine and Human Thymocytes

(**A-C**) Scatter plots show correlation between (left) glycolytic enzyme gene expression and basal glycolysis (ECAR), or (right) correlation between electron transport chain gene expression and basal respiration (OCR) in (**A**) M-THY, (**B**) M-ATO, and (**C**) H-THY, and (**D**) H-ATO. The x

axis represents the Pearson correlation coefficient R values calculated for individual genes within the specified metabolic pathway for all cell populations for which respective extracellular flux data was collected. The y axis represents the statistical significance of each R value using -log10 of Benjamini-Hochberg adjusted p-values. Solid black line indicates an adjusted p-value of 0.05; all R values above the line are statistically significant. Genes with R values >0.5 (pink) are positively correlated with metabolic flux data, while genes with R values <-0.5 (blue) are negatively correlated with metabolic flux data. Nonsignificant or weak correlation R values >-.05 or <0.5 are indicated in grey. Certain genes of interest are indicated. (M-THY: n=6 flux analysis values for 5 populations, n=2 RNA-seq replicates; H-THY: n=3 flux analysis values for 5 populations, n=3 RNA-seq replicates; M-ATO: n=6 flux analysis values for 3 populations, n=2 RNA-seq replicates; H-ATO: n=6 flux analysis values for 3 populations, n=2 RNA-seq replicates)

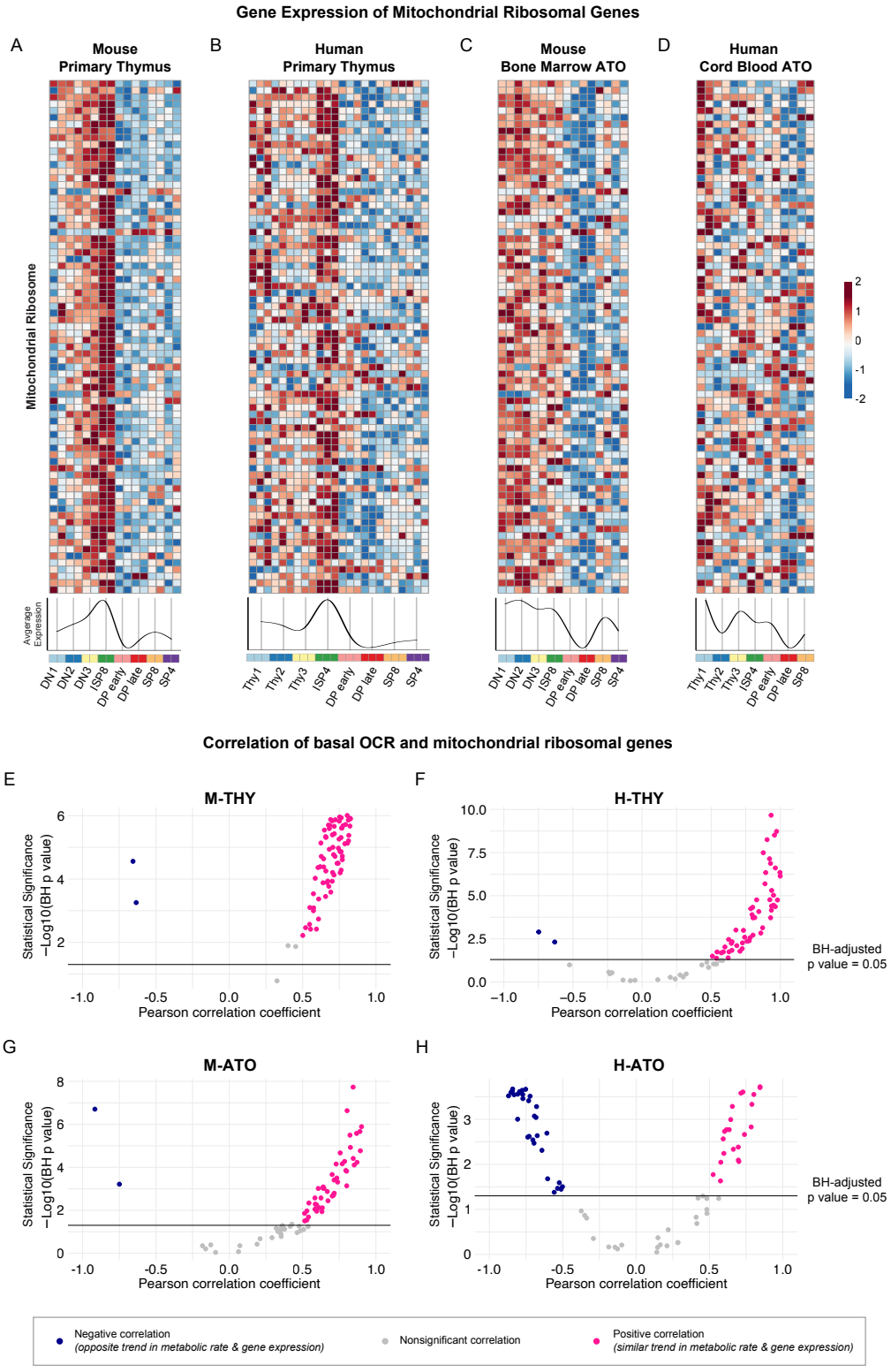

Figure 3-6: Correlation between Mitochondrial Ribosome Gene Expression and Basal Respiration throughout Murine and Human Thymocyte Development

(**A-D**) Heatmaps and summary line plots of mitochondrial ribosomal genes in (**A**) M-THY, (**B**) H-THY, (**C**) M-ATO, and (**D**) H-ATO. The x axis represents cells sorted from progenitor (DN1 or Thy1) to mature single-positive (SP) T cells. Each individual heatmap represents *z*-scores of normalized variance-stabilized gene expression data. Line plots represent the average *z*-score for all genes in the heatmap. (n=2 independent replicates per population in M-THY; n=3 in H-THY; n=2 in M-ATO; n=2 in H-ATO)

(**E-H**) Scatter plots show correlation between (**E**) mitochondrial ribosomal genes and basal respiration (OCR) in (**E**) M-THY, (**F**) H-THY, (**G**) M-ATO, and (**H**) H-ATO. The x axis represents the Pearson correlation coefficient R values calculated for individual genes within the specified metabolic pathway for all thymocyte populations for which respective extracellular flux data was collected. The y axis represents the statistical significance of each R value using -log10 of Benjamini-Hochberg adjusted p-values. Solid black line indicates an adjusted p-value of 0.05; all R values above the line are statistically significant. Genes with R values >0.5 (pink) are positively correlated with metabolic flux data, while genes with R values <-0.5 (blue) are negatively correlated with metabolic flux data. Nonsignificant or weak correlation R values >-.05 or <0.5 are indicated in grey. (M-THY: n=6 flux analysis values for 5 populations, n=2 RNA-seq replicates; H-THY: n=3 flux analysis values for 5 populations, n=3 RNA-seq replicates; M-ATO: n=6 flux analysis values for 3 populations, n=2 RNA-seq replicates; H-ATO: n=6 flux analysis values for 3 populations, n=2 RNA-seq replicates)

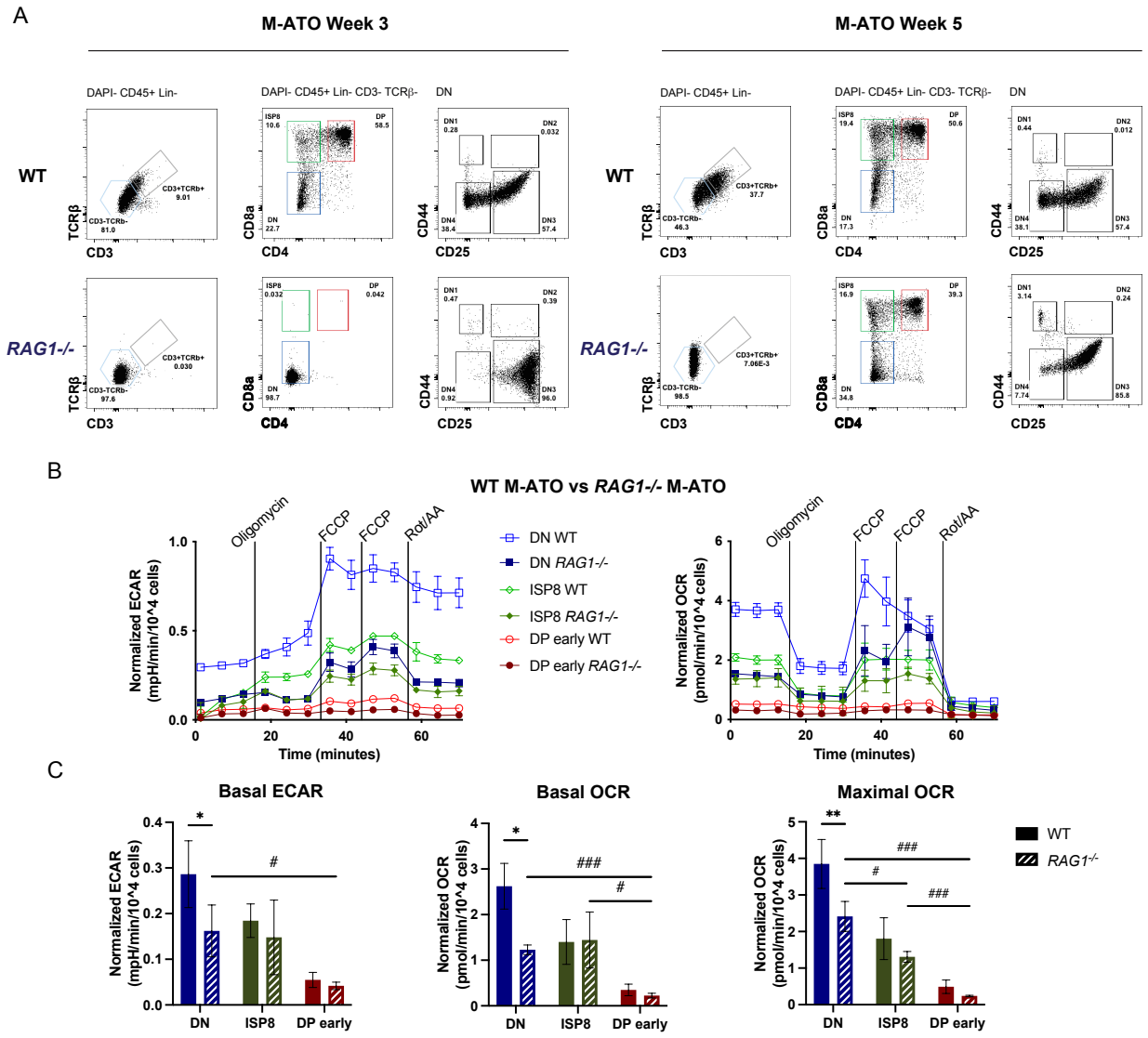

Figure 3-7: Metabolic Flux Dynamics in M-ATO-derived Thymocytes in the Absence of RAG-1-mediated TCR Rearrangement

(**A**) Representative flow cytometry analysis of thymocyte populations from Week 3 and 5 M-ATOs derived from WT and *Rag1*$^{-/-}$ mouse bone marrow.

(**B**) Extracellular flux analyses of thymocyte populations from Week 3 M-ATOs derived from WT or Week 5 M-ATOs derived from *Rag1*$^{-/-}$ mouse bone marrow HSPCs.

(C) Comparison of basal ECAR, basal OCR, maximal OCR, SRC, and OCR/ECR ratio between thymocyte populations from M-ATOs derived from WT or *Rag1*$^{-/-}$ bone marrow HSPCs. (WT: n=6, *Rag1*$^{-/-}$: n=3 independent experiments)

(error bars: sd, significance: multiple t-test p values, comparisons between WT and *Rag1*$^{-/-}$ ATO populations denoted by *; comparisons between *Rag1*$^{-/-}$ ATO populations denoted by #. * or # p <0.05; ** or ## p<0.01; *** or ### p<0.001)

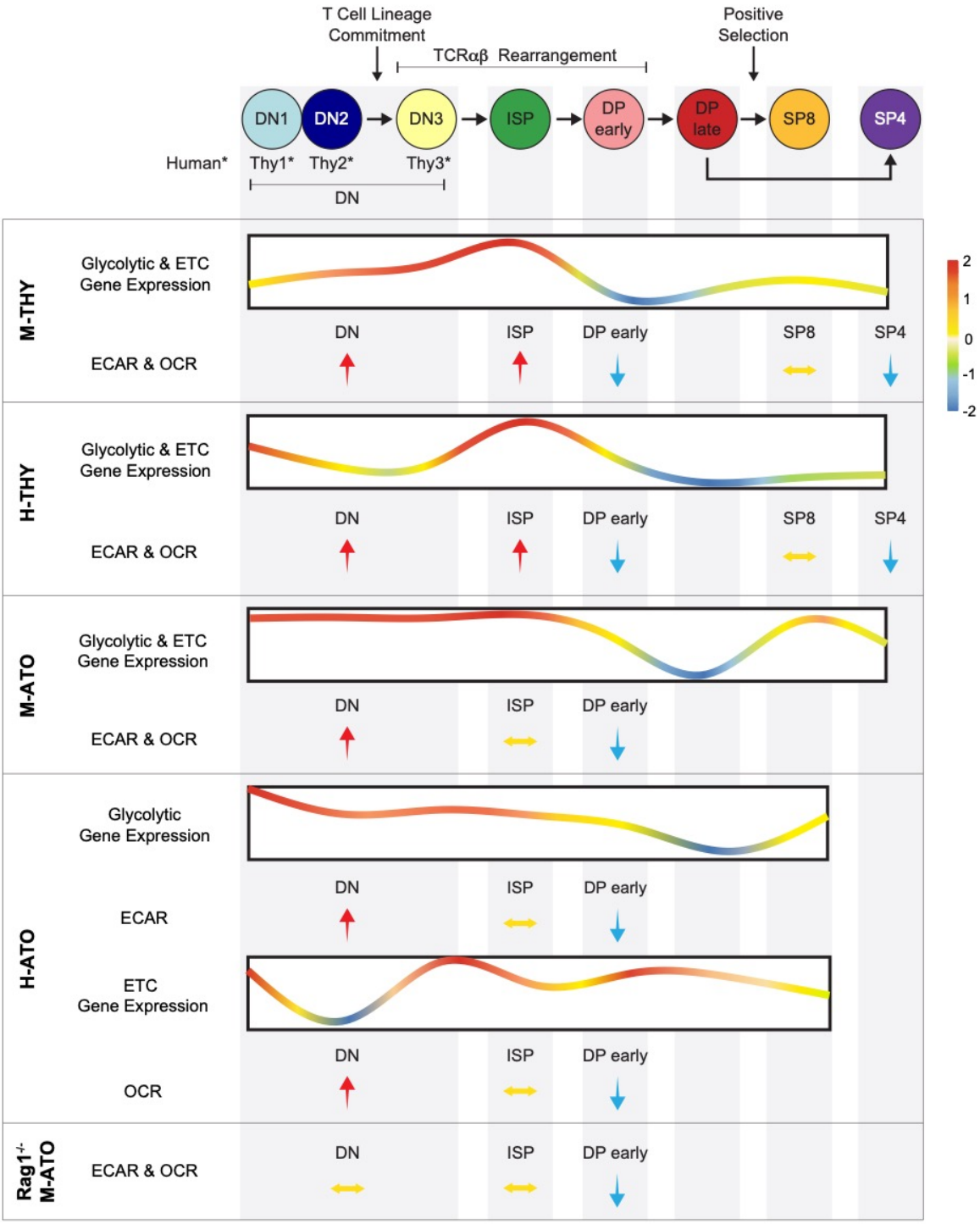

Figure 3-8: Summary of Metabolic Transcriptional and Extracellular Flux Data in Murine and Human Thymic and *In Vitro*-derived Thymocytes

Schematic summarizing metabolism dynamics throughout thymocyte development in M-THY, H-THY, M-ATO, H-THY, H-ATO, and *RAG1*$^{-/-}$ M-ATO. Glycolytic and ETC gene expression patterns are represented with line plots. Color scale indicates relative fold change. Relative changes in extracellular flux between thymocyte populations are represented with arrows. H-ATO glycolytic and ETC results are shown separately. (*DN populations are named DN1-3 in mouse, and Thy1-3 in human.)

Chapter 4 – Conclusion

Immune health requires ongoing T cell generation from HSPCs in the thymus. For instance, increased incidence of infections and cancer is associated with age-related decline in thymopoiesis (32). *In vitro* development of T cells from stem cells would be useful not only for thymopoiesis studies but also for the advancement of immunotherapies that enable reconstitution of T cells in the context of diseases (34, 35). Primary thymus consists of a complex, multi-cellular microenvironment that provides signals to thymocytes to undergo key developmental checkpoints. The complexity of thymic tissue is difficult to recapitulate *in vitro,* although breakthrough *in vitro* models have revealed that stroma expressing Notch ligands are necessary for supporting T cell development (5, 46). Standard *in vitro* models show several limitations in terms of efficiency and mature T cell production (45). While targeting metabolism has gained traction as a method for boosting immune cell function and manipulating *in vitro* differentiation conditions (51), metabolic studies on the entire breadth of T cell developmental stages are lacking, particularly in human thymus and *in vitro* systems.

Here, we describe the development of the mouse artificial thymic organoid (M-ATO) that produces thymocyte developmental populations phenotypically identical and transcriptionally similar to those seen in primary mouse thymus. Unlike previous mouse *in vitro* systems, the M-ATO is a 3D structure grown in serum-free media in which HSPCs derived from adult bone marrow are aggregated with an MS5 supportive stromal cell-line expressing Notch ligands. Whereas previous monolayer mouse co-culture models of *in vitro* T cell differentiation primarily produce SP8 T cells and not SP4 T cells, we show that, in addition to mature SP8 T cells, the M-ATO even generates mature SP4 T cells including a rare population of cells with a Treg phenotype. Moreover, M-ATO-derived SP8 and SP4 T cells express a diverse TCR Vβ repertoire

and proliferate and produce cytokines when activated. M-ATOs initiated with isolated HSCs or increasingly committed lymphoid progenitors from bone marrow or thymus tissue faithfully captured expected T cell differentiation kinetics; for example, HSCs revealed the slowest while DN3 thymocytes revealed the fastest differentiation into mature T cells. Most remarkably, adult bone marrow-derived single HSCs cultured in M-ATOs were able to efficiently generate the complete trajectory of T cell differentiation and a broad TCR repertoire, which has also not been shown before in previous mouse models. Thus, the M-ATO system we developed is a simple, efficient, reproducible, and promising platform to study the full range of murine T cell maturation from various or even single purified HSPC clones.

The 3D structure of the ATO model may provide more optimal interactions between MHC class II-expressing cells and T cell precursors, as other 3D systems (FTOC) allow positive selection and T cell maturation of SP4 T cells (44, 115-117). Previous monolayer mouse co-cultures may not have permitted the production of SP4 T cells possibly due to lack of MHC Class II expression or inefficient TCR-MHC interactions. The 3D structure may also allow maturing T cells to migrate away from Notch ligand-expression stroma, which is normally seen during *in vivo* thymopoiesis in the cortical-medullary thymic architecture. However, SP8 T cells are still more predominant in the M-ATO culture compared to SP4 T cells. Future work in the lab will further improve T cell maturation in both the mouse and human ATO systems.

We also now report the first comparative analysis of metabolic dynamics during human and murine thymopoiesis *in vivo* and *in vitro* through comprehensive integration of transcriptomics and metabolic flux data. We demonstrate that metabolism during T cell development is largely conserved between species and *in vitro.* Thymocytes prior to the DP stage show the highest glycolytic and OXPHOS activity. At the DP early stage, glycolysis and

mitochondrial respiration are invariably reduced in mouse thymus, human thymus, mouse ATO and even human ATO. Metabolic transcriptional profiles generally reflect functional metabolic activity; except for the uncoordinated ETC gene expression in the human ATO. Lastly, while loss of RAG-mediated TCR rearrangement had a deleterious impact on DN cell metabolism, the downregulation of glycolytic and OXPHOS activity at the DP stage occurred regardless; suggesting that this metabolic downregulation in DP early cells is independent of TCR-mediated signaling.

The fidelity of thymocyte metabolic dynamics *in vitro* is impressive, considering the differences in the microenvironment, such as gas exchange, supportive tissue, and nutrient availability. Our findings suggest, with the exception of Notch signaling, key metabolic changes during T cell development do not require the complex architecture of the primary thymus. There were still some metabolic differences between *in vivo* and *in vitro* systems. Mainly, human ATO cells showed poor coordination between respiratory metabolism and ETC gene expression. The discrepancy between mitochondrial gene expression and activity may be due to additional regulatory mechanisms, including post-translational processes, controlling mitochondrial metabolism. The uncoordinated mitochondrial gene expression in the human ATO system also uncovers an opportunity to further improve the human ATO system.

It remains unclear what mechanisms are controlling these highly conserved metabolic shifts. Notch signaling during T cell development is recapitulated in the ATO system and is consistently associated with key metabolic shifts. Notch signaling has been shown in the mouse system to be required for DN3 cells to upregulate glucose receptors after beta selection (60). Other potential mechanisms, such as cytokine signaling suppression at the DP stage, have been hypothesized to prevent external signals from allowing DP cells to survive when most are

supposed to die from neglect if they lack a functional TCR (140). Future studies are required to investigate the mechanisms controlling the tightly conserved metabolic changes in both mouse and human thymopoiesis, and whether these thymocyte metabolic changes are perturbed in the context of aging or other diseases.

In conclusion, we report advancements in mouse *in vitro* T cell differentiation models and T cell development metabolic studies. Notably, the M-ATO system we generated shows unprecedented robust differentiation from a single HSC as well as the ability to generate SP4 T cells, including Tregs. We have also performed the first comprehensive metabolic studies on the entirety of thymic T cell development. Combining transcriptomics and metabolic assays, we have revealed dramatic metabolic transitions between key thymocyte stages that are highly conserved between human and mouse species. Despite the lack of a complex thymic microenvironment, the metabolic pattern was even conserved *in vitro,* specifically in the mouse and human ATO systems. The ATO systems are therefore robust models that recapitulate critical metabolic transitions during human and murine thymopoiesis. Thus, our work has propelled the thymopoiesis field's arsenal of highly reliable *in vitro* platforms and uncovered the strikingly controlled metabolic landscape during T cell development across species and systems.

APPENDICES

Chapter 2 Supplemental Materials

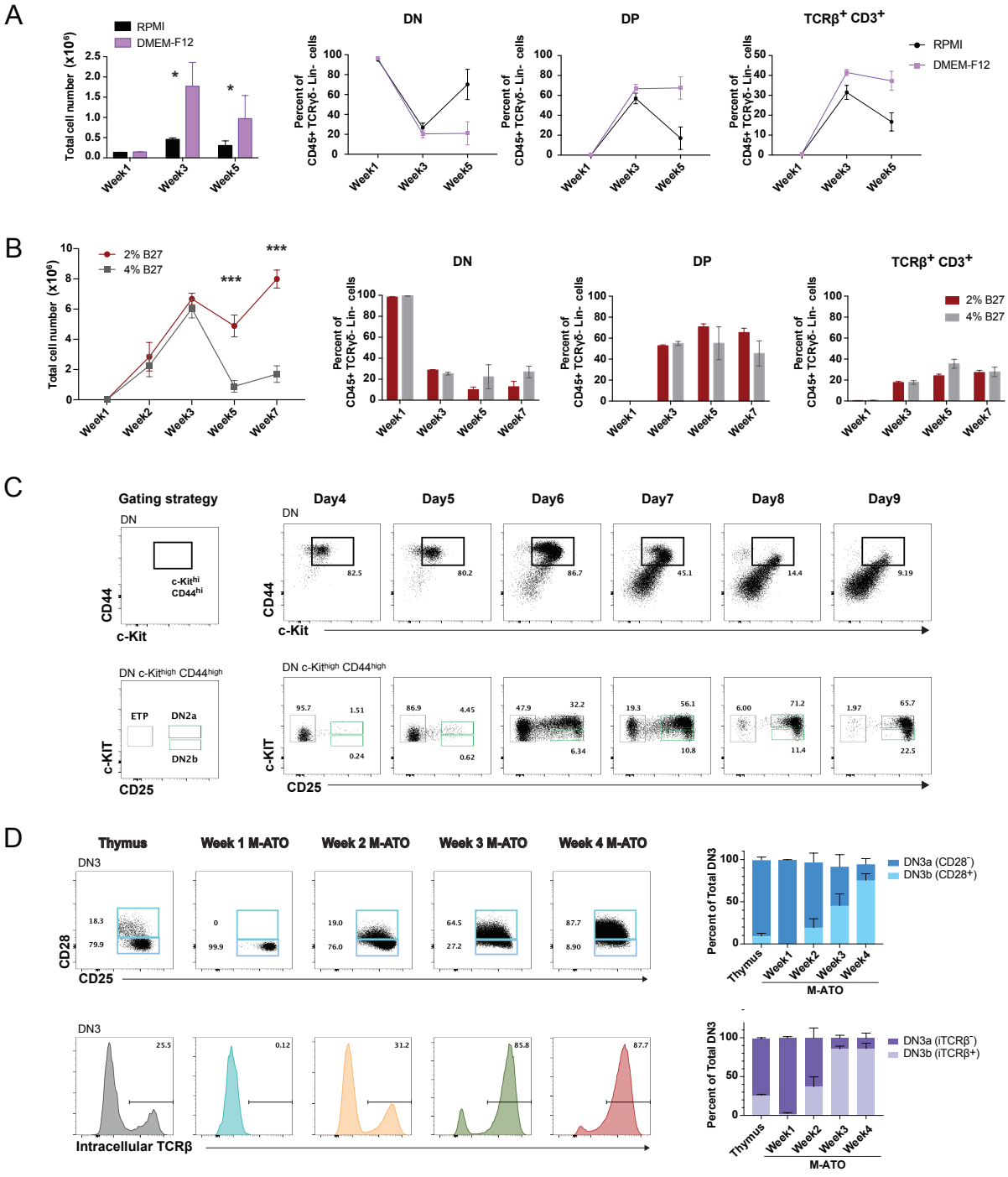

Figure S2-1 (related to Figure 2-1): T cell development in M-ATOs

(**A**) Comparison of T cell differentiation in M-ATOs using either RPMI 1640 (black) or DMEM-F12 (pink) as basal medium. Fold expansion of cells (left) and frequencies of different T cell populations (right) are shown. Error bars: +/- SD (n=3 independent experiments, significance: unpaired t-test *$p<0.05$).

(**B**) Comparison of T cell differentiation in M-ATOs using either 2% (red) or 4% (grey) of B27 supplement. Cell numbers (left) and frequencies of different T cell populations (right) are shown. Error bars: +/- SD (n=3 independent experiments, significance: unpaired t-test ***$p<0.001$).

(**C**) Kinetic analysis of early T cell development (ETP, DN2a and DN2b) in M-ATOs during the first 9 days of culture. Gating strategy is shown on the left. Cells are gated on the DN population (top row) and subgated on $CD44^{high}$ and $c\text{-}kit^{high}$ cells (bottom row): (ETP) ($c\text{-}kit^{hi}$, $CD44^{hi}CD25^{-}$), DN2a ($ckit^{hi}$, $CD44^{hi}CD25^{+}$), DN2b ($ckit^{hi}$, $CD44^{dim}CD25^{+}$). Data is representative of 3 independent experiments.

(**D**) Frequency of DN3a ($CD28^{-}$ or $iTCR\beta^{-}$) and DN3b ($CD28^{+}$ or $iTCR\beta^{+}$) cells within the DN3 population in the thymus and over the course of M-ATO development in FVB mice. Error bars: +/- SD (n=3 independent experiments).

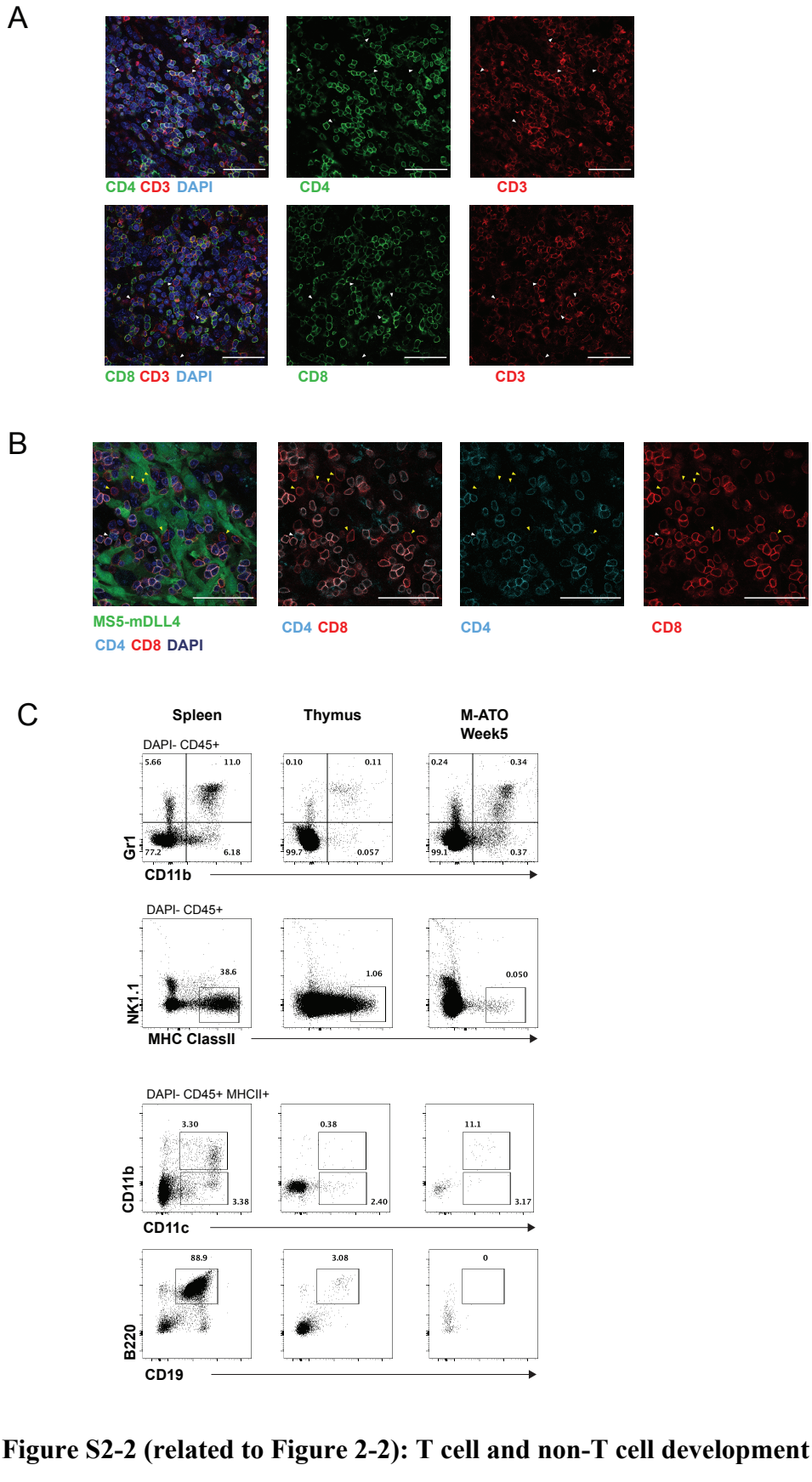

Figure S2-2 (related to Figure 2-2): T cell and non-T cell development in M-ATOs

(**A-B**) Immunofluorescence analysis in M-ATOs from LSK isolated from C57BL/6 WT mice representative of 3 independent experiments. Nuclei were stained with DAPI (dark blue). Scale bars, 50μm. (**A**) CD4 (green) and CD3 (red) expression (top); and CD8 (green) and CD3 (red) (bottom) in week 4 M-ATOs. White arrowhead represents CD3+CD8- or CD3+CD4- cells. (**B**) MS5-mDll4 GFP^+ stroma (green), CD4 (cyan), CD8 (red) expression in week 6 M-ATOs. White arrowhead represents CD8-CD4+ cells; yellow arrowhead represents CD8+CD4- cells.
(**C**) Representative flow cytometry analysis of non-T lineage markers in spleen, thymus, and week 5 M-ATOs from C57BL/6 WT mice.

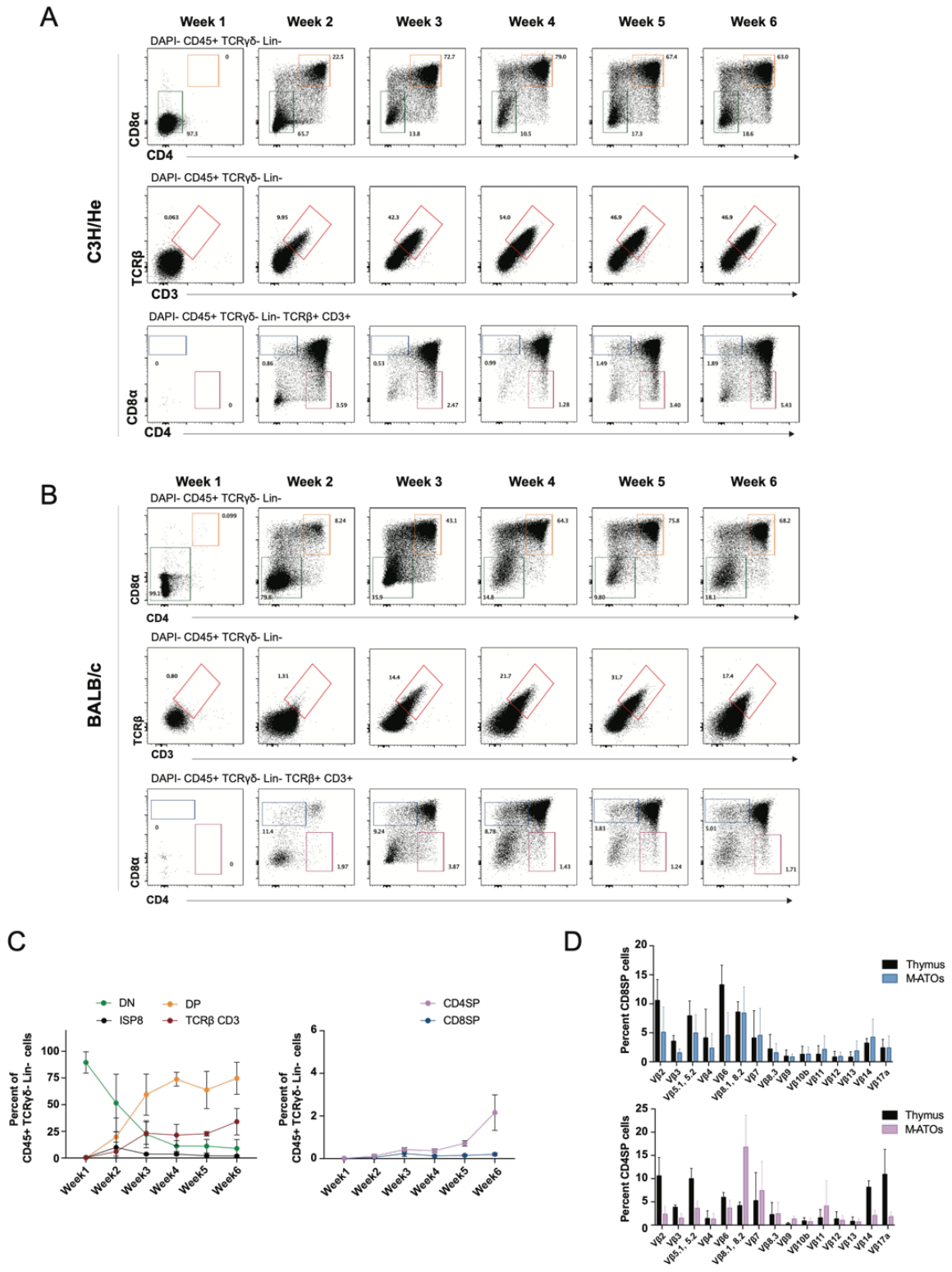

Figure S2-3 (related to Figure 2-3): T cell development in M-ATO using bone marrow from different murine genetic strains

(**A-B**) Representative kinetic analysis of T cell development in M-ATOs from LSK isolated from C3H/He mice (**A**), BALB/c mice (**B**) at the indicated time points gated on $CD45^+$ $TCR\gamma\delta^-$ Lin^- cells. Bottom row shows CD4 and CD8 expression gated on $CD3^+TCR\beta^+$ cells. Data is representative of 3 biological replicates.

(**C**) Frequencies of the different T cell populations generated in M-ATOs from LSK from the FVB background shown as percent of total $CD45^+$ $TCR\gamma\delta^-$ Lin^- cells over time. Error bars: +/-SD (n=4 independent experiments). (**D**) TCR diversity in $CD3^+CD8SP$ (top) and $CD3^+CD4SP$ (bottom) T cells from week 6 M-ATOs from LSK isolated from FVB mice. Error bar: +/-SD: FVB thymus n=4, FVB M-ATO n=4 independent experiments.

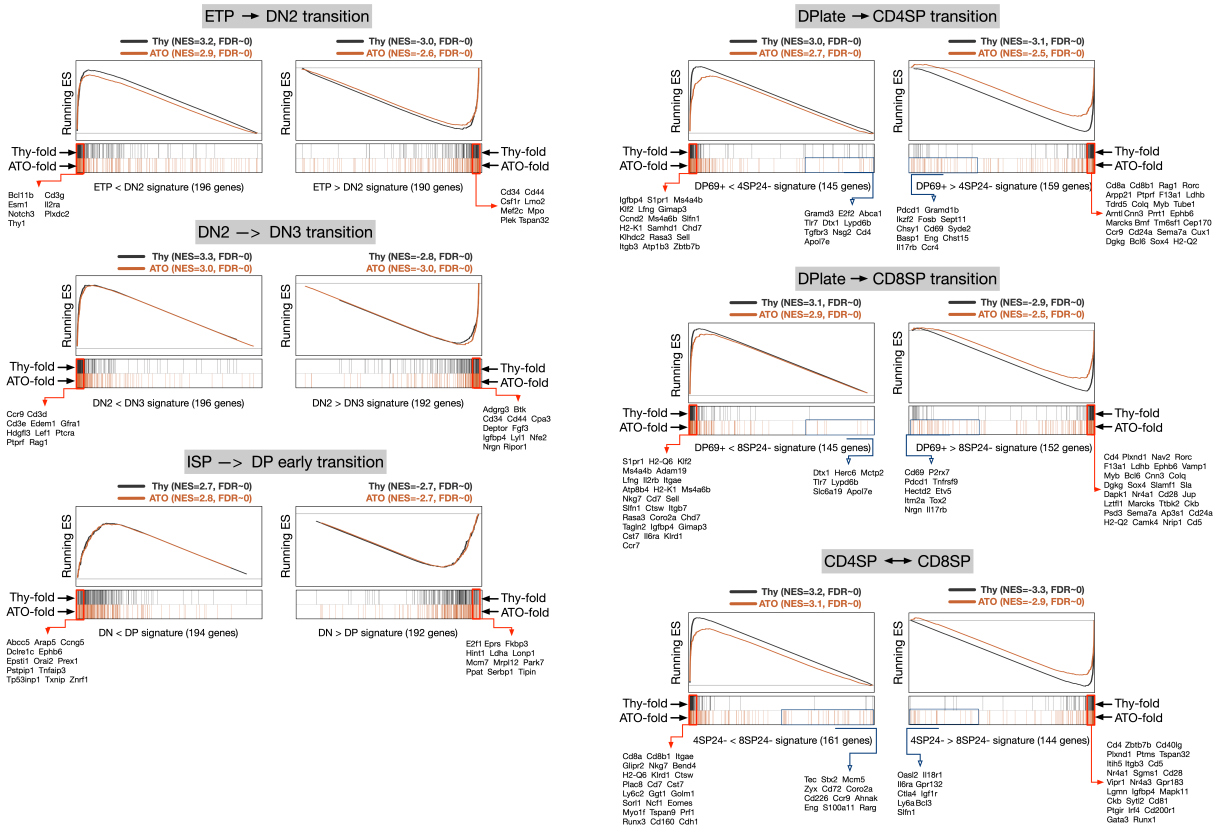

Figure S2-4 (related to Figure 2-4): Gene set enrichment analyses (GSEA) of reference T-cell gene signatures in M-ATO-derived and thymic populations.

For each two-population analysis, the x axis represents the pre-ranked list of genes based on fold changes between the two populations from either thymic (*Thy-fold, black*) or M-ATO-derived (*ATO-fold, orange*) cells. For instance, for the ETP/DN2 transition, genes highly up-regulated in DN2 cells are positioned to the left. Segment plots (bottom) highlight the position of genes from independent reference signatures (e.g., ETP<DN2 signature) in the sorted vector of fold changes from our samples. The vertical axis in line plots (top) represents the cumulative Enrichment Score (ES) from GSEA, and NES is the overall normalized enrichment score (with FDR=false discovery rate). Details on the external signatures employed for each transition are provided in Methods.

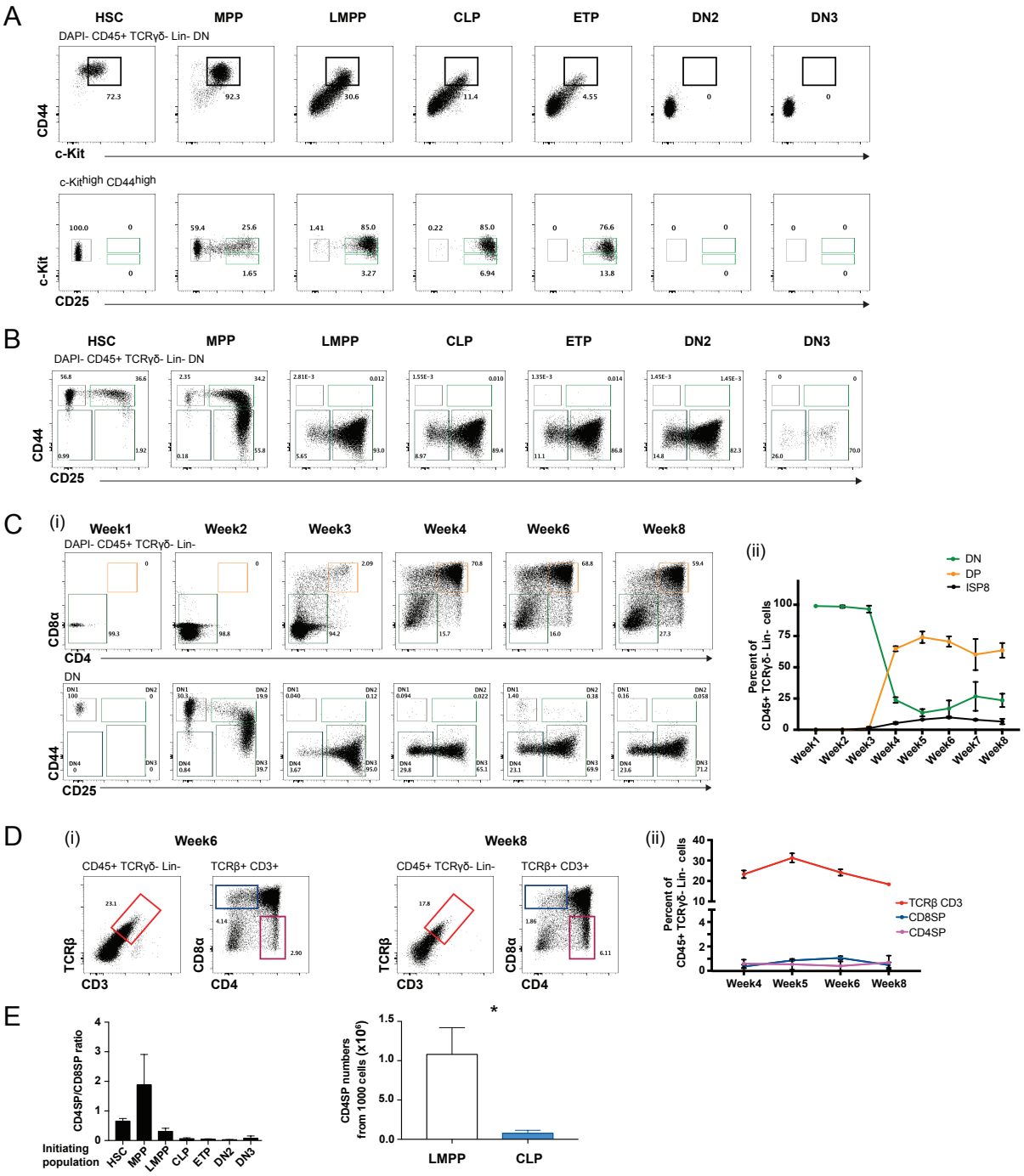

Figure S2-5 (related to Figure 2-6): T cell development in M-ATO from different hematopoietic subsets.

(**A-B**) Representative analysis of (**A**) early T cell development (ETP, DN2a and DN2b) in week 1 M-ATOs and (**B**) the DN population in week 2 M-ATOs initiated with the different hematopoietic

subsets shown above each graph. Cells are gated on the DN population (top row) and subgated on $CD44^{high}$ and $c\text{-}kit^{high}$ cells (bottom row): (ETP) ($c\text{-}kit^{hi}$, $CD44^{hi}CD25^{-}$) (left gate), DN2a ($ckit^{hi}$, $CD44^{hi}CD25^{+}$), DN2b ($ckit^{hi}$, $CD44^{dim}CD25^{+}$). Data are representative of 3 biological replicates.

(**C-D**) Representative kinetic analysis of (**C**) early T cell development and (**D**) mature T cell differentiation in M-ATOs from purified HSCs (LSK $CD48^{-}CD150^{+}$) cells at the indicated time points (**i**). Line graphs (**ii**) show summary of (**C**) DN, DP, ISP8 population frequencies and (**D**) $TCR\beta^{+}CD3^{+}$, CD8SP, CD4SP population frequencies as percent of total $CD45^{+}$ $TCR\gamma\delta^{-}$ Lin^{-} cells. Error Bars: +/-SD (n=3 independent experiments).

(**E**) Analysis of the frequencies of CD4SP and CD8SP cells generated from different hematopoietic subsets (as indicated) at week 6. Ratios between frequencies of CD4SP cells versus CD8SP cells are shown for all hematopoietic subsets (left graph). Right graph shows the comparison of absolute CD4SP cell numbers generated from 1000 LMPP or CLP in M-ATOs. Error bars: +/- SEM (n=3 independent experiments, Significance: unpaired t-tests *$p<0.05$).

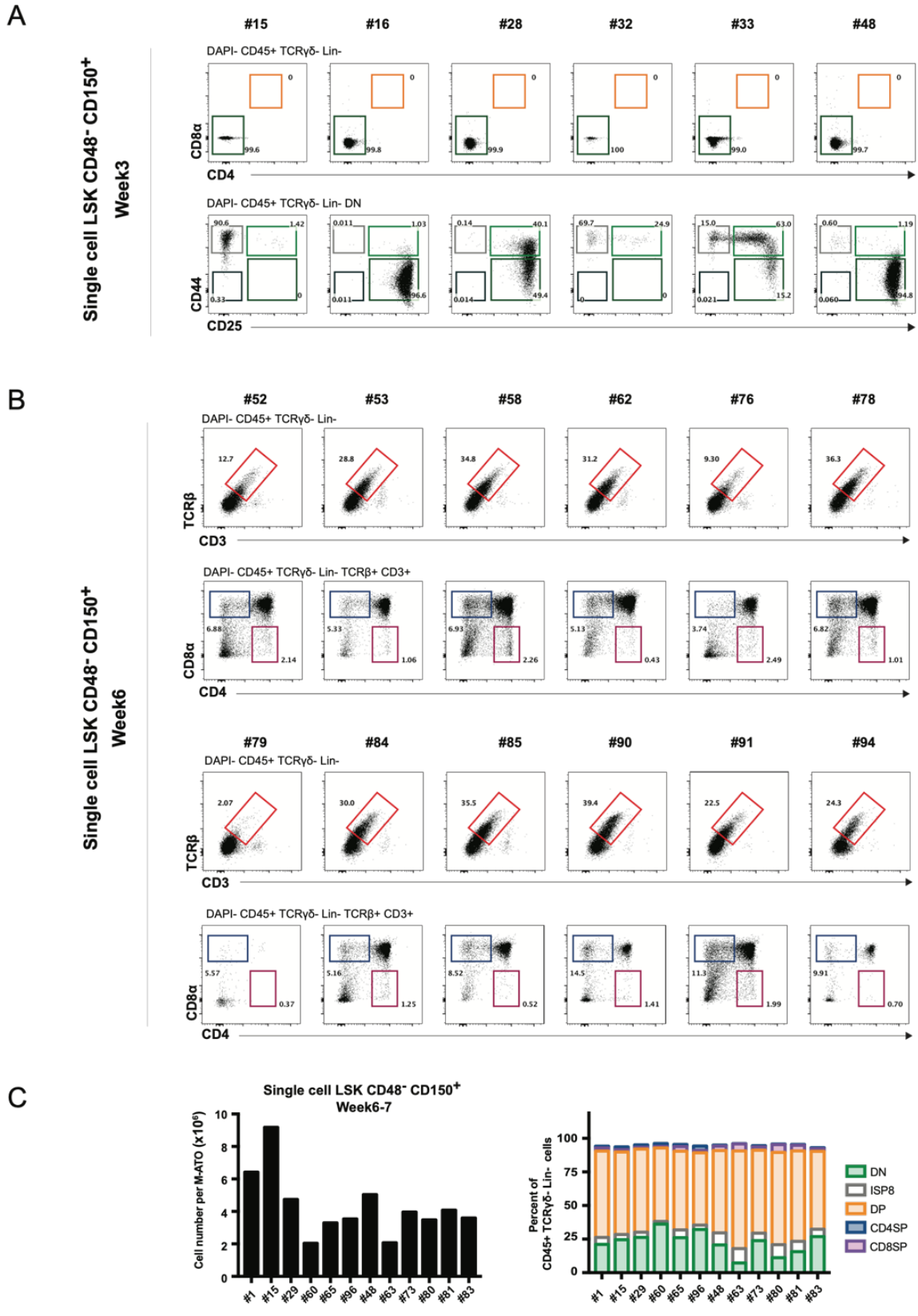

Figure S2-6 (related to Figure 2-7): T cell development in M-ATO from single HSCs

(**A-B**) Flow cytometry analysis of week 3 (**A**) and week 6 (**B**) M-ATOs, each initiated with a single HSC (LSK $CD48^{-}CD150^{+}$). Clone numbers are shown above each graph. (**C**) Cell numbers (left) and phenotype (right) in week 6-7 M-ATOs initially seeded with a single (LSK $CD48^{-}CD150^{+}$) HSC cell. 12 independent M-ATOs are shown from an experiment independent of the one shown in Figure 7D

Table S2-1 (related to Figure 2-4 and Figure S2-4): Differential and Functional Analyses of RNA Sequencing Data

See excel file under Supplemental Information at https://www.cell.com/cell-reports/fulltext/S2211-1247(20)31309-7.

Chapter 3 Supplemental Materials

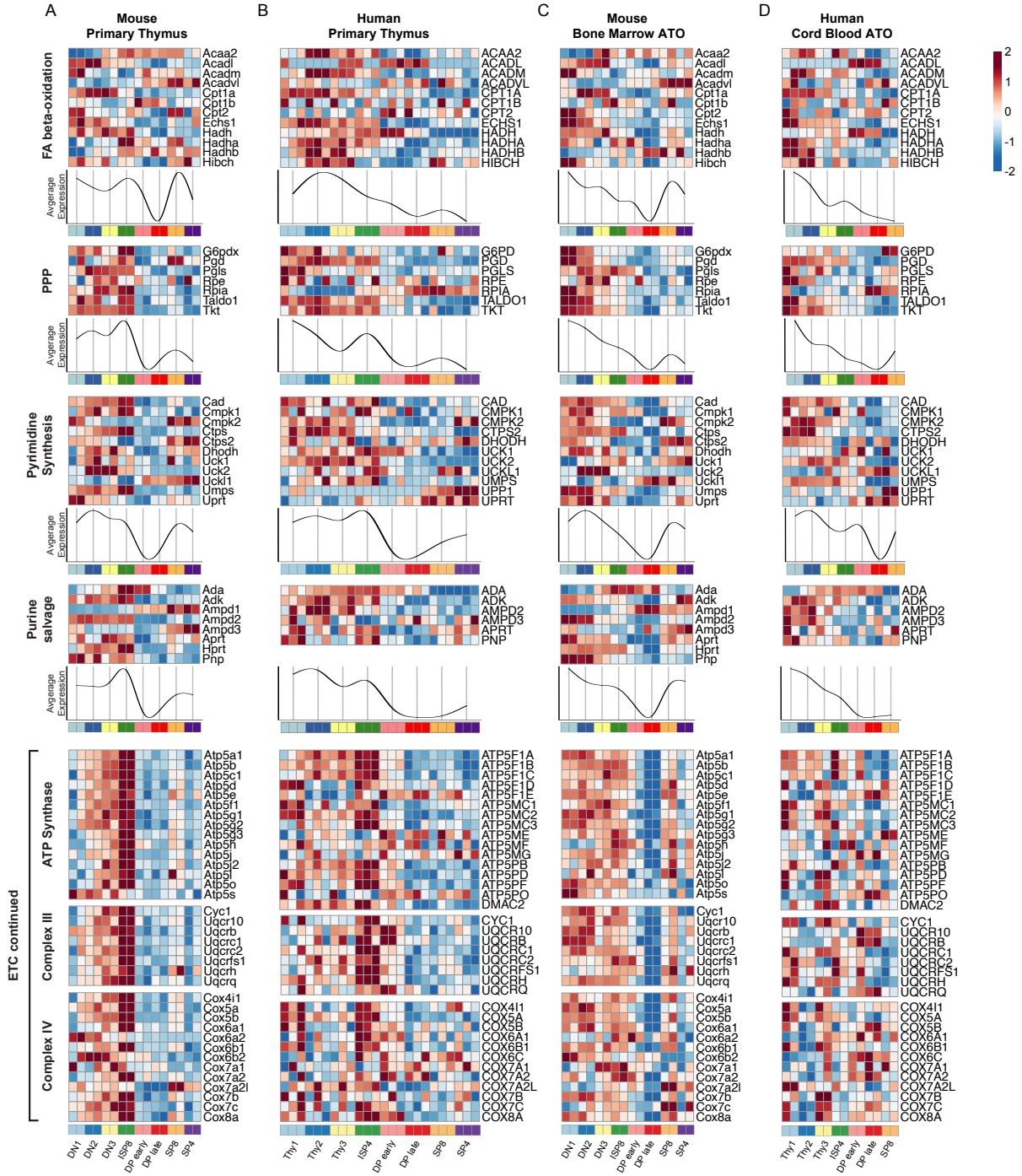

Figure S3-1 (related to Figure 3-3): Metabolic gene expression profiles in thymic and *in vitro* murine and human thymopoiesis

(**A-D**) Summary heatmaps and line plots of additional metabolic pathways (fatty acid beta-oxidation, pentose phosphate pathway, and nucleotide metabolism) and additional electron transport chain complexes in (**A**) M-THY, (**B**) H-THY, (**C**) M-ATO, and (**D**) H-ATO. The x axis indicates cell types isolated for analysis. Each individual heatmap represents *z*-scores of normalized variance-stabilized gene expression data. Line plots represent the average *z*-score for all genes in the heatmap. (n=2 independent replicates per population in M-THY; n=3 in H-THY; n=2 in M-ATO; n=2 in H-ATO)

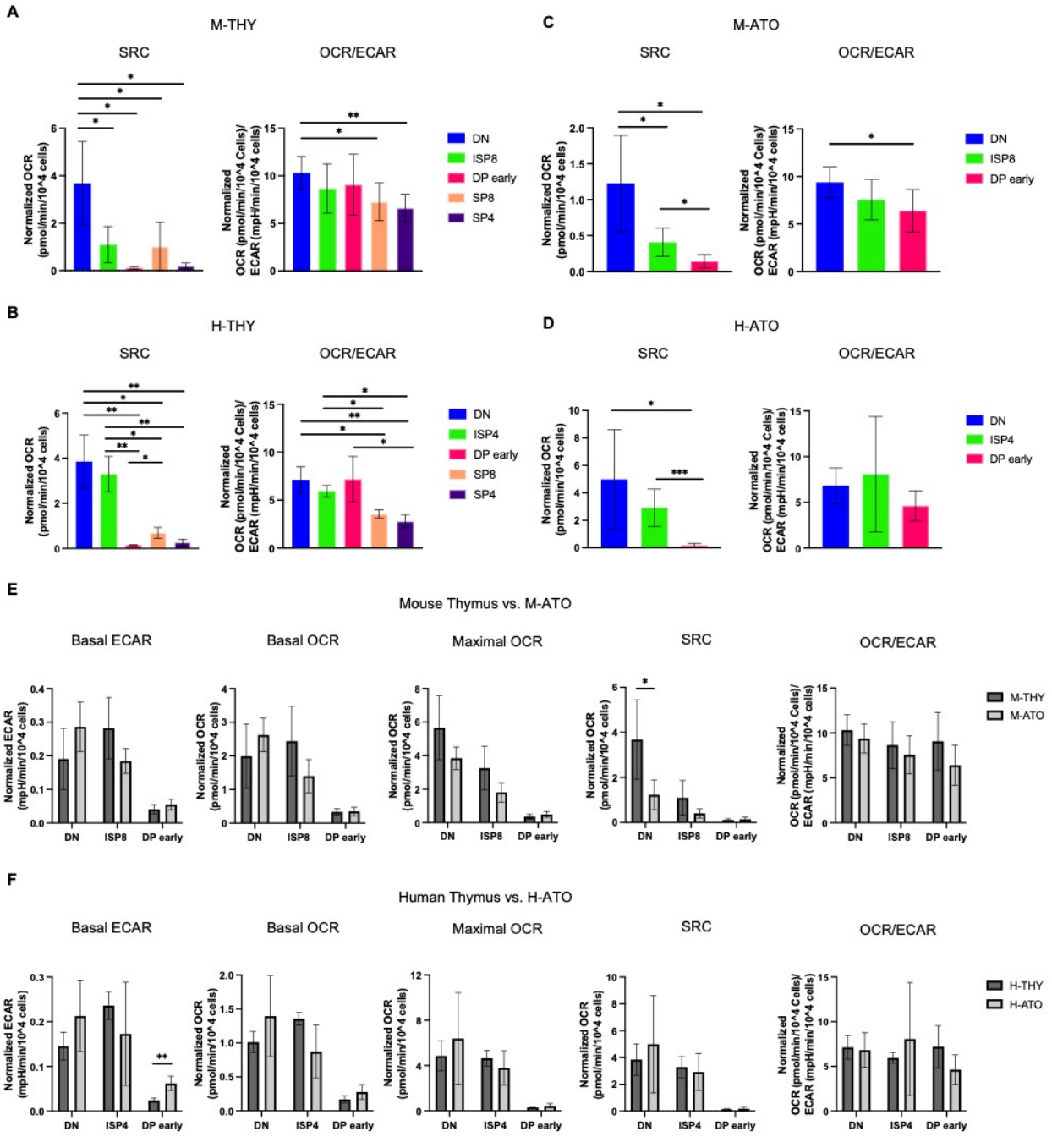

Figure S3-2 (related to Figure 3-4): Primary and *in vitro*-derived thymocytes exhibit similar metabolic activity

(**A-D**) SRC and OCR/ECAR ratio in thymocyte populations from (**A**) M-THY, (**B**) H-THY, (**C**) M-ATO, and (**D**) H-ATO. Measurements are normalized to cell number per well. (n=6

independent experiments in M-THY; n=6 MATO; n=3 H-THY [except for ISP4: n=2]; n=6 H-ATO [except for ISP4: n=5])

(**E**) Extracellular flux measurements are compared between M-THY and M-ATO. (n=6 independent experiments in M-THY; n=6 MATO)

(error bars: sd, significance: multiple t-test p values * $p < 0.05$; ** $p < 0.01$, *** $P < 0.001$)

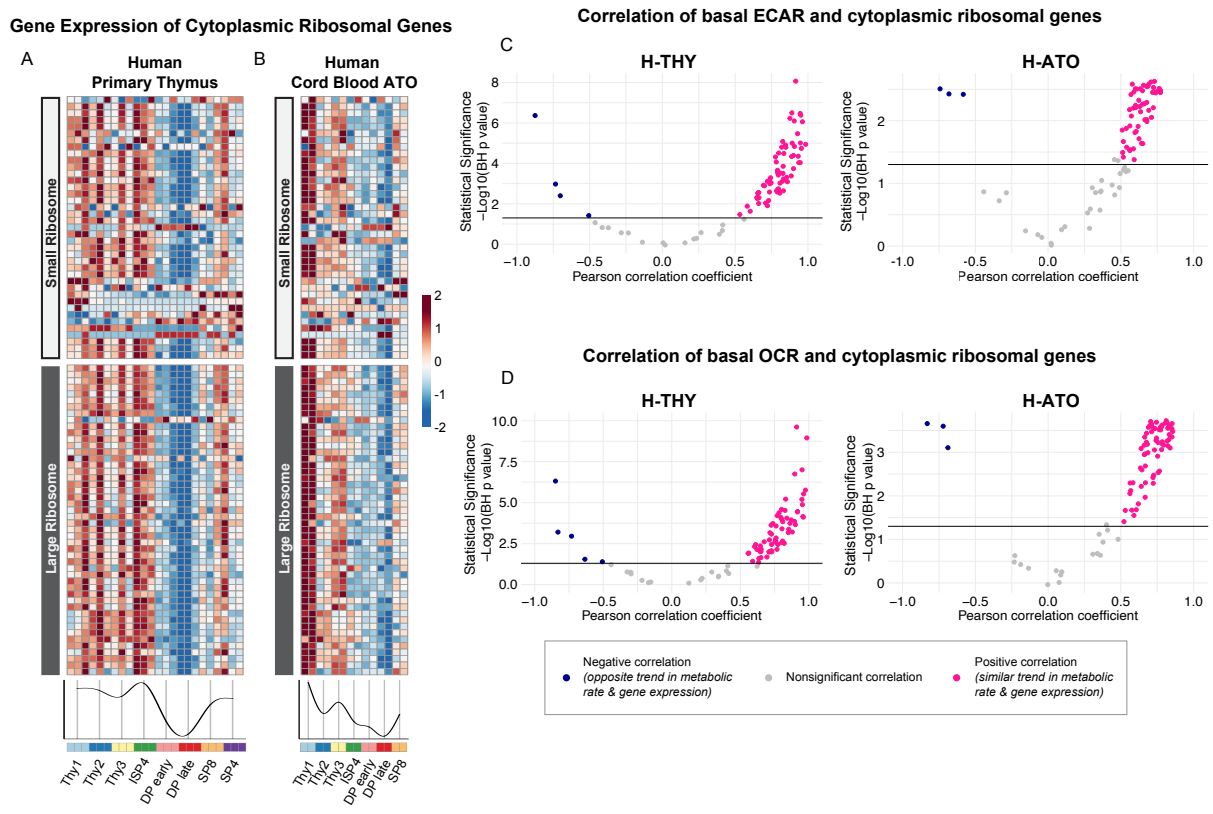

Figure S3-3 (Related to Figure 3-6): Correlation between structural ribosome gene expression and extracellular flux data in human thymocytes

(**A-B**) Summary heatmaps and line plots of cytoplasmic ribosomal genes (small and large ribosome) in (**A**) H-THY and (**B**) H-ATO. The x axis indicates cells isolated for analysis. Each individual heatmap represents *z*-scores of normalized variance-stabilized gene expression data. Line plots represent the average *z*-score for all genes in the heatmap. (n=3 in H-THY; n=2 in H-ATO)

(**C-D**) Scatter plots show correlation between (**C**) small/large cytoplasmic ribosomal genes and basal glycolysis (ECAR) or (**D**) small/large cytoplasmic ribosomal genes and basal respiration (OCR) in the H-THY (left) or H-ATO (right). The x axis represents the Pearson correlation coefficient R values calculated for individual genes within the specified metabolic pathway for all thymocyte populations for which respective extracellular flux data was collected. The y axis

represents the statistical significance of each R value using -log10 of Benjamini-Hochberg adjusted p-values. Solid black line indicates an adjusted p-value of 0.05; all R values above the line are statistically significant. Genes with R values >0.5 (pink) are positively correlated with metabolic flux data, while genes with R values <-0.5 (blue) are negatively correlated with metabolic flux data. Nonsignificant or weak correlation R values >-.05 or <0.5 are indicated in grey. (H-THY: n=3 flux analysis values for 5 populations [except for ISP4: n=2], n=3 RNA-seq replicates; H-ATO: n=6 flux analysis values for 3 populations [except for ISP4: n=5], n=2 RNA-seq replicates)

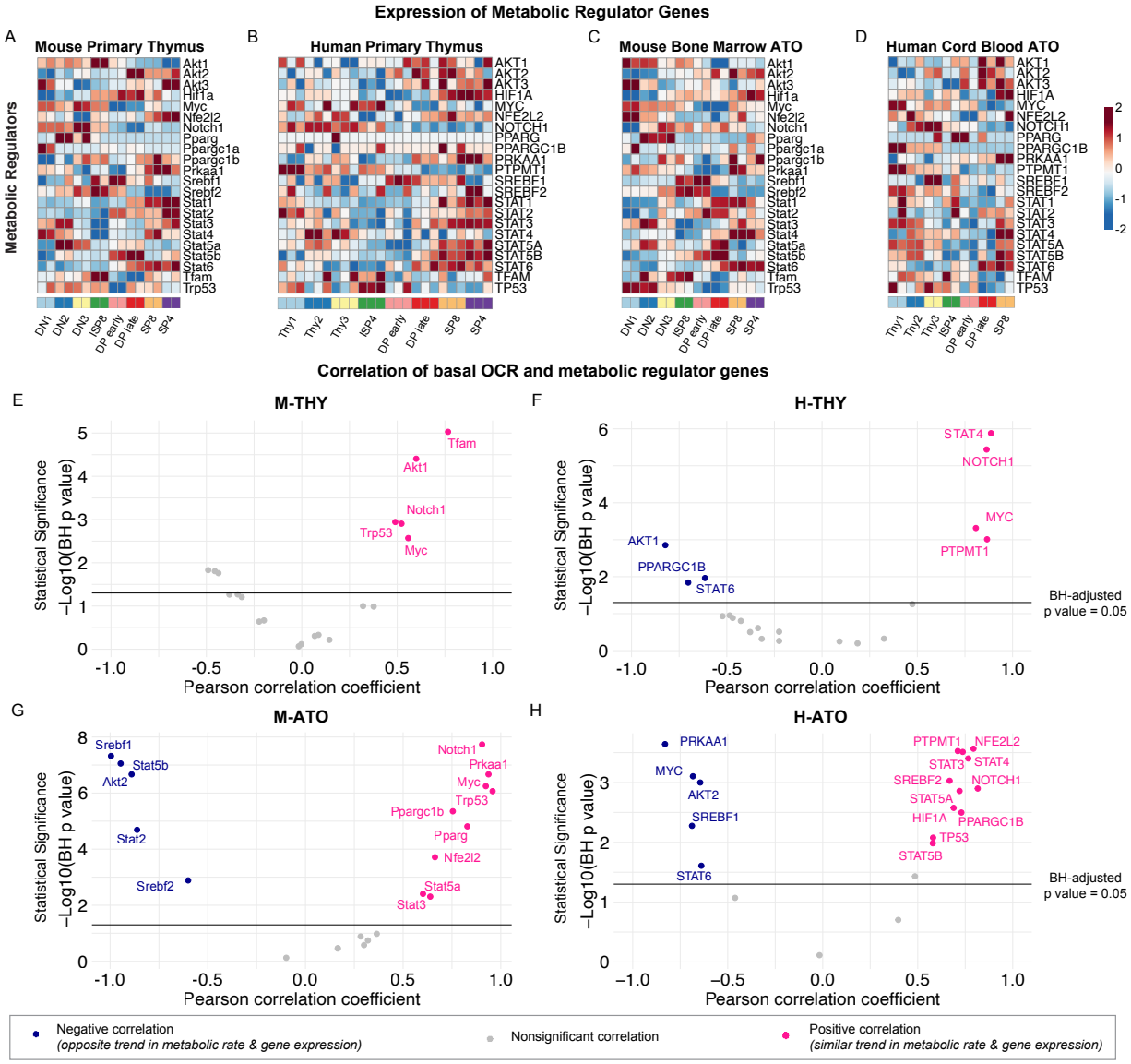

Figure S3-4 (related to Figure 3-6): Correlation between gene expression of metabolic regulators and extracellular flux data in murine and human thymocytes

(**A-D**) Heatmaps and summary line plots of genes encoding key signaling molecules and transcription factors that regulate metabolic programs in (**A**) M-THY, (**B**) H-THY, (**C**) M-ATO, and (**D**) H-ATO. The x axis indicates cell populations isolated for analysis. Each individual heatmap represents *z*-scores of normalized variance-stabilized gene expression data. (n=2

independent replicates per population in M-THY; n=3 in H-THY; n=2 in M-ATO; n=2 in H-ATO).

(**E-H**) Scatter plots show correlation between gene expression of metabolic regulators and basal respiration (OCR) in (**E**) M-THY, (**F**) H-THY, (**G**) M-ATO, and (**H**) H-ATO. The x axis represents the Pearson correlation coefficient R values calculated for individual genes within the specified metabolic pathway for all thymocyte populations for which respective extracellular flux data was collected. The y axis represents the statistical significance of each R value using -log10 of Benjamini-Hochberg adjusted p-values. Solid black line indicates an adjusted p-value of 0.05; all R values above the line are statistically significant. Genes with R values >0.5 (pink) are positively correlated with metabolic flux data, while genes with R values <-0.5 (blue) are negatively correlated with metabolic flux data. Nonsignificant or weak correlation R values >-.05 or <0.5 are indicated in grey. (M-THY: n=6 flux analysis values for 5 populations, n=2 RNA-seq replicates; H-THY: n=3 flux analysis values for 5 populations [except for ISP4: n=2], n=3 RNA-seq replicates; M-ATO: n=6 flux analysis values for 3 populations, n=2 RNA-seq replicates; H-ATO: n=6 flux analysis values for 3 populations [except for ISP4: n=5], n=2 RNA-seq replicates)

Table S3-1 (related to Figure 3-1): Population phenotypes for RNA-seq and Seahorse Assay Analyses

See excel file under Supplemental Information.

Table S3-2 (related to Figure 3-2B): Differentially expressed genes in human thymus and ATO RNA-seq dataset listed in order of appearance
See excel file under Supplemental Information.

Table S3-3 (related to Figure 3-5, Figure 3-6, Figure S3-3, and Figure S3-4): Results from correlation analyses between extracellular flux and transcriptional data in mouse and human thymocytes

See excel file under Supplemental Information.

Bibliography

1. Porritt HE, Rumfelt LL, Tabrizifard S, Schmitt TM, Zuniga-Pflucker JC, Petrie HT. Heterogeneity among DN1 prothymocytes reveals multiple progenitors with different capacities to generate T cell and non-T cell lineages. Immunity. 2004;20(6):735-45.

2. Ghaedi M, Steer CA, Martinez-Gonzalez I, Halim TYF, Abraham N, Takei F. Common-Lymphoid-Progenitor-Independent Pathways of Innate and T Lymphocyte Development. Cell Rep. 2016;15(3):471-80.

3. Harman BC, Jenkinson EJ, Anderson G. Entry into the thymic microenvironment triggers Notch activation in the earliest migrant T cell progenitors. J Immunol. 2003;170(3):1299-303.

4. Heinzel K, Benz C, Martins VC, Haidl ID, Bleul CC. Bone marrow-derived hemopoietic precursors commit to the T cell lineage only after arrival in the thymic microenvironment. J Immunol. 2007;178(2):858-68.

5. Schmitt TM, Ciofani M, Petrie HT, Zuniga-Pflucker JC. Maintenance of T cell specification and differentiation requires recurrent notch receptor-ligand interactions. J Exp Med. 2004;200(4):469-79.

6. Hozumi K, Mailhos C, Negishi N, Hirano K, Yahata T, Ando K, et al. Delta-like 4 is indispensable in thymic environment specific for T cell development. J Exp Med. 2008;205(11):2507-13.

7. Breed ER, Lee ST, Hogquist KA. Directing T cell fate: How thymic antigen presenting cells coordinate thymocyte selection. Semin Cell Dev Biol. 2018;84:2-10.

8. Rothenberg EV, Moore JE, Yui MA. Launching the T-cell-lineage developmental programme. Nat Rev Immunol. 2008;8(1):9-21.

9. Takahama Y. Journey through the thymus: stromal guides for T-cell development and selection. Nat Rev Immunol. 2006;6(2):127-35.

10. Godfrey DI, Kennedy J, Suda T, Zlotnik A. A developmental pathway involving four phenotypically and functionally distinct subsets of CD3-CD4-CD8- triple-negative adult mouse thymocytes defined by CD44 and CD25 expression. J Immunol. 1993;150(10):4244-52.

11. Bell JJ, Bhandoola A. The earliest thymic progenitors for T cells possess myeloid lineage potential. Nature. 2008;452(7188):764-7.

12. Yui MA, Feng N, Rothenberg EV. Fine-scale staging of T cell lineage commitment in adult mouse thymus. J Immunol. 2010;185(1):284-93.

13. Krangel MS. Mechanics of T cell receptor gene rearrangement. Curr Opin Immunol. 2009;21(2):133-9.

14. Yannoutsos N, Wilson P, Yu W, Chen HT, Nussenzweig A, Petrie H, et al. The role of recombination activating gene (RAG) reinduction in thymocyte development in vivo. J Exp Med. 2001;194(4):471-80.

15. Eberl G, Colonna M, Di Santo JP, McKenzie AN. Innate lymphoid cells. Innate lymphoid cells: a new paradigm in immunology. Science. 2015;348(6237):aaa6566.

16. Shin SB, McNagny KM. ILC-You in the Thymus: A Fresh Look at Innate Lymphoid Cell Development. Front Immunol. 2021;12:681110.

17. Carpenter AC, Bosselut R. Decision checkpoints in the thymus. Nat Immunol. 2010;11(8):666-73.

18. Fehling HJ, Krotkova A, Saint-Ruf C, von Boehmer H. Crucial role of the pre-T-cell receptor alpha gene in development of alpha beta but not gamma delta T cells. Nature. 1995;375(6534):795-8.

19. Gegonne A, Chen QR, Dey A, Etzensperger R, Tai X, Singer A, et al. Immature CD8 Single-Positive Thymocytes Are a Molecularly Distinct Subpopulation, Selectively Dependent on BRD4 for Their Differentiation. Cell Rep. 2018;24(1):117-29.

20. Casero D, Sandoval S, Seet CS, Scholes J, Zhu Y, Ha VL, et al. Long non-coding RNA profiling of human lymphoid progenitor cells reveals transcriptional divergence of B cell and T cell lineages. Nat Immunol. 2015;16(12):1282-91.

21. Takeuchi Y, Fujii Y, Okumura M, Inada K, Nakahara K, Matsuda H. Characterization of CD4+ single positive cells that lack CD3 in the human thymus. Cell Immunol. 1993;151(2):481-90.

22. Parekh C, Crooks GM. Critical differences in hematopoiesis and lymphoid development between humans and mice. J Clin Immunol. 2013;33(4):711-5.

23. Blom B, Verschuren MC, Heemskerk MH, Bakker AQ, van Gastel-Mol EJ, Wolvers-Tettero IL, et al. TCR gene rearrangements and expression of the pre-T cell receptor complex during human T-cell differentiation. Blood. 1999;93(9):3033-43.

24. Taghon T, Van de Walle I, De Smet G, De Smedt M, Leclercq G, Vandekerckhove B, et al. Notch signaling is required for proliferation but not for differentiation at a well-defined beta-selection checkpoint during human T-cell development. Blood. 2009;113(14):3254-63.

25. Dietrich J, Neisig A, Hou X, Wegener AM, Gajhede M, Geisler C. Role of CD3 gamma in T cell receptor assembly. J Cell Biol. 1996;132(3):299-310.

26. Georgiev H, Peng C, Huggins MA, Jameson SC, Hogquist KA. Classical MHC expression by DP thymocytes impairs the selection of non-classical MHC restricted innate-like T cells. Nat Commun. 2021;12(1):2308.

27. Klein L, Kyewski B, Allen PM, Hogquist KA. Positive and negative selection of the T cell repertoire: what thymocytes see (and don't see). Nat Rev Immunol. 2014;14(6):377-91.

28. Cosway EJ, James KD, Lucas B, Anderson G, White AJ. The thymus medulla and its control of alphabetaT cell development. Semin Immunopathol. 2021;43(1):15-27.

29. Resop RS, Uittenbogaart CH. Human T-Cell Development and Thymic Egress: An Infectious Disease Perspective. For Immunopathol Dis Therap. 2015;6(1-2):33-49.

30. Sakaguchi S, Yamaguchi T, Nomura T, Ono M. Regulatory T cells and immune tolerance. Cell. 2008;133(5):775-87.

31. Gui J, Mustachio LM, Su DM, Craig RW. Thymus Size and Age-related Thymic Involution: Early Programming, Sexual Dimorphism, Progenitors and Stroma. Aging Dis. 2012;3(3):280-90.

32. Palmer S, Albergante L, Blackburn CC, Newman TJ. Thymic involution and rising disease incidence with age. Proc Natl Acad Sci U S A. 2018;115(8):1883-8.

33. Thomas R, Wang W, Su DM. Contributions of Age-Related Thymic Involution to Immunosenescence and Inflammaging. Immun Ageing. 2020;17:2.

34. Singh J, Zuniga-Pflucker JC. Producing proT cells to promote immunotherapies. Int Immunol. 2018;30(12):541-50.

35. Wraith DC. The Future of Immunotherapy: A 20-Year Perspective. Front Immunol. 2017;8:1668.

36. Salmikangas P, Kinsella N, Chamberlain P. Chimeric Antigen Receptor T-Cells (CAR T-Cells) for Cancer Immunotherapy - Moving Target for Industry? Pharm Res. 2018;35(8):152.

37. van Loenen MM, de Boer R, Amir AL, Hagedoorn RS, Volbeda GL, Willemze R, et al. Mixed T cell receptor dimers harbor potentially harmful neoreactivity. Proc Natl Acad Sci U S A. 2010;107(24):10972-7.

38. Ruella M, Xu J, Barrett DM, Fraietta JA, Reich TJ, Ambrose DE, et al. Induction of resistance to chimeric antigen receptor T cell therapy by transduction of a single leukemic B cell. Nat Med. 2018;24(10):1499-503.

39. Poirot L, Philip B, Schiffer-Mannioui C, Le Clerre D, Chion-Sotinel I, Derniame S, et al. Multiplex Genome-Edited T-cell Manufacturing Platform for "Off-the-Shelf" Adoptive T-cell Immunotherapies. Cancer Res. 2015;75(18):3853-64.

40. Rosenberg SA, Restifo NP. Adoptive cell transfer as personalized immunotherapy for human cancer. Science. 2015;348(6230):62-8.

41. Patel SJ, Yamauchi T, Ito F. Induced Pluripotent Stem Cell-Derived T Cells for Cancer Immunotherapy. Surg Oncol Clin N Am. 2019;28(3):489-504.

42. DeLuca D, Mandel TE, Luckenbach GA, Kennedy MM. Tolerance induction by fusion of fetal thymus lobes in organ culture. J Immunol. 1980;124(4):1821-9.

43. Mandel TE, Kennedy MM. The differentiation of murine thymocytes in vivo and in vitro. Immunology. 1978;35(2):317-31.

44. Plum J, De Smedt M, Defresne MP, Leclercq G, Vandekerckhove B. Human CD34+ fetal liver stem cells differentiate to T cells in a mouse thymic microenvironment. Blood. 1994;84(5):1587-93.

45. Dolens AC, Taghon T. Human T cell development notched up a level. Nat Methods. 2017;14(5):477-8.

46. Schmitt TM, Zuniga-Pflucker JC. Induction of T cell development from hematopoietic progenitor cells by delta-like-1 in vitro. Immunity. 2002;17(6):749-56.

47. Seet CS, He C, Bethune MT, Li S, Chick B, Gschweng EH, et al. Generation of mature T cells from human hematopoietic stem and progenitor cells in artificial thymic organoids. Nat Methods. 2017;14(5):521-30.

48. Montel-Hagen A, Crooks GM. From pluripotent stem cells to T cells. Exp Hematol. 2019;71:24-31.

49. Tatapudy S, Aloisio F, Barber D, Nystul T. Cell fate decisions: emerging roles for metabolic signals and cell morphology. EMBO Rep. 2017;18(12):2105-18.

50. Nagaraj R, Sharpley MS, Chi F, Braas D, Zhou Y, Kim R, et al. Nuclear Localization of Mitochondrial TCA Cycle Enzymes as a Critical Step in Mammalian Zygotic Genome Activation. Cell. 2017;168(1-2):210-23 e11.

51. Buck MD, O'Sullivan D, Pearce EL. T cell metabolism drives immunity. J Exp Med. 2015;212(9):1345-60.

52. Ito K, Bonora M, Ito K. Metabolism as master of hematopoietic stem cell fate. Int J Hematol. 2019;109(1):18-27.

53. Wilkinson AC, Yamazaki S. The hematopoietic stem cell diet. Int J Hematol. 2018;107(6):634-41.

54. Ito K, Ito K. Hematopoietic stem cell fate through metabolic control. Exp Hematol. 2018;64:1-11.

55. Kopf H, de la Rosa GM, Howard OM, Chen X. Rapamycin inhibits differentiation of Th17 cells and promotes generation of FoxP3+ T regulatory cells. Int Immunopharmacol. 2007;7(13):1819-24.

56. Sun IH, Oh MH, Zhao L, Patel CH, Arwood ML, Xu W, et al. mTOR Complex 1 Signaling Regulates the Generation and Function of Central and Effector Foxp3(+) Regulatory T Cells. J Immunol. 2018;201(2):481-92.

57. Hartmann FJ, Mrdjen D, McCaffrey E, Glass DR, Greenwald NF, Bharadwaj A, et al. Single-cell metabolic profiling of human cytotoxic T cells. Nat Biotechnol. 2021;39(2):186-97.

58. Tan H, Yang K, Li Y, Shaw TI, Wang Y, Blanco DB, et al. Integrative Proteomics and Phosphoproteomics Profiling Reveals Dynamic Signaling Networks and Bioenergetics Pathways Underlying T Cell Activation. Immunity. 2017;46(3):488-503.

59. Ron-Harel N, Notarangelo G, Ghergurovich JM, Paulo JA, Sage PT, Santos D, et al. Defective respiration and one-carbon metabolism contribute to impaired naive T cell activation in aged mice. Proc Natl Acad Sci U S A. 2018;115(52):13347-52.

60. Ciofani M, Zuniga-Pflucker JC. Notch promotes survival of pre-T cells at the beta-selection checkpoint by regulating cellular metabolism. Nat Immunol. 2005;6(9):881-8.

61. Yang K, Blanco DB, Chen X, Dash P, Neale G, Rosencrance C, et al. Metabolic signaling directs the reciprocal lineage decisions of alphabeta and gammadelta T cells. Sci Immunol. 2018;3(25).

62. Zhang S, Zhang X, Wang K, Xu X, Li M, Zhang J, et al. Newly Generated CD4(+) T Cells Acquire Metabolic Quiescence after Thymic Egress. J Immunol. 2018;200(3):1064-77.

63. Mingueneau M, Kreslavsky T, Gray D, Heng T, Cruse R, Ericson J, et al. The transcriptional landscape of alphabeta T cell differentiation. Nat Immunol. 2013;14(6):619-32.

64. Macintyre AN, Gerriets VA, Nichols AG, Michalek RD, Rudolph MC, Deoliveira D, et al. The glucose transporter Glut1 is selectively essential for CD4 T cell activation and effector function. Cell Metab. 2014;20(1):61-72.

65. Ouyang X, Han Y, Qu G, Li M, Wu N, Liu H, et al. Metabolic regulation of T cell development by Sin1-mTORC2 is mediated by pyruvate kinase M2. J Mol Cell Biol. 2019;11(2):93-106.

66. Zhao FL, Ahn JJ, Chen ELY, Yi TJ, Stickle NH, Spaner D, et al. Peroxisome Proliferator-Activated Receptor-delta Supports the Metabolic Requirements of Cell Growth in TCRbeta-Selected Thymocytes and Peripheral CD4(+) T Cells. J Immunol. 2018;201(9):2664-82.

67. Ramstead AG, Wallace JA, Lee SH, Bauer KM, Tang WW, Ekiz HA, et al. Mitochondrial Pyruvate Carrier 1 Promotes Peripheral T Cell Homeostasis through Metabolic Regulation of Thymic Development. Cell Rep. 2020;30(9):2889-99 e6.

68. Corrado M, Samardzic D, Giacomello M, Rana N, Pearce EL, Scorrano L. Deletion of the mitochondria-shaping protein Opa1 during early thymocyte maturation impacts mature memory T cell metabolism. Cell Death Differ. 2021.

69. Anderson SJ, Lauritsen JP, Hartman MG, Foushee AM, Lefebvre JM, Shinton SA, et al. Ablation of ribosomal protein L22 selectively impairs alphabeta T cell development by activation of a p53-dependent checkpoint. Immunity. 2007;26(6):759-72.

70. Chapman NM, Boothby MR, Chi H. Metabolic coordination of T cell quiescence and activation. Nat Rev Immunol. 2020;20(1):55-70.

71. Cunningham CA, Hoppins S, Fink PJ. Cutting Edge: Glycolytic Metabolism and Mitochondrial Metabolism Are Uncoupled in Antigen-Activated CD8(+) Recent Thymic Emigrants. J Immunol. 2018;201(6):1627-32.

72. Koch U, Fiorini E, Benedito R, Besseyrias V, Schuster-Gossler K, Pierres M, et al. Delta-like 4 is the essential, nonredundant ligand for Notch1 during thymic T cell lineage commitment. J Exp Med. 2008;205(11):2515-23.

73. Taghon T, Yui MA, Pant R, Diamond RA, Rothenberg EV. Developmental and molecular characterization of emerging beta- and gammadelta-selected pre-T cells in the adult mouse thymus. Immunity. 2006;24(1):53-64.

74. Fan Y, Tajima A, Goh SK, Geng X, Gualtierotti G, Grupillo M, et al. Bioengineering Thymus Organoids to Restore Thymic Function and Induce Donor-Specific Immune Tolerance to Allografts. Mol Ther. 2015;23(7):1262-77.

75. Hare KJ, Jenkinson EJ, Anderson G. In vitro models of T cell development. Semin Immunol. 1999;11(1):3-12.

76. Itoh K, Tezuka H, Sakoda H, Konno M, Nagata K, Uchiyama T, et al. Reproducible establishment of hemopoietic supportive stromal cell lines from murine bone marrow. Exp Hematol. 1989;17(2):145-53.

77. Dobin A, Davis CA, Schlesinger F, Drenkow J, Zaleski C, Jha S, et al. STAR: ultrafast universal RNA-seq aligner. Bioinformatics. 2013;29(1):15-21.

78. Love MI, Huber W, Anders S. Moderated estimation of fold change and dispersion for RNA-seq data with DESeq2. Genome Biol. 2014;15(12):550.

79. Si Y, Liu P, Li P, Brutnell TP. Model-based clustering for RNA-seq data. Bioinformatics. 2014;30(2):197-205.

80. Zhou Y, Zhou B, Pache L, Chang M, Khodabakhshi AH, Tanaseichuk O, et al. Metascape provides a biologist-oriented resource for the analysis of systems-level datasets. Nat Commun. 2019;10(1):1523.

81. Subramanian A, Tamayo P, Mootha VK, Mukherjee S, Ebert BL, Gillette MA, et al. Gene set enrichment analysis: a knowledge-based approach for interpreting genome-wide expression profiles. Proc Natl Acad Sci U S A. 2005;102(43):15545-50.

82. Teague TK, Tan C, Marino JH, Davis BK, Taylor AA, Huey RW, et al. CD28 expression redefines thymocyte development during the pre-T to DP transition. Int Immunol. 2010;22(5):387-97.

83. Wilson A, Capone M, MacDonald HR. Unexpectedly late expression of intracellular CD3epsilon and TCR gammadelta proteins during adult thymus development. Int Immunol. 1999;11(10):1641-50.

84. Brandt D, Hedrich CM. TCRalphabeta(+)CD3(+)CD4(-)CD8(-) (double negative) T cells in autoimmunity. Autoimmun Rev. 2018;17(4):422-30.

85. Yamamoto R, Xu Y, Ikeda S, Sumida K, Tanaka H, Hozumi K, et al. Thymic Development of a Unique Bone Marrow-Resident Innate-like T Cell Subset with a Potent Innate Immune Function. J Immunol. 2019;203(1):167-77.

86. Bradley LM, Watson SR, Swain SL. Entry of naive CD4 T cells into peripheral lymph nodes requires L-selectin. J Exp Med. 1994;180(6):2401-6.

87. Budd RC, Cerottini JC, Horvath C, Bron C, Pedrazzini T, Howe RC, et al. Distinction of virgin and memory T lymphocytes. Stable acquisition of the Pgp-1 glycoprotein concomitant with antigenic stimulation. J Immunol. 1987;138(10):3120-9.

88. Ley K, Tedder TF. Leukocyte interactions with vascular endothelium. New insights into selectin-mediated attachment and rolling. J Immunol. 1995;155(2):525-8.

89. Fontenot JD, Rasmussen JP, Williams LM, Dooley JL, Farr AG, Rudensky AY. Regulatory T cell lineage specification by the forkhead transcription factor foxp3. Immunity. 2005;22(3):329-41.

90. Marshall D, Sinclair C, Tung S, Seddon B. Differential requirement for IL-2 and IL-15 during bifurcated development of thymic regulatory T cells. J Immunol. 2014;193(11):5525-33.

91. Tai X, Erman B, Alag A, Mu J, Kimura M, Katz G, et al. Foxp3 transcription factor is proapoptotic and lethal to developing regulatory T cells unless counterbalanced by cytokine survival signals. Immunity. 2013;38(6):1116-28.

92. Lio CW, Hsieh CS. A two-step process for thymic regulatory T cell development. Immunity. 2008;28(1):100-11.

93. Petkova SB, Yuan R, Tsaih SW, Schott W, Roopenian DC, Paigen B. Genetic influence on immune phenotype revealed strain-specific variations in peripheral blood lineages. Physiol Genomics. 2008;34(3):304-14.

94. Abe R, Kanagawa O, Sheard MA, Malissen B, Foo-Phillips M. Characterization of a new minor lymphocyte stimulatory system. I. Cluster of self antigens recognized by "I-E-reactive" V beta s, V beta 5, V beta 11, and V beta 12 T cell receptors for antigen. J Immunol. 1991;147(3):739-49.

95. Bill J, Kanagawa O, Woodland DL, Palmer E. The MHC molecule I-E is necessary but not sufficient for the clonal deletion of V beta 11-bearing T cells. J Exp Med. 1989;169(4):1405-19.

96. Bill J, Kanagawa O, Linten J, Utsunomiya Y, Palmer E. Class I and class II MHC gene products differentially affect the fate of V beta 5 bearing thymocytes. J Mol Cell Immunol. 1990;4(5):269-79; discussion 79-80.

97. Gao EK, Kanagawa O, Sprent J. Capacity of unprimed CD4+ and CD8+ T cells expressing V beta 11 receptors to respond to I-E alloantigens in vivo. J Exp Med. 1989;170(6):1947-57.

98. Hodes RJ, Abe R. Mouse endogenous superantigens: Ms and Mls-like determinants encoded by mouse retroviruses. Curr Protoc Immunol. 2001;Appendix 1:Appendix 1F.

99. Sugihara S, Maruo S, Tsujimura T, Tarutani O, Kohno Y, Hamaoka T, et al. Autoimmune thyroiditis induced in mice depleted of particular T cell subsets. III. Analysis of regulatory cells suppressing the induction of thyroiditis. Int Immunol. 1990;2(4):343-51.

100. Tomonari K, Fairchild S, Rosenwasser OA. Influence of viral superantigens on V beta- and V alpha-specific positive and negative selection. Immunol Rev. 1993;131:131-68.

101. Vacchio MS, Hodes RJ. Selective decreases in T cell receptor V beta expression. Decreased expression of specific V beta families is associated with expression of multiple MHC and non-MHC gene products. J Exp Med. 1989;170(4):1335-46.

102. Woodland D, Happ MP, Bill J, Palmer E. Requirement for cotolerogenic gene products in the clonal deletion of I-E reactive T cells. Science. 1990;247(4945):964-7.

103. Woodland DL, Happ MP, Gollob KJ, Palmer E. An endogenous retrovirus mediating deletion of alpha beta T cells? Nature. 1991;349(6309):529-30.

104. Mombaerts P, Iacomini J, Johnson RS, Herrup K, Tonegawa S, Papaioannou VE. RAG-1-deficient mice have no mature B and T lymphocytes. Cell. 1992;68(5):869-77.

105. Nowotschin S, Xenopoulos P, Schrode N, Hadjantonakis AK. A bright single-cell resolution live imaging reporter of Notch signaling in the mouse. BMC Dev Biol. 2013;13:15.

106. Berzins SP, Boyd RL, Miller JF. The role of the thymus and recent thymic migrants in the maintenance of the adult peripheral lymphocyte pool. J Exp Med. 1998;187(11):1839-48.

107. Boehm T. Self-renewal of thymocytes in the absence of competitive precursor replenishment. J Exp Med. 2012;209(8):1397-400.

108. Love PE, Bhandoola A. Signal integration and crosstalk during thymocyte migration and emigration. Nat Rev Immunol. 2011;11(7):469-77.

109. Rothenberg EV. Programming for T-lymphocyte fates: modularity and mechanisms. Genes Dev. 2019;33(17-18):1117-35.

110. de Barros SC, Vicente R, Chebli K, Jacquet C, Zimmermann VS, Taylor N. Intrathymic progenitor cell transplantation across histocompatibility barriers results in the persistence of early thymic progenitors and T-cell differentiation. Blood. 2013;121(11):2144-53.

111. Martins VC, Ruggiero E, Schlenner SM, Madan V, Schmidt M, Fink PJ, et al. Thymus-autonomous T cell development in the absence of progenitor import. J Exp Med. 2012;209(8):1409-17.

112. Peaudecerf L, Lemos S, Galgano A, Krenn G, Vasseur F, Di Santo JP, et al. Thymocytes may persist and differentiate without any input from bone marrow progenitors. J Exp Med. 2012;209(8):1401-8.

113. Ballesteros-Arias L, Silva JG, Paiva RA, Carbonetto B, Faisca P, Martins VC. T Cell Acute Lymphoblastic Leukemia as a Consequence of Thymus Autonomy. J Immunol. 2019;202(4):1137-44.

114. Martins VC, Busch K, Juraeva D, Blum C, Ludwig C, Rasche V, et al. Cell competition is a tumour suppressor mechanism in the thymus. Nature. 2014;509(7501):465-70.

115. Chung B, Montel-Hagen A, Ge S, Blumberg G, Kim K, Klein S, et al. Engineering the human thymic microenvironment to support thymopoiesis in vivo. Stem Cells. 2014;32(9):2386-96.

116. Poznansky MC, Evans RH, Foxall RB, Olszak IT, Piascik AH, Hartman KE, et al. Efficient generation of human T cells from a tissue-engineered thymic organoid. Nat Biotechnol. 2000;18(7):729-34.

117. Robinson JH, Owen JJ. Generation of T-cell function in organ culture of foetal mouse thymus. II. Mixed lymphocyte culture reactivity. Clin Exp Immunol. 1977;27(2):322-7.

118. Shyer JA, Flavell RA, Bailis W. Metabolic signaling in T cells. Cell Res. 2020;30(8):649-59.

119. Almeida L, Lochner M, Berod L, Sparwasser T. Metabolic pathways in T cell activation and lineage differentiation. Semin Immunol. 2016;28(5):514-24.

120. MacIver NJ, Michalek RD, Rathmell JC. Metabolic regulation of T lymphocytes. Annu Rev Immunol. 2013;31:259-83.

121. Geltink RIK, Kyle RL, Pearce EL. Unraveling the Complex Interplay Between T Cell Metabolism and Function. Annu Rev Immunol. 2018;36:461-88.

122. Hosokawa H, Rothenberg EV. How transcription factors drive choice of the T cell fate. Nat Rev Immunol. 2021;21(3):162-76.

123. Kumar BV, Connors TJ, Farber DL. Human T Cell Development, Localization, and Function throughout Life. Immunity. 2018;48(2):202-13.

124. Germain RN. T-cell development and the CD4-CD8 lineage decision. Nat Rev Immunol. 2002;2(5):309-22.

125. Montel-Hagen A, Sun V, Casero D, Tsai S, Zampieri A, Jackson N, et al. In Vitro Recapitulation of Murine Thymopoiesis from Single Hematopoietic Stem Cells. Cell Rep. 2020;33(4):108320.

126. Yu WM, Liu X, Shen J, Jovanovic O, Pohl EE, Gerson SL, et al. Metabolic regulation by the mitochondrial phosphatase PTPMT1 is required for hematopoietic stem cell differentiation. Cell Stem Cell. 2013;12(1):62-74.

127. He F, Ru X, Wen T. NRF2, a Transcription Factor for Stress Response and Beyond. Int J Mol Sci. 2020;21(13).

128. Fu Z, Ye J, Dean JW, Bostick JW, Weinberg SE, Xiong L, et al. Requirement of Mitochondrial Transcription Factor A in Tissue-Resident Regulatory T Cell Maintenance and Function. Cell Rep. 2019;28(1):159-71 e4.

129. Guidos CJ, Williams CJ, Wu GE, Paige CJ, Danska JS. Development of CD4+CD8+ thymocytes in RAG-deficient mice through a T cell receptor beta chain-independent pathway. J Exp Med. 1995;181(3):1187-95.

130. Hagenbeek TJ, Naspetti M, Malergue F, Garcon F, Nunes JA, Cleutjens KB, et al. The loss of PTEN allows TCR alphabeta lineage thymocytes to bypass IL-7 and Pre-TCR-mediated signaling. J Exp Med. 2004;200(7):883-94.

131. Bosticardo M, Pala F, Calzoni E, Delmonte OM, Dobbs K, Gardner CL, et al. Artificial thymic organoids represent a reliable tool to study T-cell differentiation in patients with severe T-cell lymphopenia. Blood Adv. 2020;4(12):2611-6.

132. Le J, Park JE, Ha VL, Luong A, Branciamore S, Rodin AS, et al. Single-Cell RNA-Seq Mapping of Human Thymopoiesis Reveals Lineage Specification Trajectories and a Commitment Spectrum in T Cell Development. Immunity. 2020;52(6):1105-18 e9.

133. Park JE, Botting RA, Dominguez Conde C, Popescu DM, Lavaert M, Kunz DJ, et al. A cell atlas of human thymic development defines T cell repertoire formation. Science. 2020;367(6480).

134. Swainson L, Kinet S, Manel N, Battini JL, Sitbon M, Taylor N. Glucose transporter 1 expression identifies a population of cycling CD4+ CD8+ human thymocytes with high CXCR4-induced chemotaxis. Proc Natl Acad Sci U S A. 2005;102(36):12867-72.

135. Jones N, Cronin JG, Dolton G, Panetti S, Schauenburg AJ, Galloway SAE, et al. Metabolic Adaptation of Human CD4(+) and CD8(+) T-Cells to T-Cell Receptor-Mediated Stimulation. Front Immunol. 2017;8:1516.

136. Hale LP, Braun RD, Gwinn WM, Greer PK, Dewhirst MW. Hypoxia in the thymus: role of oxygen tension in thymocyte survival. Am J Physiol Heart Circ Physiol. 2002;282(4):H1467-77.

137. Mak TW, Chaddah MR, Saunders ME. The immune response: basic and clinical principles. Amsterdam: Elsevier; 2006. p. 341-72.

138. Sudo T, Nishikawa S, Ohno N, Akiyama N, Tamakoshi M, Yoshida H, et al. Expression and function of the interleukin 7 receptor in murine lymphocytes. Proc Natl Acad Sci U S A. 1993;90(19):9125-9.

139. Guillemard E, Nugeyre MT, Chene L, Schmitt N, Jacquemot C, Barre-Sinoussi F, et al. Interleukin-7 and infection itself by human immunodeficiency virus 1 favor virus persistence in mature CD4(+)CD8(-)CD3(+) thymocytes through sustained induction of Bcl-2. Blood. 2001;98(7):2166-74.

140. Yu Q, Park JH, Doan LL, Erman B, Feigenbaum L, Singer A. Cytokine signal transduction is suppressed in preselection double-positive thymocytes and restored by positive selection. J Exp Med. 2006;203(1):165-75.

141. Rathmell JC, Vander Heiden MG, Harris MH, Frauwirth KA, Thompson CB. In the absence of extrinsic signals, nutrient utilization by lymphocytes is insufficient to maintain either cell size or viability. Mol Cell. 2000;6(3):683-92.

142. Vander Heiden MG, Plas DR, Rathmell JC, Fox CJ, Harris MH, Thompson CB. Growth factors can influence cell growth and survival through effects on glucose metabolism. Mol Cell Biol. 2001;21(17):5899-912.